Chapter 1

Introduction

Graphite, which is one of the most prevalent carbon allotropes, is a layered material in which infinite sheets of hexagonal carbon networks are stacked in the AB fashion (Bernal stacking) with the aid of weak intersheet interaction [1], as shown in Fig. 1.1. Each two-dimensional (2D) sheet is called graphene. The unit cell of graphene, with a lattice constant of $a = 0.246$ nm, is formed of two independent carbon sites, where the strong σ-bonds and weak π-bonds of the carbon atoms give a bond length of 0.142 nm. The σ-bonds consist of threefold symmetric sp^3 hybrid orbitals of $2s$, $2p_x$, and $2p_y$ orbitals, while the π-bonds consist of $2p_z$ orbitals. Graphite has two independent graphene sheets, where some carbon atoms in a graphene sheet are on top of carbon atoms in the sheet underneath and others are over the centers of hexagons in the sheet underneath.

The quasi-2D structural feature of graphite makes its electronic band structure quasi-2D [2]. Figure 1.2(a) shows the energy band structure of graphite for the lattice structure shown in Fig. 1.1(b), which is obtained on the basis of the density functional theory with the local density approximation. The quasi-2D character can be seen in the less dispersive energy band feature for both the σ- and π-bands in the intersheet directions K↔H and Γ↔A in the Brillouin zone, even though the bands have strong wave number
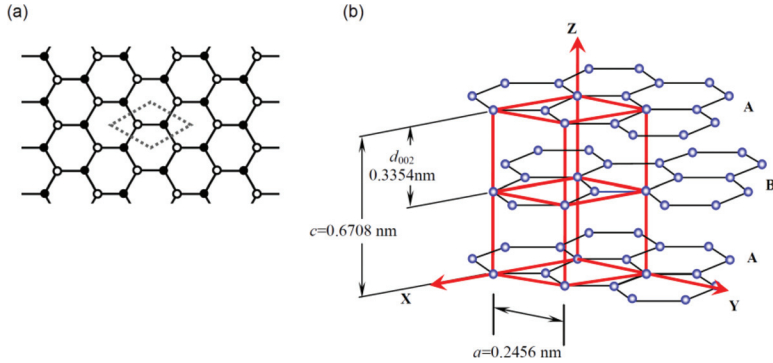
Figure 1.1 The structures of (a) graphene and (b) graphite. The unit cell (dotted lines) of graphene with a lattice constant of $a = 0.2456$ nm has two independent carbon atoms (filled and open circles). Graphene sheets in graphite are stacked in AB fashion. The unit cell of graphite (bold red lines) has four independent carbon atoms. The intra-sheet and c-axis lattice constants are 0.2456 nm and 0.6708 nm, respectively.

dependence in the intrasheet directions. The valence π-band and the conduction π*-band are each split into two subbands due to the presence of two independent graphene sheets interacting with each other in a unit cell. What is important is that these bands touch each other at the K point, giving a semimetallic electronic structure. Indeed, the weakly dispersive π-band crosses the Fermi level along the direction K↔H, resulting in the coexistence of the same small number of electrons and holes. A single graphene sheet extracted from graphite is free from the intersheet interaction and thus a pure 2D electronic structure is formed as shown in Fig. 1.2(b). The feature of the electronic structure of graphite is roughly preserved in graphene.

What distinguishes graphene from graphite is the zero-gap semiconducting feature that appears at the K point, where the valence π-band and conduction π*-band having a linear wave number dependence touch each other. Interestingly, the linear dispersion of the π- and π*-bands in the vicinity of the Fermi level indicates the feature of massless electrons at the Fermi level. This unconventional electronic structure of graphene, first predicted theoretically by Wallace in 1947 [3], is effectively equivalent to
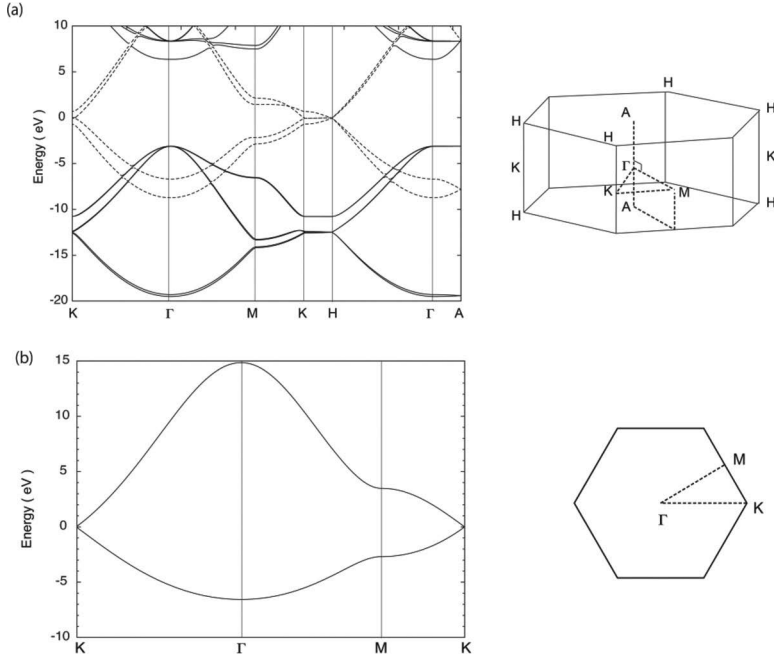
(a)

(b)

Figure 1.2 (a) The band structure of graphite with its Brillouin zone. The band structure of graphite is calculated by a mixed-basis pseudopotential method. The solid and dotted lines denote the σ- and π-bands, respectively. (b) π-bands of graphene are derived from the tight binding method.

what we observe for the massless fermion in the relativistic Dirac equation (Weyl equation for neutrinos) [4]. Moreover, in graphene we can expect phenomena the same as those observed for neutrinos. After the successful isolation of graphene in 2004 [5], theoretical and experimental efforts have unveiled a variety of phenomena related to the intriguing features of the massless Dirac fermion in graphene [6], including the half-integer quantum Hall effect [7, 8]. The massless electrons in graphene, whose Fermi velocity is about 1/300 the speed of light, has attracted great attention in cutting-edge nanotechnology applications [9, 10].

When we discuss graphene, we involve another aspect from chemistry. The fundamental unit of graphene is the hexagonal benzene ring that we discuss in chemistry. Indeed, graphene is formed
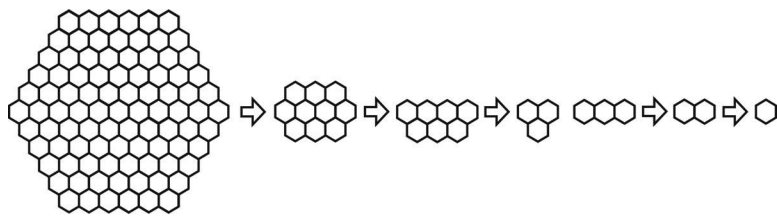
Figure 1.3 Fragmentation of graphene into small polycyclic aromatic hydrocarbon molecules.

by fusing an infinite number of benzene rings two-dimensionally. Accordingly, we expect that the knowledge we use in chemistry is applicable in understanding the properties of graphene. With this viewpoint, we can create a variety of graphene fragments whose sizes extend from small polycyclic aromatic hydrocarbon molecules to macro-size graphene, as shown in Fig. 1.3. Among these, the nano-size graphene (nanographene) is particularly important as this forms a bridge between small polycyclic aromatic hydrocarbon molecules and infinite graphene, which are related to issues of chemistry and physics, respectively. The electronic structures of small polycyclic aromatic hydrocarbon molecules depend on the shapes of the molecules: in other words, on how benzene rings are fused. For example, there are two ways to fuse three benzene rings: fusing them in 1D gives anthracene, while fusing them into a triangle gives phenalene. The former is well stabilized and chemically inactive as a Kekulé molecule having a closed-shell electronic structure, whereas the latter is unstable and very chemically active as a non-Kekulé molecule having an open-shell electronic structure with a spin state of $S = 1/2$. This geometrical dependence is also preserved in the edges of nanographene and graphene, as we can understand on the basis of Clar's aromatic sextet rule [11]. Actually, there are two types of edges: zigzag edges and armchair edges, which give essentially different electronic features owing to Kekulé and non-Kekulé structures, respectively. Importantly, nonbonding π-electron states having a large local density of states with localized spins are created in zigzag edges, and these are the origin of the electronic, magnetic, and chemical activities of nanographene and
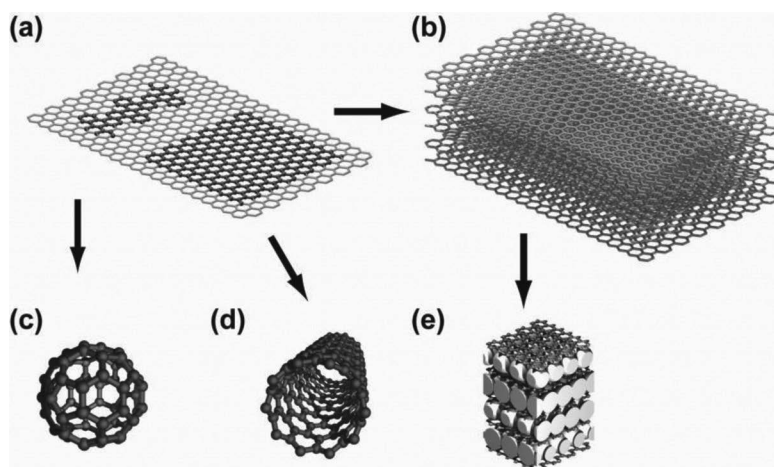
Figure 1.4 Carbon-based π-electron materials: (a) graphene, (b) graphite, (c) fullerene (C_{60}), (d) a carbon nanotube, and (e) a graphite intercalation compound (KC_8). The parts drawn with bold lines in (a) are the precursors of the C_{60} and the carbon nanotube. The large white spheres in (e) are potassium atoms.

graphene edges [12]. This is important for applications such as spintronics devices, batteries, catalysts, and fuel cells.

There exist important carbon-based π-electron materials, which have been at the focal point in physics and chemistry these past three decades, that is, graphite intercalation compounds, fullerenes, and carbon nanotubes, as illustrated in Fig. 1.4. Graphite intercalation compounds (GICs) are obtained when a variety of guest molecules (intercalates) having abilities to donate and accept electrons are accepted into the graphitic galleries through charge transfer interaction with graphene having amphoteric electronic properties. GICs are 2D metallic systems showing exotic electronic features such as high electrical conductivity, superconductivity, and 2D magnetism [13, 14]. Folding a graphene sheet into a spherical shape yields a fullerene [15], while rolling one into a cylindrical shape yields a carbon nanotube [16]. These are carbon nanomaterials having electronic properties that are interesting not only in fundamental science but also for device applications. Here, graphene is the most basic material, from which are created all the π-electron-based

carbon systems such as graphite, fullerenes, carbon nanotubes, and graphite intercalation compounds. Therefore, knowledge about graphene is particularly important in understanding these carbon-based materials.

In the following chapters, we discuss the properties of graphene from the viewpoints of physics and chemistry as follows: Chapter 2, "Theory of Electronic States and Transport in Graphene"; Chapter 3, "Experimental Approach to Graphene and Device Applications"; Chapter 4, "Theory of Electronic Properties of Nanographene"; Chapter 5, "Spin Structure of Polycyclic Aromatic Hydrocarbons (PAHs)"; and Chapter 6, "Experimental Approach to Electronic and Magnetic Properties of Nanographene."

References

1. Kelly, B. T. (1981). *Physics of graphite* (Applied Science Publishers, London).
2. Horzwarth, N. A. W., Louie, S. G. and Rabii, S. (1982). X-ray form factors and the electronic structure of graphite, *Phys. Rev. B*, **26**, pp. 5382–5390.
3. Wallace, P. R. (1947). The band theory of graphite, *Phys. Rev.*, **71**, pp. 476 and pp. 622–634.
4. Shon, N. H. and Ando, T. (1998). Quantum transport in two-dimensional graphite system, *J. Phys. Soc. Jpn.*, **67**, pp. 2421–2429.
5. Novoselov, K. S., Geim, A. K., Morozov, S. V., Jiang, D., Zhang, Y., Dubonos, S. V., Grigorieva, I. V. and Firsov, A. A. (2004). Electric field effect in atomically thin carbon films, *Science*, **306**, pp. 666–669.
6. Castro Neto, A. H., Guinea, F., Peres, N. M. R., Novoselov, K. S. and Geim, A. K. (2009). The electronic properties of graphene, *Rev. Mod. Phys.*, **81**, pp. 109–162.
7. Novoselov, K. S., Geim, A. K., Morozov, S. V., Jiang, D., Katsnelson, M. I., Grigorieva, I. V., Dubonos, S. V. and Firsov, A. A. (2005). Two-dimensional gas of massless Dirac fermion in graphene, *Nature*, **438**, pp. 197–200.
8. Zhang, Y., Tan, Y-W., Stormer, H. L. and Kim, P. (2005). Experimental observation of the quantum Hall effect and Berry's phase in graphene, *Nature*, **438**, pp. 201–204.
9. Berger, C., Song, Z., Li, T., Li, X., Ogbazghi, A. Y., Feng, R., Dai, Z., Marchenkov, A. N., Conrad, E. H., First, P. N. and de Heer, W. A. (2004).

Ultrathin epitaxial graphite: 2D electron gas properties and a route toward graphene-based nanoelectronics, *J. Chem. Phys. B*, **108**, pp. 19912–19916.

10. Cheianov, V. V., Fal'ko, V. and Altshuler, B. L. (2007). The focusing of electron flow and a Veselago lens in graphene p–n junctions, *Science,* **315**, pp. 1252–1255.

11. Clar, E. (1972). *The Aromatic Sextet* (Wiley, London).

12. Fujita, M., Wakabayashi, K., Nakada, K. and Kusakabe, K. (1996). Peculiar localized state at zigzag graphite edge, *J. Phys. Soc. Jpn.,* **65**, pp. 1920–1923.

13. Dresselhaus, M. S. and Dresselhaus, G. (1981). Intercalation compounds of graphite, *Adv. Phys.*, **30**, pp. 139–326.

14. Enoki, T., Suzuki, M. and Endo, M. (2003). *Graphite Intercalation Compounds and Applications* (Oxford University Press, New York).

15. Dresselhaus, M. S., Dresselhaus, G. and Eklund, P. C. (1996). *Science of Fullerenes and Carbon Nanotubes* (Academic Press, San Diego).

16. Saito, R., Dresselhaus, G., and Dresselhaus, M. S. (1998). *Physical Properties of Carbon Nanotubes* (Imperial College Press, London).

This page intentionally left blank

Chapter 2

Theory of Electronic States and Transport in Graphene

Tsuneya Ando

Department of Physics, Tokyo Institute of Technology
2-12-1 Ookayama, Meguro-ku, Tokyo 152-8551, Japan
ando@phys.titech.ac.jp

2.1 Introduction

Graphene is a monolayer graphite sheet recently fabricated [1–3] and has been attracting attention theoretically and experimentally since the observation of the integer quantum Hall effect [4, 5]. Several reviews have already been published [6–9]. Actually, graphene has been a subject of study prior to the experimental realization because of the peculiar electronic structure responsible for intriguing properties of carbon nanotubes [10] and because of theoretical interest in special properties of systems in relativistic limit. The purpose of this chapter is to give a brief review on electronic properties of graphenes mainly from a theoretical point of view. The topics include effective-mass description of electronic states, transport and optical properties, and phonons and their interaction with electrons.

Within an effective-mass approximation or a **k·p** scheme, the electron motion in graphene is governed by the Weyl equation for a neutrino or the Dirac equation with vanishing rest mass or in the relativistic limit [6–16]. An important feature is the presence of a topological singularity at $\mathbf{k} = 0$. This singularity is the origin of the absence of backscattering in metallic carbon nanotubes [17, 18]. It also leads to the presence of a Landau level at $\varepsilon = 0$, responsible for the singular diamagnetic susceptibility [19–22]. It is considered the origin of the peculiar behavior in transport, such as the minimum conductivity [23], the half-integer quantum Hall effect [24], the dynamical conductivity [25], and the special time reversal symmetry [26–28] leading to antilocalization behavior [29, 30]. A massless Dirac system can also be realized in organic conductors [31]. Bilayer graphene has a zero-gap structure, but with quadratic dispersion unlike monolayer, leading to nonzero density of states even at zero energy [32–39]. Electronic states in multilayer graphene are well understood in terms of decomposition of the Hamiltonian into those of monolayer or bilayers [40–42].

In Sections 2.2–2.5, various properties of monolayer graphene are described: In Section 2.2, effective-mass description of electronic states is briefly reviewed, in Section 2.3 the singular behavior of the orbital diamagnetic response is discussed, in Section 2.4 the dynamical conductivity describing optical absorption is discussed, in Section 2.5 the singular behavior of the conductivity is discussed together with the Hall coefficient and the nonuniversal behavior of the minimum conductivity at the Dirac point, and in Section 2.6 phonons and effects of electron–phonon interactions are reviewed. In Section 2.7, similar discussions are given for bilayer graphene. In Section 2.8, the effective Hamiltonian in multilayer graphenes are shown to be decomposed into those of bilayer graphenes and that of a monolayer graphene when several important parameters characterizing interlayer interactions are considered.

2.2 Electronic States of Monolayer Graphene

2.2.1 *Massless Dirac Electron*

The lattice structure of monolayer graphene and the first Brillouin zone are shown in Figs. 2.1(a) and (b), respectively. We have the
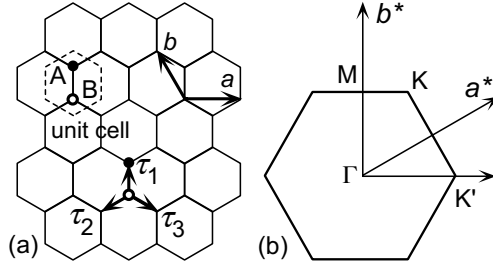
Figure 2.1 (a) The lattice structure of graphene sheet. Two primitive translation vectors are denoted by **a** and **b**. A unit cell represented by a dashed line contains two carbon atoms denoted by A and B. Three vectors directed from a B site to nearest neighbor A sites are given by $\vec{\tau}_l$ ($l = 1, 2, 3$). (b) The first Brillouin zone. The vertices of the hexagon are called K and K′ points and reciprocal lattice vectors are denoted by **a*** and **b***.

primitive translation vectors $\mathbf{a} = a(1, 0)$ and $\mathbf{b} = a(-1/2, \sqrt{3}/2)$, and the vectors connecting nearest neighbor carbon atoms $\vec{\tau}_1 = a(0, 1/\sqrt{3})$, $\vec{\tau}_2 = a(-1/2, -1/2\sqrt{3})$, and $\vec{\tau}_3 = a(1/2, -1/2\sqrt{3})$, where a is the lattice constant given by $a = 0.246$ nm. A unit cell with area $\Omega_0 = (\sqrt{3}/2)a^2$ contains two carbon atoms, which will be denoted by A and B in the following as shown in Fig. 2.1(a). The primitive reciprocal lattice vectors $\mathbf{a}^*$ and $\mathbf{b}^*$ are given by $\mathbf{a}^* = (2\pi/a)(1, 1/\sqrt{3})$ and $\mathbf{b}^* = (2\pi/a)(0, 2/\sqrt{3})$, The hexagonal first Brillouin zone has area $\Omega_0^* = (2/\sqrt{3})(2\pi/a)^2$.

The K and K′ points at the corners of the Brillouin zone are given as $\mathbf{K} = (2\pi/a)(1/3, 1/\sqrt{3})$ and $\mathbf{K}' = (2\pi/a)(2/3, 0)$, respectively. We have the relations $\exp(i\mathbf{K} \cdot \vec{\tau}_1) = \omega$, $\exp(i\mathbf{K} \cdot \vec{\tau}_2) = \omega^{-1}$, $\exp(i\mathbf{K} \cdot \vec{\tau}_3) = 1$, $\exp(i\mathbf{K}' \cdot \vec{\tau}_1) = 1$, $\exp(i\mathbf{K}' \cdot \vec{\tau}_2) = \omega^{-1}$, and $\exp(i\mathbf{K}' \cdot \vec{\tau}_3) = \omega$, with $\omega = \exp(2\pi i/3)$. As will be shown below, the conduction and valence bands consisting of π states touch at the K and K′ points, where the Fermi level is located, and therefore electronic properties are determined by the states near the K and K′ points.

In a tight-binding model, the wave function is written as

$$\psi(\mathbf{r}) = \sum_{\mathbf{R}_A} \psi_A(\mathbf{R}_A)\phi(\mathbf{r} - \mathbf{R}_A) + \sum_{\mathbf{R}_B} \psi_B(\mathbf{R}_B)\phi(\mathbf{r} - \mathbf{R}_B), \qquad (2.1)$$

where $\phi(\mathbf{r})$ is the wave function of the p_z orbital of a carbon atom located at the origin, $\mathbf{R}_A = n_a\mathbf{a} + n_b\mathbf{b} + \vec{\tau}_1$, and $\mathbf{R}_B = n_a\mathbf{a} + n_b\mathbf{b}$ with integer n_a and n_b. Let $-\gamma_0$ be the transfer integral between nearest-neighbor carbon atoms and choose the energy origin at that of the

carbon p_z level. Then, we have

$$\varepsilon \psi_A(\mathbf{R}_A) = -\gamma_0 \sum_{l=1}^{3} \psi_B(\mathbf{R}_A - \vec{\tau}_l),$$

$$\varepsilon \psi_B(\mathbf{R}_B) = -\gamma_0 \sum_{l=1}^{3} \psi_A(\mathbf{R}_B + \vec{\tau}_l), \qquad (2.2)$$

where the overlap integral between nearest A and B sites is completely neglected for simplicity.

Assuming $\psi_A(\mathbf{R}_A) \propto f_A(\mathbf{k})\exp(i\mathbf{k}\cdot\mathbf{R}_A)$ and $\psi_B(\mathbf{R}_B) \propto f_B(\mathbf{k})\exp(i\mathbf{k}\cdot\mathbf{R}_B)$, we have

$$\begin{pmatrix} 0 & h_{AB}(\mathbf{k}) \\ h_{AB}(\mathbf{k})^* & 0 \end{pmatrix} \begin{pmatrix} f_A(\mathbf{k}) \\ f_B(\mathbf{k}) \end{pmatrix} = \varepsilon \begin{pmatrix} f_A(\mathbf{k}) \\ f_B(\mathbf{k}) \end{pmatrix}, \qquad (2.3)$$

$$h_{AB}(\mathbf{k}) = -\gamma_0 \sum_l \exp(-i\mathbf{k}\cdot\vec{\tau}_l). \qquad (2.4)$$

The energy bands are given by

$$\varepsilon_{\pm}(\mathbf{k}) = \pm\gamma_0 \sqrt{1 + 4\cos\frac{ak_x}{2}\cos\frac{\sqrt{3}ak_y}{2} + 4\cos^2\frac{ak_x}{2}}. \qquad (2.5)$$

They are shown in Fig. 2.2.

In order to see the behavior in the vicinity of a K point, we replace $\mathbf{k}$ with $\mathbf{K} + \mathbf{k}$. Then, to the lowest order in $|\mathbf{k}|a$, we have

$$-\gamma_0 \sum_{l=1}^{3} \exp[-i(\mathbf{K}+\mathbf{k})\cdot\vec{\tau}_l] = -i\omega^{-1}\gamma(k_x - ik_y). \qquad (2.6)$$

with

$$\gamma = \frac{\sqrt{3}a\gamma_0}{2}, \qquad (2.7)$$

A similar expansion is possible for the K′ point. Therefore, we have $\varepsilon_{\pm}(\mathbf{K}) = \varepsilon_{\pm}(\mathbf{K}') = 0$, showing that there is no gap at the K and K′ points. For $f_A(\mathbf{K}+\mathbf{k}) = \tilde{f}_A(\mathbf{k})$ and $f_B(\mathbf{K}+\mathbf{k}) = i\omega\tilde{f}_B(\mathbf{k})$, we have

$$\gamma \begin{pmatrix} 0 & k_x - ik_y \\ k_x + ik_y & 0 \end{pmatrix} \begin{pmatrix} \tilde{f}_A(\mathbf{k}) \\ \tilde{f}_B(\mathbf{k}) \end{pmatrix} = \varepsilon \begin{pmatrix} \tilde{f}_A(\mathbf{k}) \\ \tilde{f}_B(\mathbf{k}) \end{pmatrix}. \qquad (2.8)$$

In terms of the Pauli spin matrices

$$\sigma_x = \begin{pmatrix} 0 & 1 \\ 1 & 0 \end{pmatrix}, \quad \sigma_y = \begin{pmatrix} 0 & -i \\ i & 0 \end{pmatrix}, \quad \sigma_z = \begin{pmatrix} 1 & 0 \\ 0 & -1 \end{pmatrix}, \qquad (2.9)$$
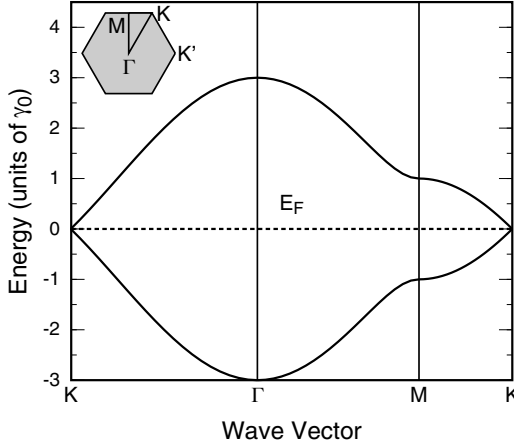
Figure 2.2 The π band structure of graphene obtained in a nearest-neighbor tight-binding model along $K \to \Gamma \to M \to K$ shown in the inset. The Fermi level lies at the center $\varepsilon = 0$.

the above is rewritten as

$$\gamma(\vec{\sigma} \cdot \mathbf{k})\tilde{\mathbf{f}}(\mathbf{k}) = \varepsilon\tilde{\mathbf{f}}(\mathbf{k}), \quad \tilde{\mathbf{f}}(\mathbf{k}) = \begin{pmatrix} \tilde{f}_A(\mathbf{k}) \\ \tilde{f}_B(\mathbf{k}), \end{pmatrix} \tag{2.10}$$

with $\vec{\sigma} = (\sigma_x, \sigma_y)$. For the K' point, we have the same equation except that $\vec{\sigma}$ is replaced with $\vec{\sigma}^*$.

In the vicinity of the K and K' points, the energy becomes

$$\varepsilon_s(\mathbf{k}) = s\gamma|\mathbf{k}|, \quad (s = \pm 1), \tag{2.11}$$

giving the density of states

$$D(\varepsilon) = \frac{g_s g_v}{L^2} \sum_{s,\mathbf{k}} \delta(\varepsilon - s\gamma|\mathbf{k}|) = \frac{g_s g_v |\varepsilon|}{2\pi\gamma^2}, \tag{2.12}$$

with system area L^2, spin degeneracy $g_s = 2$, and valley degeneracy $g_v = 2$. The corresponding electron or hole concentration at zero temperature is given by

$$n_s = \text{sgn}(\varepsilon)\frac{g_s g_v \varepsilon^2}{4\pi\gamma^2}, \tag{2.13}$$

with

$$\text{sgn}(t) = \begin{cases} +1 & (t > 0); \\ 0 & (t = 0); \\ -1 & (t < 0). \end{cases} \tag{2.14}$$
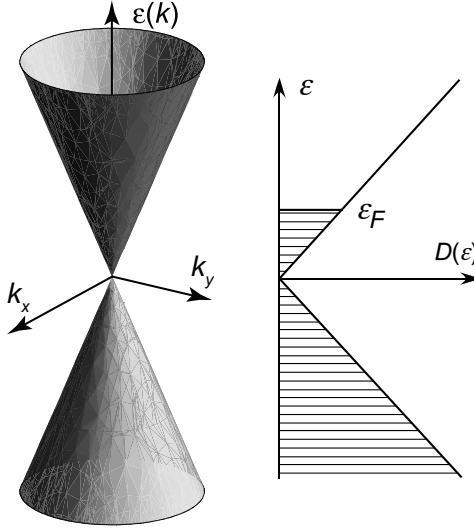
Figure 2.3 The energy bands in the vicinity of the K and K' points and the density of states in monolayer graphene.

This energy dispersion and the density of states are shown in Fig. 2.3. Because the density of states vanishes at $\varepsilon = 0$, to be called the Dirac point, graphene is often called a zero-gap semiconductor. This is quite inappropriate as will be shown later because of its metallic behavior.

In an effective-mass approximation or a **k·p** scheme near the K and K' points, the effective Schrödinger equation is obtained from Eq. (2.10) by replacing **k** with operator $\hat{\mathbf{k}} = -i\vec{\nabla}$. Then, we have

$$\gamma \begin{pmatrix} 0 & \hat{k}_x - i\hat{k}_y \\ \hat{k}_x + i\hat{k}_y & 0 \end{pmatrix} \mathbf{F}^K(\mathbf{r}) = \varepsilon \mathbf{F}^K(\mathbf{r}),$$

$$\gamma \begin{pmatrix} 0 & \hat{k}_x + i\hat{k}_y \\ \hat{k}_x - i\hat{k}_y & 0 \end{pmatrix} \mathbf{F}^{K'}(\mathbf{r}) = \varepsilon \mathbf{F}^{K'}(\mathbf{r}),$$

$$(2.15)$$

where $\mathbf{F}^K(\mathbf{r})$ and $\mathbf{F}^{K'}(\mathbf{r})$ are two-component wave functions

$$\mathbf{F}^K(\mathbf{r}) = \begin{pmatrix} F_A^K(\mathbf{r}) \\ F_B^K(\mathbf{r}) \end{pmatrix}, \quad \mathbf{F}^{K'}(\mathbf{r}) = \begin{pmatrix} F_A^{K'}(\mathbf{r}) \\ F_B^{K'}(\mathbf{r}) \end{pmatrix}. \tag{2.16}$$

These are rewritten as

$$\gamma(\vec{\sigma} \cdot \hat{\mathbf{k}})\mathbf{F}^K(\mathbf{r}) = \varepsilon \mathbf{F}^K(\mathbf{r}),$$

$$\gamma(\vec{\sigma}^* \cdot \hat{\mathbf{k}})\mathbf{F}^{K'}(\mathbf{r}) = \varepsilon \mathbf{F}^{K'}(\mathbf{r}). \tag{2.17}$$

This is equivalent to the Weyl equation for a neutrino or relativistic Dirac electron with vanishing rest mass, moving with the velocity of light, except that the velocity

$$v = \frac{\gamma}{\hbar} \qquad (2.18)$$

is about 1/300 of the light velocity. This neutrino description of the electron motion is most suitable for revealing various interesting features of electronic properties of graphene.

In magnetic field B perpendicular to graphene layer, we should make replacement $\hat{\mathbf{k}} = -i\vec{\nabla} + (e/c\hbar)\mathbf{A}$ with vector potential $\mathbf{A}$, giving $B = \vec{\nabla} \times \mathbf{A} = (\partial A_y/\partial x) - (\partial A_x/\partial y)$. In the presence of external potential $V(\mathbf{r})$, which is slowly varying in a scale of the lattice constant and therefore is the same between A and B sites within a unit cell, $V(\mathbf{r})$ should be added to the diagonal element of Eqs. (2.15) and (2.17). The Schrödinger equation in the presence of potential with range shorter than the lattice constant causing mixing between the K and K' points can also be derived. Readers interested in more details on the effective-mass approximation should refer to Ref. [10], for example.

2.2.2 *Berry's Phase and Topological Anomaly*

The eigen wave functions and energies of the Hamiltonian for the K point are written in the absence of a magnetic field as

$$\mathbf{F}_{s\mathbf{k}}(\mathbf{r}) = \frac{1}{L} \exp(i\mathbf{k} \cdot \mathbf{r}) \, \mathbf{F}_{s\mathbf{k}}. \qquad (2.19)$$

In general, we can write eigenvector $\mathbf{F}_{s\mathbf{k}}$ as

$$\mathbf{F}_{s\mathbf{k}} = \exp[i\phi_s(\mathbf{k})] \, R^{-1}[\theta(\mathbf{k})] \, |s\rangle, \qquad (2.20)$$

where $\phi_s(\mathbf{k})$ is an arbitrary phase factor, $\theta(\mathbf{k})$ is the angle between wave vector $\mathbf{k}$ and the k_y axis, i.e., $k_x + ik_y = +i|\mathbf{k}|e^{i\theta(\mathbf{k})}$ and $k_x - ik_y = -i|\mathbf{k}|e^{-i\theta(\mathbf{k})}$, $R(\theta)$ is a spin-rotation operator, given by

$$R(\theta) = \exp\left(i\frac{\theta}{2}\sigma_z\right) = \begin{pmatrix} \exp(+i\theta/2) & 0 \\ 0 & \exp(-i\theta/2) \end{pmatrix}, \qquad (2.21)$$

with σ_z being a Pauli matrix, and $|s\rangle$ is the eigenvector for the state with $\mathbf{k}$ in the positive k_y direction, given by

$$|s\rangle = \frac{1}{\sqrt{2}} \begin{pmatrix} -is \\ 1 \end{pmatrix}. \qquad (2.22)$$

Obviously, we have

$$
\begin{aligned}
R(\theta_1)R(\theta_2) &= R(\theta_1 + \theta_2), \\
R(-\theta) &= R^{-1}(\theta).
\end{aligned}
\tag{2.23}
$$

Further, because $R(\theta)$ describes the rotation of a spin, it has the property

$$
R(\theta \pm 2\pi) = -R(\theta),
\tag{2.24}
$$

which gives $R(-\pi) = -R(+\pi)$. The appearance of the spin rotation operator and the corresponding sign change under the 2π rotation around $\mathbf{k} = 0$ correspond to a topological singularity at $\mathbf{k} = 0$. Because phase $\phi_s(\mathbf{k})$ is arbitrary, we can choose the eigen wave function as

$$
\mathbf{F}_{s\mathbf{k}} = \frac{1}{\sqrt{2}} \begin{pmatrix} -is \, \exp[-i\theta(\mathbf{k})] \\ 1 \end{pmatrix}.
\tag{2.25}
$$

This is the "spin" part of an eigenfunction, obtained by choosing $\phi_s(\mathbf{k}) = -\theta(\mathbf{k})/2$ in such a way that the wave function becomes continuous as a function of $\theta(\mathbf{k})$. It seems that this $\mathbf{F}_{s\mathbf{k}}$ does not change the sign after 2π rotation $\theta(\mathbf{k}) \rightarrow \theta(\mathbf{k}) + 2\pi$. However, the wave function changes the sign when we consider Berry's phase [43, 44].

Let us consider the case that the Hamiltonian contains parameter η and change η from $\eta(0)$ to $\eta(T)$ as a function of time t from $t = 0$ to $t = T$ and assume that $\mathcal{H}[\eta(T)] = \mathcal{H}[\eta(0)]$. Note that $\eta(T)$ is not necessarily the same as $\eta(0)$. When there is no degeneracy, the state at $t = T$ is completely same as that at $t = 0$ when the process is sufficiently slow and adiabatic. Let us write

$$
\psi(T) = \psi(0) \exp\left(-i\varphi - \frac{i}{\hbar} \int_0^T dt' \, E_0[\eta(t')] \right),
\tag{2.26}
$$

where $E_0[\eta(t)]$ is eigen energy in the steady state, i.e.,

$$
\mathcal{H}[\eta(t)]\psi_0[\eta(t)] = E_0[\eta(t)]\psi_0[\eta(t)],
\tag{2.27}
$$

and therefore represents phase change corresponding to electron energy. Extra phase φ is called the Berry phase.

In order to obtain an explicit expression of φ, we write

$$
\psi(t) = \psi[\eta(t)] \exp\left(-i\varphi(t) - \frac{i}{\hbar} \int_0^t dt' \, E_0[\eta(t')] \right),
\tag{2.28}
$$

and substitute $\psi(t)$ into the time-dependent Schrödinger equation. Then, we have

$$\frac{d\varphi(t)}{dt} = -i \left\langle \psi[\eta(t)] \middle| \frac{d\psi[\eta(t)]}{dt} \right\rangle, \tag{2.29}$$

and on integration we have

$$\varphi = -i \int_0^T dt \left\langle \psi[\eta(t)] \middle| \frac{d\psi[\eta(t)]}{dt} \right\rangle. \tag{2.30}$$

When the wave vector **k** is rotated in the anticlockwise direction adiabatically as a function of time t around the origin for a time interval $0 < t < T$, the wavefunction (2.25) is changed into $\psi_s(\mathbf{k}) \exp(-i\varphi)$, where φ is Berry's phase given by

$$\varphi = -i \int_0^T dt\, \mathbf{F}_{s\mathbf{k}(t)}^{\dagger} \frac{d}{dt} \mathbf{F}_{s\mathbf{k}(t)} = -\pi. \tag{2.31}$$

This shows that the rotation in the **k** space by 2π leads to the change in the phase by $-\pi$, i.e., a sign change. Note that $R^{-1}[\theta(\mathbf{k})]|s\rangle$ is obtained from Eq. (2.25) by continuously varying the direction of **k** including Berry's phase. Note also that the signature change occurs only when the closed contour encircles the origin $\mathbf{k} = 0$ but not when the contour does not contain $\mathbf{k} = 0$, showing the prepense of a singularity at $\mathbf{k} = 0$. This topological singularity at $\mathbf{k} = 0$ causes various zero-mode anomalies as will be discussed in the following as well as the absence of backscattering leading to the perfect conductance in metallic carbon nanotubes [17, 18].

2.2.3 *Landau Levels in Magnetic Fields*

A singularity at $\varepsilon = 0$ manifests itself in magnetic field B even in classical mechanics. The equation of motion gives the cyclotron frequency $\omega_c(\varepsilon) = eBv^2/c\varepsilon$. The cyclotron frequency diverges and changes its signature at $\varepsilon = 0$ [24, 45]. In quantum mechanics $\hat{k}_x$ and $\hat{k}_y$ satisfy the commutation relation $[\hat{k}_x, \hat{k}_y] = -i/l^2$, where l is the magnetic length given by $l = \sqrt{c\hbar/(eB)}$. Semiclassically, the Landau levels can be obtained by the condition

$$\oint k_x dk_y = \pm \frac{2\pi}{l^2} \left(|n| + \frac{1}{2} \right), \tag{2.32}$$

as $\varepsilon_n = \text{sgn}(n)\sqrt{|n| + \frac{1}{2}}\,\hbar\omega_B$ with integer n, where

$$\hbar\omega_B = \frac{\sqrt{2}\gamma}{l}. \tag{2.33}$$

Because of the uncertainty principle, $k^2 = 0$ is not allowed and there is no Landau level at $\varepsilon = 0$. However, a full quantum mechanical treatment gives

$$\varepsilon_n = \text{sgn}(n)\sqrt{|n|}\,\hbar\omega_B, \tag{2.34}$$

leading to the formation of Landau levels at $\varepsilon = 0$, first noted by McClure in 1956 [11]. This can be understood by the cancellation of factor $1/2$ in Eq. (2.32) by Berry's phase corresponding to the rotation in the **k** space.

Define $a = (l/\sqrt{2})(\hat{k}_x - i\hat{k}_y)$ and $a^\dagger = (l/\sqrt{2})(\hat{k}_x + i\hat{k}_y)$. Then, we have $[a, a^\dagger] = 1$. In terms of these operators the Hamiltonian for the K point is rewritten as

$$\mathcal{H}_0 = \frac{\sqrt{2}\gamma}{l}\begin{pmatrix} 0 & a \\ a^\dagger & 0 \end{pmatrix}. \tag{2.35}$$

We shall define a function $h_n(x, y)$ such that

$$h_n(x, y) = \frac{(a^\dagger)^n}{\sqrt{n!}}\,h_0(x, y), \tag{2.36}$$

with

$$a\,h_0(x, y) = 0. \tag{2.37}$$

Then, we have

$$a^\dagger h_n = \sqrt{n+1}\,h_{n+1}, \quad a\,h_{n+1} = \sqrt{n+1}\,h_{n+1}, \quad a^\dagger a\,h_n = n\,h_n. \tag{2.38}$$

Therefore, there is a Landau level with vanishing energy $\varepsilon_0 = 0$ with wave function

$$\mathbf{F}_0^K = \begin{pmatrix} 0 \\ h_0 \end{pmatrix}. \tag{2.39}$$

Other Landau levels have wave function

$$\mathbf{F}_n^K = \frac{1}{\sqrt{2}}\begin{pmatrix} \text{sgn}(n)h_{|n|-1} \\ h_{|n|} \end{pmatrix}, \tag{2.40}$$

where $n = \pm 1, \pm 2, \dots$.

For the K′ point, we should exchange a and $a^\dagger$ in Hamiltonian (2.35). Then, we have

$$\mathbf{F}_0^{K'} = \begin{pmatrix} h_0 \\ 0 \end{pmatrix}, \tag{2.41}$$

$$\mathbf{F}_n^{K'} = \frac{1}{\sqrt{2}} \begin{pmatrix} h_{|n|} \\ \mathrm{sgn}(n)h_{|n|-1} \end{pmatrix}, \quad (n = \pm 1, \pm 2, \ldots). \tag{2.42}$$

The presence of the Landau level at $\varepsilon = 0$ independent of the magnetic-field strength is a remarkable feature of the Weyl equation, leading to a divergent magnetic susceptibility as discussed below.

2.2.4 *Effects of Bandgap Opening*

In the presence of potential difference 2Δ between the A and B sites, the Hamiltonian becomes

$$\mathcal{H}_0 = \begin{pmatrix} \Delta & \gamma(\hat{k}_x - i\hat{k}_y) \\ \gamma(\hat{k}_x + i\hat{k}_y) & -\Delta \end{pmatrix}. \tag{2.43}$$

Such potential asymmetry can arise when graphene is placed on a certain substrate material. In fact, bandgap opening is observed in graphene epitaxially grown on a SiC substrate [46, 47]. From a theoretical point of view, the singular behavior in ideal graphene with vanishing gap is better understood by taking the limit $\Delta \to 0$, as will be shown below. We can safely assume $\Delta \geq 0$ without loss of generality.

The energy band becomes

$$\varepsilon_s(p) = s\sqrt{\gamma^2 k^2 + \Delta^2}, \quad (s = \pm 1), \tag{2.44}$$

and the density of states becomes [48]

$$D(\varepsilon) = \frac{g_s g_v |\varepsilon|}{2\pi\gamma^2}\theta(|\varepsilon| - |\Delta|), \tag{2.45}$$

where $\theta(t)$ is a step function, defined by

$$\theta(t) = \begin{cases} 1 \ (t > 0); \\ 0 \ (t < 0). \end{cases} \tag{2.46}$$

Figure 2.4 shows the energy bands and the density of states for nonzero Δ.
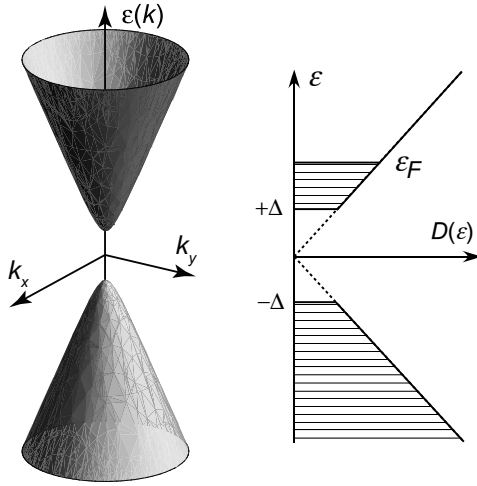
Figure 2.4 The energy bands in the vicinity of the K and K' points and the density of states in graphene with nonzero gap.

In magnetic field B perpendicular to the system, the Landau levels at the K point become

$$\varepsilon_n^K = \begin{cases} \text{sgn}(n)\sqrt{(\hbar\omega_B)^2|n| + \Delta^2} & (n = \pm1, \pm2, \cdots); \\ -\Delta & (n = 0), \end{cases} \tag{2.47}$$

and at the K' point

$$\varepsilon_n^{K'} = \begin{cases} \text{sgn}(n)\sqrt{(\hbar\omega_B)^2|n| + \Delta^2} & (n = \pm1, \pm2, \cdots); \\ +\Delta & (n = 0). \end{cases} \tag{2.48}$$

The Landau level $n = 0$ lies just at the top of the valence band for the K point and at the bottom of the conduction band for the K' point. The Landau levels of $n \neq 0$ are doubly degenerate between the K and K' valleys. Figure 2.5 shows some examples of Landau levels for $\Delta = 0$ and $\Delta > 0$.

2.3 Magnetic Properties

2.3.1 *Singular Diamagnetism*

The unique Landau-level structure gives rise to a singular diamagnetism [11], that is the origin of large diamagnetic susceptibility of
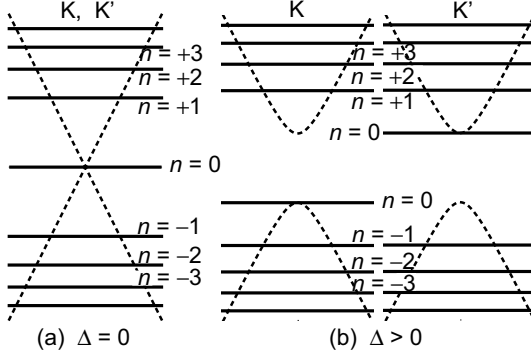
Figure 2.5 Landau levels in graphene with potential asymmetry Δ. (a) $\Delta = 0$. (b) $\Delta > 0$.

bulk graphite [49, 50]. The thermodynamic function Ω is given by

$$\Omega = -k_B T \frac{g_s g_v}{2\pi l^2} \sum_n \varphi(\varepsilon_n),$$

$$\varphi(\varepsilon) = \ln\left\{1 + \exp[\beta(\zeta - \varepsilon)]\right\}, \tag{2.49}$$

where T is the temperature, k_B the Boltzmann constant, $\beta = 1/k_B T$, and ζ the chemical potential. Let n_s be the electron concentration. Then, the free energy is written as

$$F = n_s \zeta + \Omega. \tag{2.50}$$

With the use of the relation $n_s = -(\partial \Omega / \partial \zeta)_B$, the magnetization is given by

$$M = -\left(\frac{\partial F}{\partial B}\right)_{n_s} = -\left(\frac{\partial \Omega}{\partial B}\right)_{\zeta}. \tag{2.51}$$

Therefore, susceptibility χ, defined by $M = \chi B$ for small B, can be obtained by calculating Ω up to the order of B^2.

The thermodynamic function is rewritten as

$$\Omega = -k_B T \frac{g_s g_v}{2\pi l^2} \sum_{n=0}^{\infty} g(\hbar\omega_B \sqrt{n})\left(1 - \frac{1}{2}\delta_{n0}\right) \ln$$

$$\times \left[1 + 2e^{\beta\zeta}\cosh(\beta\hbar\omega_B \sqrt{n}) + e^{2\beta\zeta}\right], \tag{2.52}$$

where $1/2\pi l^2$ is the degeneracy of a Landau level due to guiding centers and $g(\varepsilon)$ is a cutoff function that decays smoothly but sufficiently rapidly in such a way that the summation converges. In

order to expand Ω in terms of $\hbar\omega_B$, let us consider a smooth function $F(x)$ and its integral

$$\int_0^\infty F(x)dx = \int_0^{h/2} F(x)dx + \sum_{j=1}^\infty \int_{-h/2}^{h/2} F(x+hj)dx, \quad (2.53)$$

where h is a small positive number. By expanding this with respect to h, we have

$$h\left[\frac{1}{2}F(0)+\sum_{j=1}^\infty F(x+hj)\right] = \int_0^\infty F(x)dx - \frac{1}{12}h^2\left[F'(0)+\frac{1}{2}F'(\infty)\right],$$

$$(2.54)$$

up to the second order in h.

The desired expansion in $\hbar\omega_B$ is performed by letting $h = (\hbar\omega_B)^2$, $x = nh$, and

$$F(x) = g(\sqrt{x})\ln\left[1 + 2\exp(\beta\zeta)\cosh(\beta\sqrt{x}) + \exp(2\beta\zeta)\right]. \quad (2.55)$$

Then, we immediately have

$$\Omega = \Omega_0 + \Delta\Omega, \quad (2.56)$$

where Ω_0 is the thermodynamic potential in the absence of a magnetic field and

$$\Delta\Omega = \frac{1}{12}\frac{g_v g_s(\hbar\omega_B)^2}{2\pi l^2}\frac{\beta\exp(\beta\zeta)}{[1+\exp(\beta\zeta)]^2}$$

$$= \frac{g_v g_s \gamma^2}{12\pi l^4}\int_{-\infty}^\infty \left(-\frac{\partial f(\varepsilon)}{\partial\varepsilon}\right)\delta(\varepsilon)d\varepsilon, \quad (2.57)$$

where $f(\varepsilon)$ is the Fermi distribution function. The susceptibility becomes

$$\chi = \int_{-\infty}^\infty \left(-\frac{\partial f(\varepsilon)}{\partial\varepsilon}\right)\chi(\varepsilon)d\varepsilon, \quad (2.58)$$

with

$$\chi(\varepsilon) = -\frac{g_v g_s \gamma^2}{6\pi}\left(\frac{e}{c\hbar}\right)^2\delta(\varepsilon). \quad (2.59)$$

This singular susceptibility is characteristic to graphene and obtained first by McClure [11] and later by many others [51–53].

Consider the average contribution of states around ε_n ($|n| \gg 1$) to the thermodynamic potential in the weak-field limit. We have

$$\int_{-1/2}^{1/2} \text{sgn}(n)\hbar\omega_B\sqrt{|n|+t}\,\varphi\left[\text{sgn}(n)\hbar\omega_B\sqrt{|n|+t}\right]dt$$

$$= \varphi(\varepsilon_n) + \frac{\beta}{96}(\hbar\omega_B)^4[\varepsilon_n^{-3}f(\varepsilon_n) - \varepsilon_n^{-2}f'(\varepsilon_n)] + \cdots. \quad (2.60)$$

Therefore, the change in the thermodynamic potential in a magnetic field becomes

$$\Delta\Omega = \frac{g_v g_s}{2\pi l^2} \frac{(\hbar\omega_B)^2}{48} \int_{-\infty}^{\infty} \text{sgn}(\varepsilon)[\varepsilon^{-2} f(\varepsilon) - \varepsilon^{-1} f'(\varepsilon)]d\varepsilon. \quad (2.61)$$

When the Fermi level lies well away from $\varepsilon = 0$, the integral vanishes identically and therefore the susceptibility vanishes.

At $\varepsilon = 0$, the integrand becomes singular and gives the "paramagnetic" contribution

$$\Delta\Omega = -\frac{g_v g_s}{2\pi l^2} \frac{1}{24} (\hbar\omega_B)^2 \int_{-\infty}^{\infty} \left(-\frac{\partial f(\varepsilon)}{\partial\varepsilon} \right) \delta(\varepsilon) d\varepsilon. \quad (2.62)$$

In fact, we have

$$\int_0^{\infty} \left(\frac{f(\varepsilon)}{\varepsilon^2} - \frac{f'(\varepsilon)}{\varepsilon} \right) d\varepsilon - \int_{-\infty}^0 \left(\frac{f(\varepsilon)}{\varepsilon^2} - \frac{f'(\varepsilon)}{\varepsilon} \right) d\varepsilon$$

$$= \lim_{\varepsilon \to +0} \left(\frac{f(\varepsilon)}{\varepsilon} + \frac{f(-\varepsilon)}{-\varepsilon} \right) = 2f'(0). \quad (2.63)$$

For $n = 0$, the average contribution to the thermodynamic potential in the weak-field limit becomes

$$\int_{-1/2}^{1/2} \varphi[\text{sgn}(t)\hbar\omega_B\sqrt{|t|}]dt = \frac{1}{8}(\hbar\omega_B)^2 \varphi''(0) + \cdots$$

$$= -\frac{\beta}{8}(\hbar\omega_B)^2 f'(0) + \cdots, \quad (2.64)$$

giving

$$\Delta\Omega = \frac{g_v g_s}{2\pi l^2} \frac{1}{8} (\hbar\omega_B)^2 \int_{-\infty}^{\infty} \left(-\frac{\partial f(\varepsilon)}{\partial\varepsilon} \right) \delta(\varepsilon) d\varepsilon. \quad (2.65)$$

By adding the contribution from $n \neq 0$ given by Eq. (2.62), we have the result given by Eq. (2.57). This shows clearly that the presence of the Landau level at $\varepsilon = 0$ is the origin of the singular behavior of the susceptibility.

2.3.2 *Effects of Bandgap Opening*

It is instructive to consider diamagnetic response in the presence of nonzero gap Δ. In this case, we should replace $\hbar\omega_B\sqrt{n}$ with

$\sqrt{(\hbar\omega_B)^2|n| + \Delta^2}$ in Eq. (2.52). Then, we immediately obtain [22]

$$\chi(\varepsilon) = -\frac{g_v g_s \gamma^2}{6\pi}\left(\frac{e}{c\hbar}\right)^2 \frac{\theta(\Delta - |\varepsilon|)}{2\Delta}. \tag{2.66}$$

This agrees with Eq. (2.59) for $\Delta \to 0$.

Because the Hamiltonian is equivalent to that of a Dirac electron with a nonzero mass, the magnetic susceptibility around the band edge should correspond to that of a conventional electron in vacuum. This is clearly illustrated by the effective Hamiltonian expanded in the vicinity of $\mathbf{k} = 0$. For the conduction band, $s = +1$, the effective Hamiltonian for the A site near the band bottom ($\varepsilon = \Delta$) is written apart from the constant energy as

$$\mathcal{H}^K \approx \frac{\gamma^2}{2\Delta}\hat{k}_-\hat{k}_+ = \frac{\hbar^2\hat{\mathbf{k}}^2}{2m^*} - \frac{1}{2}g^*\mu_B B, \tag{2.67}$$

$$\mathcal{H}^{K'} \approx \frac{\gamma^2}{2\Delta}\hat{k}_-\hat{k}_+ = \frac{\hat{\mathbf{k}}^2}{2m^*} + \frac{1}{2}g^*\mu_B B, \tag{2.68}$$

where μ_B is the Bohr magneton, given by $e\hbar/(2mc)$ with m being the free electron mass, and we used the relation $[\hat{k}_x, \hat{k}_y] = i/l^2$ and defined

$$m^* = \frac{\hbar^2\Delta}{\gamma^2}, \quad g^* = 2\frac{m}{m^*}. \tag{2.69}$$

The last term in each Hamiltonian can be regarded as the pseudo-spin Zeeman term, where the different valleys K and K' serve as pseudo-spin up ($\xi = +1$) and down ($\xi = -1$), respectively. This shows that electrons at the K and K' points have intrinsic magnetic moment perpendicular to the graphene sheet in agreement with the self-rotation of wave packet [54, 55]. The combined Hamiltonian is written as

$$\mathcal{H} \approx \frac{\hat{\mathbf{k}}^2}{2m^*} - \frac{\xi}{2}g^*\mu_B B. \tag{2.70}$$

Obviously, the pseudo-spin Zeeman term gives the Pauli paramagnetism and the first term containing $\hat{\mathbf{k}}^2$ gives the Landau diamagnetism in the usual form as

$$\chi_P(\varepsilon) = \left(\frac{g^*}{2}\right)^2\mu_B^2 D(\varepsilon), \tag{2.71}$$

$$\chi_L(\varepsilon) = -\frac{1}{3}\left(\frac{m}{m^*}\right)^2\mu_B^2 D(\varepsilon), \tag{2.72}$$

with density of states

$$D(\varepsilon) = \frac{g_v g_s m^*}{2\pi\hbar^2}\,\theta(\varepsilon). \tag{2.73}$$

The total susceptibility $\chi_P + \chi_L$ actually agrees with the amount of the jump at the conduction band bottom in $\chi(\varepsilon)$ of Eq. (2.66). Because $g = 2m/m^*$ in the present case, we have $\chi_L = -\chi_P/3 \propto 1/m^*$ as in the free electron, giving the paramagnetic susceptibility in total. Therefore the susceptibility exhibits a discrete jump toward the paramagnetic direction when the Fermi energy moves off the Dirac point. The jump height goes to infinity as the gap closes, because the susceptibility is inversely proportional to the effective mass.

In the original Hamiltonian, the Landau-level energies can be rewritten as

$$\varepsilon_{\xi,s,n'} = s\sqrt{(\hbar\omega_B)^2\left(n' + \frac{1}{2} + \frac{\xi s}{2}\right) + \Delta^2} \quad (n' = 0, 1, 2, \cdots). \tag{2.74}$$

For the conduction band, the levels of the same n' with opposite pseudo-spins $\xi = \pm 1$ share the same Landau level function $\phi_{n'}$ on the A site, on which the states near the conduction-band bottom $(\varepsilon = \Delta)$ have most of the amplitude. For the valence band, similarly, n' describes the index of the Landau-level function at the B site. The above is nothing but the Landau level of a (two-dimensional) electron in vacuum.

2.3.3 *Magnetic Screening and Mirroring*

Graphene exhibits singular diamagnetism also in non-uniform magnetic fields [21]. We apply a magnetic field perpendicular to the layer $B(\mathbf{r}) = B(\mathbf{q})\exp(i\mathbf{q}\cdot\mathbf{r}) + \text{c.c.}$, where 'c.c.' stands for complex conjugate. Within the linear response, the Fourier-transforms of induced current density $\mathbf{j}(\mathbf{r}) = \mathbf{j}(\mathbf{q})\exp(i\mathbf{q}\cdot\mathbf{r}) + \text{c.c.}$ and $\mathbf{A}(\mathbf{r}) = \mathbf{A}(\mathbf{q})\exp(i\mathbf{q}\cdot\mathbf{r}) + \text{c.c.}$ are related by

$$j_\mu(\mathbf{q}) = \sum_{\nu=x,y} K_{\mu\nu}(\mathbf{q})A_\nu(\mathbf{q}), \quad (\mu = x, y), \tag{2.75}$$

with response function $K_{\mu\nu}(\mathbf{q})$. The gauge invariance for $\mathbf{A}(\mathbf{r})$ requires $\sum_\nu K_{\mu\nu}(\mathbf{q})\,q_\nu = 0$. The continuous equation in the static

system, $\vec{\nabla} \cdot \mathbf{j}(\mathbf{r}) = 0$, imposes another constraint $\sum_\mu q_\mu K_{\mu\nu}(\mathbf{q}) = 0$. To meet both requirements, tensor $K_{\mu\nu}(\mathbf{q})$ needs to be in the form,

$$K_{\mu\nu}(\mathbf{q}) = K(\mathbf{q})\left(\delta_{\mu\nu} - \frac{q_\mu q_\nu}{q^2}\right). \tag{2.76}$$

On the other hand, because $\vec{\nabla} \cdot \mathbf{j}(\mathbf{r}) = 0$, we can express $\mathbf{j}(\mathbf{r})$ as

$$j_x = c\frac{\partial m}{\partial y}, \quad j_y = -c\frac{\partial m}{\partial x}, \tag{2.77}$$

with $m(\mathbf{r})$ being the local magnetic moment perpendicular to the layer. In the linear response, its Fourier transform is written as

$$m(\mathbf{q}) = \chi(\mathbf{q})B(\mathbf{q}), \tag{2.78}$$

with magnetic susceptibility $\chi(\mathbf{q})$. Equations (2.75) and (2.78) are complementary, and both response functions $\chi(\mathbf{q})$ and $K(\mathbf{q})$ are related by

$$\chi(\mathbf{q}) = \frac{1}{cq^2}K(\mathbf{q}). \tag{2.79}$$

The Hamiltonian becomes $\mathcal{H} = \mathcal{H}_0 + \delta\mathcal{H}$ with $\delta\mathcal{H} = (e\gamma/c\hbar)\vec{\sigma} \cdot \mathbf{A}(\mathbf{r})$. The local current density at $\mathbf{r}_0$ is calculated as the expectation value of current-density operator $\hat{\mathbf{j}}(\mathbf{r}_0) = (e\gamma/\hbar)\,\vec{\sigma}\,\delta(\mathbf{r} - \mathbf{r}_0)$ over the occupied states. In the first order perturbation in $\delta\mathcal{H}$, we have

$$K_{\mu\nu}(\mathbf{q}) = -\frac{g_s g_v e^2 \gamma^2}{c\hbar^2}\frac{1}{L^2}\sum_{ss'\mathbf{k}}\frac{f(\varepsilon_{s\mathbf{k}}) - f(\varepsilon_{s'\mathbf{k+q}})}{\varepsilon_{s\mathbf{k}} - \varepsilon_{s'\mathbf{k+q}}}$$

$$\times(\mathbf{F}_{s\mathbf{k}}^\dagger \sigma_\nu \mathbf{F}_{s'\mathbf{k+q}})(\mathbf{F}_{s'\mathbf{k+q}}^\dagger \sigma_\mu \mathbf{F}_{s\mathbf{k}}). \tag{2.80}$$

At the zero temperature, we can explicitly calculate this to obtain

$$\chi(q) = -\frac{g_s g_v e^2 \gamma}{16\hbar c^2 \hbar}\frac{1}{q}\,\theta(q - 2k_F)$$

$$\times\left[1 + \frac{2}{\pi}\frac{2k_F}{q}\sqrt{1 - \left(\frac{2k_F}{q}\right)^2} - \frac{2}{\pi}\sin^{-1}\frac{2k_F}{q}\right], \tag{2.81}$$

where $k_F = |\varepsilon_F|/\gamma$ is the Fermi wave number. Significantly, $\chi(q)$ vanishes in range $q < 2k_F$, i.e., no magnetic moment is induced when the external field is smooth enough compared to the Fermi wavelength. At $\varepsilon_F = 0$, particularly, we have

$$\chi(q) = -\frac{g_s g_v e^2 \gamma}{16\hbar c^2 \hbar}\frac{1}{q}. \tag{2.82}$$
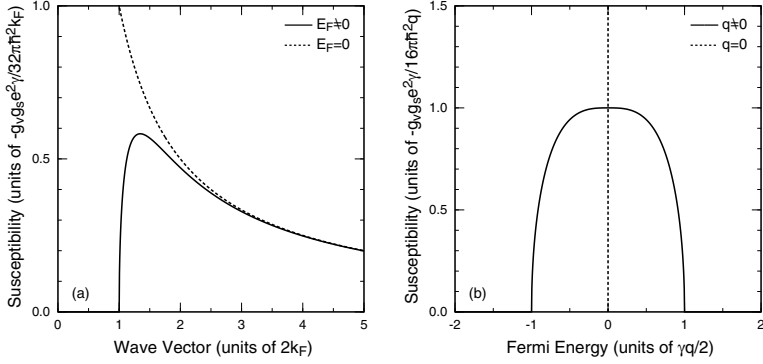
Figure 2.6 Diamagnetic susceptibility (a) versus wave vector q and versus the Fermi energy in ideal graphene.

The susceptibility of the carbon nanotube for a uniform field perpendicular to the axis has the equivalent expression of Eq. (2.82) where q is replaced by $2\pi/L$ with tube circumference L [56, 57]. Figure 2.6(a) shows a plot of $\chi(q)$ of Eq. (2.81) and Fig. 2.6(b) shows the dependence on the Fermi energy for a fixed q. The susceptibility suddenly starts from zero at $q = 2k_F$ and rapidly approaches the universal curve given by Eq. (2.82). As a function of ε_F at fixed q, it is nonzero only in a finite region satisfying $|\varepsilon_F| < \hbar v q/2$, and its integral over ε_F becomes constant $-g_s g_v e^2 \gamma^2/(6\pi c^2 \hbar^2)$. Thus, in the limit of $q \to 0$ it goes to

$$\chi(0) = -\frac{g_s g_v e^2 \gamma^2}{6\pi c^2 \hbar^2} \delta(\varepsilon_F). \qquad (2.83)$$

This agrees with the susceptibility against uniform magnetic field [11, 19].

Let us consider an undoped graphene ($\varepsilon_F = 0$) under a sinusoidal field $B(\mathbf{r}) = B_0 \cos qx$. With the susceptibility Eq. (2.81), the response current is calculated as

$$\mathbf{j}(\mathbf{r}) = -\frac{g_s g_v e^2 v B_0}{16\hbar c} \mathbf{e}_y \sin qx. \qquad (2.84)$$

The current induces a counter magnetic field that reduces the original field. The z component of the induced field on graphene becomes

$$B_{\text{ind}}(\mathbf{r}) = -\alpha_g B(\mathbf{r}), \quad \alpha_g = \frac{2\pi g_s g_v e^2 v}{16\hbar c^2}. \qquad (2.85)$$

Because the ratio is independent of q, Eq. (2.85) is actually valid for any external field $B(\mathbf{r})$, i.e., the magnetic field on the graphene is always reduced by the same factor $1 - \alpha_g$. This property holds whenever $\chi(q)$ is proportional to $1/q$. With the typical value $v \approx 1 \times 10^6$ m/s, α_g is estimated as $\approx 4 \times 10^{-5}$, showing that the counter field is much smaller than the original.

The argument of the magnetic field screening can be extended in the three dimensional field distribution. Let us suppose a situation when a certain magnetic object (permanent magnet or electric current) is located above the undoped graphene ($z > 0$), which produces an external magnetic field $\mathbf{B}(\vec{\rho})$ in three-dimensional space $\vec{\rho} = (x, y, z)$. Then, the following can easily be concluded: (i) On the other side of the graphene ($z < 0$), the induced field becomes $-\alpha_g \mathbf{B}(\vec{\rho})$, i.e., the external field is screened by the factor $1 - \alpha_g$. (ii) On the same side ($z > 0$), the induced field is given by $\alpha_g R_z[\mathbf{B}(x, y, -z)]$, where R_z is the vector inversion with respect to $z = 0$. Namely, this is equivalent to a field of the mirror image of the original object reflected with respect to $z = 0$, and reduced by α_g.

2.4 Optical Properties

With the use of the Kubo formula, the dynamical conductivity is given by

$$\sigma(\omega) = \frac{g_v g_s}{L^2} \left(\frac{e\gamma}{\hbar}\right)^2 \frac{\hbar}{i} \sum_{\alpha,\beta} \frac{|(\alpha|\sigma_x|\beta)|^2 (f_\alpha - f_\beta)}{(\varepsilon_\alpha - \varepsilon_\beta)(\varepsilon_\alpha - \varepsilon_\beta + \hbar\omega + i\delta)}, \quad (2.86)$$

where α and β are a set of quantum numbers specifying states, and δ is a positive infinitesimal. In ideal graphene, this can be separated into two parts:

$$\sigma(\omega) = \frac{g_v g_s}{L^2} \left(\frac{e\gamma}{\hbar}\right)^2 \frac{\hbar}{i} \left[\sum_{s\mathbf{k}} \frac{\partial f(\varepsilon_{sk})}{\partial \varepsilon_{sk}} \frac{|(s\mathbf{k}|\sigma_x|s\mathbf{k})|^2}{\hbar\omega + i\delta} \right.$$
$$\left. - \sum_{s \neq s', \mathbf{k}} \frac{|(s\mathbf{k}|\sigma_x|s'\mathbf{k})|^2 [f(\varepsilon_{sk}) - f(\varepsilon_{s'k})](\hbar\omega + i\delta)}{(\varepsilon_{sk} - \varepsilon_{s'k})[(\varepsilon_{sk} - \varepsilon_{s'k})^2 - (\hbar\omega + i\delta)^2]} \right], \quad (2.87)$$

where the first term in the bracket represents the Drude (intraband) part and the second the interband part.

In order to include effects of level broadening due to scatterers, we shall replace δ by $\hbar/\tau$, where τ is a relaxation time. Because of the energy dependence of the relaxation time, we shall assume $\tau = \tau(\varepsilon)$ with $\varepsilon = \varepsilon_F$ in the first term in the bracket of Eq. (2.86) and $\varepsilon = \hbar\omega/2$ in the second term, corresponding to the energy of the states giving a major contribution to the transition. Then, the dynamical conductivity at zero temperature is calculated as

$$
\sigma(\omega) = \frac{g_s g_v}{4} \frac{e^2}{4\hbar} \left[\frac{4}{\pi} \frac{i\varepsilon_F}{\hbar\omega + i[\hbar/\tau(\varepsilon_F)]} + 1 \right.
$$
$$
\left. + \frac{i}{\pi} \ln \frac{\hbar\omega + i[\hbar/\tau(\hbar\omega/2)] - 2\varepsilon_F}{\hbar\omega + i[\hbar/\tau(\hbar\omega/2)] + 2\varepsilon_F} \right]. \tag{2.88}
$$

As will be shown in the next section, for scatterers with potential range longer than the lattice constant and shorter than the electron wavelength, we have

$$
\frac{\hbar}{\tau(\varepsilon)} = \pi|\varepsilon|W, \tag{2.89}
$$

where W is the dimensionless parameter characterizing the strength and concentration of scatterers. Then, the frequency dependence of the dynamical conductivity is scaled by $\hbar\omega/\varepsilon_F$. Figure 2.7 shows $\sigma(\omega)$ as a function of $\hbar\omega/\varepsilon_F$ for several values of W [25].

The scaling of the dynamical conductivity $\sigma(\hbar\omega/\varepsilon_F)$ shows that $\sigma(\omega)$ exhibits a singular behavior at the point $(\omega, \varepsilon_F) = (0, 0)$. In fact, when we set $\omega = 0$ first, the static conductivity is given by

$$
\sigma(0) = \sigma_0 \equiv \frac{g_s g_v}{4} \frac{e^2}{\pi^2 \hbar} \frac{1}{W}, \tag{2.90}
$$

independent of the Fermi energy ε_F in agreement with the Boltzmann result [23]. When we set $\varepsilon_F = 0$ first with nonzero ω, on the other hand, the static conductivity at $\omega \to 0$ becomes

$$
\sigma_\infty \equiv \frac{g_s g_v}{4} \frac{e^2}{\pi \hbar}, \tag{2.91}
$$

which is the universal interband conductivity. The correct way is to let $\omega \to 0$ at each ε_F, leading to a singular jump of the static conductivity at $\varepsilon_F = 0$. The calculation in a self-consistent Born approximation shows that this anomaly manifests itself as a near singular dependence of σ on ε_F even if level broadening effects are
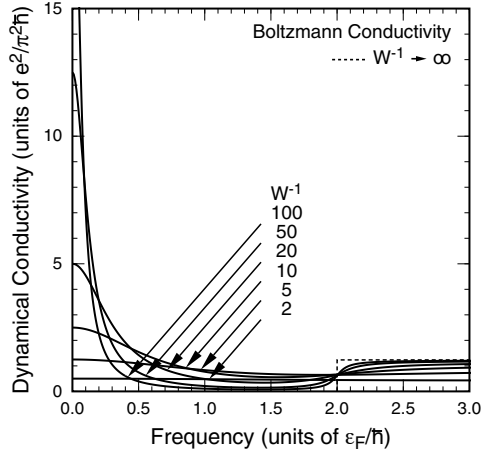
Figure 2.7 The dynamical conductivity calculated using the Boltzmann transport equation. The frequency is scaled by the Fermi energy. After Ref. [25].

included and that the conductivity at $\varepsilon_F = 0$ is given by a universal conductivity quantum $e^2/\pi^2\hbar$ as will be discussed in the following [23].

The transmission of light incident perpendicular to graphene sheet is given by [58]

$$T = \left|1 + \frac{2\pi}{c}\sigma(\omega)\right|^{-2} \approx 1 - \frac{4\pi}{c}\mathrm{Re}\,\sigma(\omega) = 1 - \frac{g_s g_v}{4}\frac{\pi e^2}{c\hbar}, \quad (2.92)$$

showing that the absorption is given by $\pi\alpha \approx 0.023$ independent of frequency or wavelength, with fine structure constant $\alpha \equiv e^2/(c\hbar) \approx 1/137$. This small absorption was experimentally observed [59, 60] and is often used to identify the number of layers of graphene flakes created by mechanical exfoliation.

2.5 Transport Properties

2.5.1 *Boltzmann Conductivity*

In this section, transport theory based on the Boltzmann equation will be reviewed [61]. The transport equation for the distribution

function $f_{s\mathbf{k}}^{\mathbf{E}}$ in the applied electric field $\mathbf{E}$ is given by

$$\frac{d\mathbf{k}}{dt} \cdot \frac{\partial f_{s\mathbf{k}}^{\mathbf{E}}}{\partial \mathbf{k}} = -\sum_{s'} \int \frac{d\mathbf{k}'}{(2\pi)^2} \left[f_{s\mathbf{k}}^{\mathbf{E}}(1 - f_{s'\mathbf{k}'}^{\mathbf{E}}) - f_{s'\mathbf{k}'}^{\mathbf{E}}(1 - f_{s\mathbf{k}}^{\mathbf{E}}) \right] W(s'\mathbf{k}', s\mathbf{k}),$$

$$(2.93)$$

with scattering probability

$$W(s'\mathbf{k}', s\mathbf{k}) = \frac{2\pi}{\hbar} \langle |V_{s'\mathbf{k}',s\mathbf{k}}|^2 \rangle \delta(\varepsilon_{s\mathbf{k}} - \varepsilon_{s'\mathbf{k}'}), \qquad (2.94)$$

where $V_{s'\mathbf{k}',s\mathbf{k}}$ is the matrix element of scattering potential and $\langle \cdots \rangle$ denotes the average over configurations of scatterers. We shall confine ourselves to the case of elastic scattering and therefore neglect interband processes ($s' \neq s$). To the lowest order in the applied electric field $\mathbf{E}$, we have

$$f_{s\mathbf{k}}^{\mathbf{E}} = f(\varepsilon_{s\mathbf{k}}) + g_{s\mathbf{k}}, \qquad (2.95)$$

where $f(\varepsilon)$ is the Fermi distribution function and $g_{s\mathbf{k}}$ is the deviation proportional to $\mathbf{E}$. Then, we have

$$\frac{d\mathbf{k}}{dt} \cdot \frac{\partial f_{s\mathbf{k}}^{\mathbf{E}}}{\partial \mathbf{k}} = -e\mathbf{E} \cdot \mathbf{v}_{s\mathbf{k}} \frac{\partial f}{\partial \varepsilon_{s\mathbf{k}}} - \frac{e}{c\hbar}(\mathbf{v}_{s\mathbf{k}} \times \mathbf{B}) \cdot \frac{\partial g_{s\mathbf{k}}}{\partial \mathbf{k}}, \qquad (2.96)$$

where $\mathbf{B}$ is the magnetic field perpendicular to the system and $\mathbf{v}_{s\mathbf{k}}$ is the velocity given by

$$\mathbf{v}_{s\mathbf{k}} = \frac{\partial \varepsilon_{s\mathbf{k}}}{\hbar \partial \mathbf{k}} = \frac{\gamma}{\hbar} \frac{s\mathbf{k}}{|\mathbf{k}|}. \qquad (2.97)$$

The vector product is defined as $\mathbf{v} \times \mathbf{B} = -\mathbf{B} \times \mathbf{v} = B(v_y, -v_x)$ for vector $\mathbf{v} = (v_x, v_y)$. The transport equation is rewritten as

$$e\mathbf{E} \cdot \mathbf{v}_{s\mathbf{k}} \left(-\frac{\partial f}{\partial \varepsilon_{s\mathbf{k}}} \right) = \frac{e}{c\hbar}(\mathbf{v}_{s\mathbf{k}} \times \mathbf{B}) \cdot \frac{\partial g_{s\mathbf{k}}}{\partial \mathbf{k}}$$

$$- \int \frac{d\mathbf{k}'}{(2\pi)^2}(g_{s\mathbf{k}} - g_{s\mathbf{k}'}) \frac{2\pi}{\hbar} \langle |V_{s\mathbf{k}',s\mathbf{k}}|^2 \rangle \delta(\varepsilon_{s\mathbf{k}} - \varepsilon_{s\mathbf{k}'}).$$

$$(2.98)$$

Let us introduce the transport relaxation time given by

$$\frac{\hbar}{\tau(\varepsilon_{s\mathbf{k}})} = 2\pi \int \frac{d\mathbf{k}'}{(2\pi)^2} \langle |V_{s\mathbf{k}',s\mathbf{k}}|^2 \rangle [1 - \cos(\theta_{\mathbf{k}} - \theta_{\mathbf{k}'})] \delta(\varepsilon_{s\mathbf{k}} - \varepsilon_{s\mathbf{k}'}),$$

$$(2.99)$$

and the cyclotron frequency

$$\omega_c(\varepsilon_{s\mathbf{k}}) = \frac{eBv^2}{c\varepsilon_{s\mathbf{k}}}. \qquad (2.100)$$

Then, the solution becomes

$$g_{sk} = -e\tau \left(-\frac{\partial f}{\partial \varepsilon_{sk}} \right) \frac{1}{1 + \omega_c^2 \tau^2} \mathbf{v}_{sk} \cdot \left(\mathbf{E} + \omega_c \tau \frac{\mathbf{B}}{B} \times \mathbf{E} \right), \quad (2.101)$$

with $\omega_c = \omega_c(\varepsilon_{sk})$ and $\tau = \tau(\varepsilon_{sk})$. It should be noted that the cyclotron frequency diverges in proportion to the inverse of the energy at zero energy and changes the sign corresponding to change in the carrier type from electron to hole.

Let us define

$$\bar{D} = \frac{g_s g_v}{2\pi\gamma^2} \int \left(-\frac{\partial f}{\partial \varepsilon} \right) |\varepsilon| d\varepsilon, \quad (2.102)$$

and the average of function $p(\varepsilon)$ by

$$\langle p(\varepsilon) \rangle \equiv \frac{1}{\bar{D}} \int \left(-\frac{\partial f}{\partial \varepsilon} \right) \frac{g_s g_v}{2\pi\gamma^2} |\varepsilon| p(\varepsilon) d\varepsilon. \quad (2.103)$$

Then, we have the diagonal conductivity

$$\sigma_{xx} = \sigma_{yy} = \frac{e^2 \gamma^2}{2\hbar^2} \bar{D} \left\langle \frac{\tau}{1 + \omega_c^2 \tau^2} \right\rangle, \quad (2.104)$$

and the Hall conductivity

$$\sigma_{xy} = -\sigma_{yx} = -\frac{e^2 \gamma^2}{2\hbar^2} \bar{D} \left\langle \frac{\omega_c \tau^2}{1 + \omega_c^2 \tau^2} \right\rangle. \quad (2.105)$$

These are essentially the same as the expressions in conventional semiconductors or metals except that ω_c depends strongly on the energy while the velocity remains independent.

The Hall coefficient is given by

$$R_H = -\frac{\sigma_{yx}}{B(\sigma_{xx}^2 + \sigma_{xy}^2)}, \quad (2.106)$$

and the Hall mobility is given by

$$\mu = c|R_H|\sigma_0, \quad (2.107)$$

in the limit $B \to 0$, where $\sigma_0 = \sigma_{xx}$ in the absence of a magnetic field. At zero temperature in weak magnetic fields, we have

$$R_H = -\frac{s}{n_s ec}, \quad (2.108)$$

with the electron concentration given by Eq. (2.13). The Hall mobility becomes

$$\mu_0 = \frac{ev^2}{\varepsilon_F} \tau(\varepsilon_F), \quad (2.109)$$

and then the conductivity is given by

$$\sigma_0 = n_s e \mu, \tag{2.110}$$

as in conventional two-dimensional systems.

For scatterers with potential $v(\mathbf{r})$, randomly distributed with concentration n_i per unit area, we have

$$\langle |V_{s'\mathbf{k}',s\mathbf{k}}|^2 \rangle = n_i |v(\mathbf{k}' - \mathbf{k})(\mathbf{F}_{s'\mathbf{k}'}^{\dagger} \cdot \mathbf{F}_{s\mathbf{k}})|^2, \tag{2.111}$$

with

$$(\mathbf{F}_{s\mathbf{k}}^{\dagger} \cdot \mathbf{F}_{s'\mathbf{k}'}) = \frac{1}{2} [\exp(i\theta_{\mathbf{k}} - i\theta_{\mathbf{k}'}) + ss'], \tag{2.112}$$

$$v(\mathbf{r}) = \int \frac{d\mathbf{q}}{(2\pi)^2} v(\mathbf{q}) \exp(i\mathbf{q} \cdot \mathbf{r}). \tag{2.113}$$

The transport relaxation time becomes

$$\frac{\hbar}{\tau(\varepsilon)} = 2\pi n_i \frac{|\varepsilon|}{2\pi\gamma^2} \int_0^\pi \frac{d\theta}{\pi} \frac{1}{2} (1 - \cos^2\theta) |v(q)|^2. \tag{2.114}$$

where $|v(q)|^2$ is the average over different directions of impurities in the case of anisotropic scatterers, i.e., $|v(q)|^2 = \langle |v(\mathbf{q})|^2 \rangle$, and $q = 2(|\varepsilon|/\gamma)\sin(\theta/2)$ in the integrand. On the other hand, the conventional relaxation time representing the electron life time is obtained from above by replacing $1 - \cos^2\theta$ with $1 + \cos\theta$, i.e.,

$$\frac{\hbar}{\tau_0(\varepsilon)} = 2\pi n_i \frac{|\varepsilon|}{2\pi\gamma^2} \int_0^\pi \frac{d\theta}{\pi} \frac{1}{2} (1 + \cos\theta) |v(q)|^2. \tag{2.115}$$

For scatterers with potential range smaller than the electron wavelength $\lambda = 2\pi/k = 2\pi\gamma/|\varepsilon|$, we can safely neglect the q dependence of $|v(q)|^2$ and set $|v(q)|^2 \approx v_i^2$. Then, we have

$$\frac{\hbar}{\tau(\varepsilon)} = \frac{\hbar}{2\tau_0(\varepsilon)} = \pi|\varepsilon| \frac{n_i v_i^2}{4\pi\gamma^2}. \tag{2.116}$$

This becomes Eq. (2.89), for the dimensionless parameter characterizing the strength of scattering

$$W = \frac{n_i v_i^2}{4\pi\gamma^2}. \tag{2.117}$$

The conductivity at zero temperature is given by Eq. (2.90), independent of the Fermi energy. This shows that graphene should be regarded as a metal rather than a semiconductor.
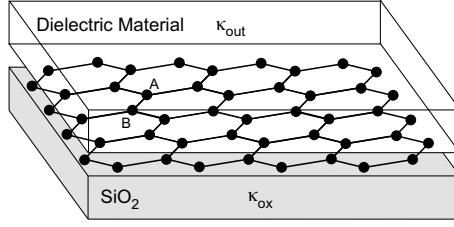
Figure 2.8 Schematic illustration of graphene on SiO_2 substrate covered by dielectric material on top.

2.5.2 *Charged Impurities*

We consider graphene on SiO_2 covered by dielectric material with dielectric constant κ_{out} on the top side as schematically illustrated in Fig. 2.8. For charged impurities located close to graphene layer, we have

$$v(q) = \frac{2\pi e^2}{\kappa q \varepsilon(q)}, \tag{2.118}$$

where κ is the effective dielectric constant determined by environmental conditions and $\varepsilon(q)$ represents the screening effect due to electrons in graphene. The static screening constant is given by the average of that of the substrate SiO_2, $\kappa_{ox} = 3.9$, and that of the covering material κ_{out} due to the image effect [62], i.e., $\kappa = (\kappa_{ox} + \kappa_{out})/2$.

Actually, we have to consider contributions of electrons in σ bands and π bands away from the Fermi level. This contribution is known to be $\kappa_0 \approx 2.4$ in bulk graphite [63], but is not known for the present system and may not be written as in Eq. (2.118). In spite of this, we shall use Eq. (2.118) assuming that κ can be larger than that estimated above.

The dielectric function of graphene is written as

$$\varepsilon(q) = 1 + \frac{2\pi e^2}{\kappa q} \Pi(q), \tag{2.119}$$

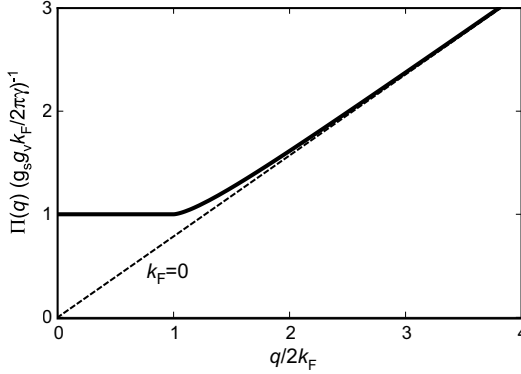where the polarization function at zero temperature is calculated as [45]

Figure 2.9 Polarization function $\Pi(q)$ in graphene. The dotted line represents pure interband contribution for vanishing electron and hole concentrations.

$$\Pi(q) = \begin{cases} \dfrac{g_s g_v}{2\pi\gamma} k_F & (q < 2k_F); \\ \dfrac{g_s g_v}{16\gamma} q + \dfrac{g_s g_v}{2\pi\gamma} k_F \left[1 - \left(\dfrac{1}{2} \sqrt{1 - \left(\dfrac{2k_F}{q} \right)^2} - \dfrac{q}{4k_F} \sin^{-1} \dfrac{2k_F}{q} \right) \right] & (q > 2k_F). \end{cases}$$

$$(2.120)$$

This is shown in Fig. 2.9. In the long-range limit $q = 0$, we have $\Pi(0) = D(\varepsilon_F)$ corresponding to the compressibility sum rule. For the relaxation time at zero temperature or at sufficiently low temperatures, we can safely replace $\Pi(q)$ with $\Pi(0)$ because $q \leq 2k_F$, i.e., we can use the Thomas–Fermi approximation.

The transport relaxation time becomes

$$\tau(\varepsilon) = \frac{n_s}{\pi g_s g_v n_i} \frac{\hbar}{|\varepsilon|} H, \qquad (2.121)$$

with

$$H^{-1} = \int_0^\pi \frac{d\theta}{\pi} \frac{1}{2}(1 - \cos^2\theta) \left(g_s g_v + \frac{\kappa\gamma}{e^2} \frac{q}{k_F} \right)^{-2}, \qquad (2.122)$$

where $q = 2k_F \sin(\theta/2)$ and $e^2/\kappa\gamma$ is the effective fine structure constant in graphene, i.e.,

$$\frac{e^2}{\kappa\gamma} = \frac{1}{\kappa} \frac{c}{v} \frac{e^2}{\hbar c} \approx \frac{300}{\kappa} \frac{1}{137}, \qquad (2.123)$$

for $v/c \approx 1/300$. The conventional relaxation time representing the electron life time is obtained from above by replacing $1 - \cos^2 \theta$ with $1 + \cos \theta$.

The mobility becomes

$$\mu_0 = \frac{e}{4\pi^2 \hbar n_{\mathrm{i}}} H, \qquad (2.124)$$

which is independent of n_s. The conductivity becomes

$$\sigma_0 = \frac{e^2}{4\pi^2 \hbar} \frac{n_{\mathrm{s}}}{n_{\mathrm{i}}} H, \qquad (2.125)$$

which is proportional to n_{s}.

The Boltzmann transport equation, as well as the Einstein relation, gives $\sigma \propto e^2 \tau(\varepsilon_F) v(\varepsilon_F)^2 D(\varepsilon_F)$. In conventional systems characterized by constant effective mass m^*, we have $\varepsilon_F = m^* v(\varepsilon_F)^2/2$. With the use of $n_s \propto \varepsilon_F D(\varepsilon_F)$, this leads to the usual expression $\sigma = n_s e \mu$ with mobility $\mu = e\tau(\varepsilon_F)/m^*$, where n_s is the electron concentration.

In graphene, the velocity v is independent of ε_F or $m^* \propto \varepsilon_F$ if we assume $\varepsilon_F = m^* v^2/2$ as above. Further, the scattering probability $\hbar/\tau(\varepsilon_F)$ is proportional to the final-state density of states with a coefficient independent of ε_F. Because the density of states is proportional to ε_F, the relaxation time is inversely proportional to ε_F. As a result, the mobility μ becomes proportional to $\varepsilon_F^{-2} \propto n_s^{-1}$, leading to the conductivity independent of the Fermi energy and the electron concentration.

In the case of charged-impurity scattering, the matrix element itself is proportional to the inverse of the Fermi energy, leading to $W \propto \varepsilon_F^{-2} \propto n_s^{-1}$. Consequently, the conductivity increases in proportion to the electron or hole concentration n_s as if there is a mobility independent of n_s [45, 64]. Note, however, that this does not change the situation that graphene should be regarded as a metal rather than a semiconductor.

2.5.3 Self-Consistent Born Approximation and Zero-Mode Anomalies

A more refined treatment has been performed for the density of states and the conductivity in a self-consistent Born approximation
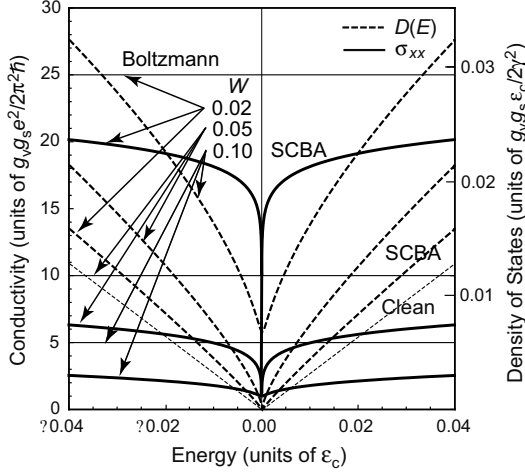
Figure 2.10 Some examples of the density of states (dashed lines) and the conductivity (solid lines), calculated in the self-consistent Born approximation (SCBA) for scatters with potential range smaller than the electron wavelength but larger than the lattice constant [23]. The thin horizontal lines denote the Boltzmann conductivity and the thin dotted line denoted as 'Clean' represents the density of states in clean graphene.

[58, 66, 66], in which level-broadening effects are properly taken into account [23]. Figure 2.10 shows some examples of the results. The density of states becomes nonzero at $\varepsilon = 0$ because of level broadening and is also enhanced due to level repulsion effect near $\varepsilon = 0$. Further, the conductivity at $\varepsilon_F = 0$ is given by

$$\sigma_{\min} = \frac{g_s g_v e^2}{2\pi^2 \hbar}, \qquad (2.126)$$

which is universal and independent of the scattering strength. The resulting conductivity varies smoothly across $\varepsilon_F = 0$ but exhibits a sharp jump in the limit of weak scattering ($W \ll 1$) from the Boltzmann result σ_0 for $\varepsilon \neq 0$ down to $\sigma_{\min}$ at $\varepsilon_F = 0$.

The energy scale characterizing this singularity in the vicinity of $\varepsilon_F = 0$ turns out to be

$$\varepsilon_0 = 2W\varepsilon_c e^{-1/2W}, \qquad (2.127)$$

where ε_c is the cutoff energy roughly corresponding to a half of the π-band width (~ 9 eV). This becomes extremely small in clean graphene with $W \ll 1$.
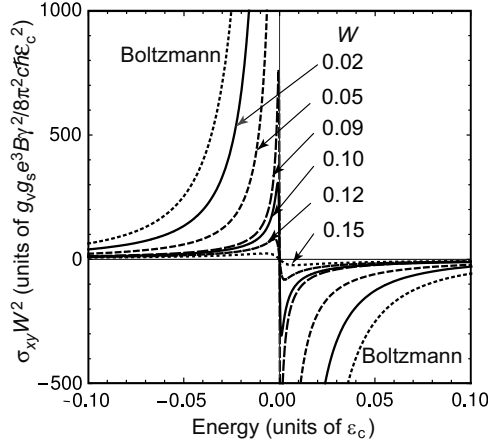
Figure 2.11 Some examples of the Hall conductivity as a function of the Fermi energy calculated in a self-consistent Born approximation for short-range scatterers. After Ref. [65].

As has been discussed in Section 2.5.1, in the Boltzmann theory, the Hall conductivity in weak magnetic field B is given by $\sigma_{xy} = -\omega_c \tau(\varepsilon_F)\sigma_0$, where ω_c is the classical cyclotron frequency given by $\omega_c(\varepsilon) = eBv^2/c\varepsilon$. The cyclotron frequency diverges at the Dirac point, showing the presence of singularity there. In spite of this singularity, the Hall coefficient is simply $R_H = -(n_s ec)^{-1}$ as in conventional systems. Similar calculations in the self-consistent Born approximation were recently performed for the weak-field Hall conductivity [65]. Figure 2.11 shows some examples of calculated σ_{xy}. The Hall conductivity behaves roughly as $-\varepsilon_F^{-1}$ outside of the region $|\varepsilon_F| > \varepsilon_0$, but is considerably reduced from the Boltzmann result. It varies almost linearly in the region $-\varepsilon_c < \varepsilon_F < +\varepsilon_c$ and crosses zero at the Dirac point.

Figure 2.12 shows the inverse Hall coefficient as a function of n_s. In clean systems such as $W < 0.1$, the Hall coefficient is essentially given by $R_H = -(n_s ec)^{-1}$ except in the critical region $|n_s| < n_s^0 = g_s g_v \varepsilon_0^2/4\pi\gamma^2$. In dirty systems such as $W > 0.1$, R_H^{-1} considerably deviates from $-n_s ec$ and also there seems to be a discrete jump in the values of R_H^{-1} extrapolated to $n_s = 0$ from the electron and hole sides. This jump may be regarded as effective carrier concentration
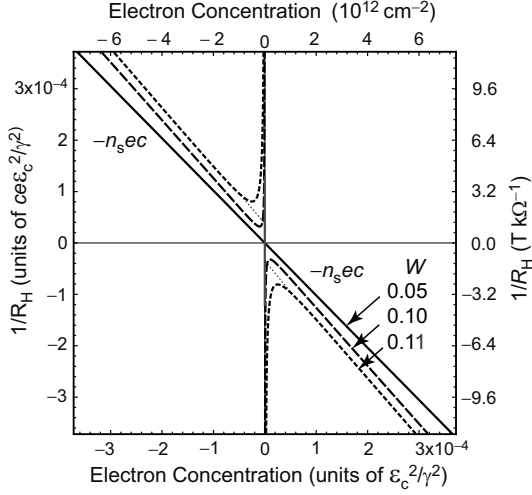
Figure 2.12 Some examples of the inverse of Hall coefficient R_H as a function of the electron concentration. With the decrease of W, R_H^{-1} approaches $-n_sec$. The thin solid lines are a linear extrapolation of the results for $W = 0.11$ toward $n_s = 0$. After Ref. [65].

associated with the nonvanishing density of states at the Dirac point due to disorder.

Experimentally, the conductivity increases almost linearly with n_s for sufficiently large n_s, showing that the effective scattering strength in actual graphene on SiO$_2$ substrate varies considerably with n_s. Most plausible scatterers giving rise to such strong n_s dependence are charged impurities [61, 64]. This strong dependence of W on n_s disappears when $|\varepsilon| < \varepsilon_0$, i.e., $|n_s| < n_s^0$, because of the level broadening leading to uncertainty in the effective kinetic energy of electrons. Experimental results [4] can be understood by assuming W, which is ~ 0.11 for $|\varepsilon_F| \lesssim \varepsilon_0$ and decreases in proportion to n_s^{-2} with increasing $|n_s|$. For $W = 0.1$, the broadening is $\Gamma_0 \sim 60$ meV. This Γ_0 is much larger than potential fluctuations ~ 25 meV estimated from observed electron–hole puddles based on ideal density of states [67], suggesting that puddles are actually not important in determining the transport in the vicinity of the Dirac point.
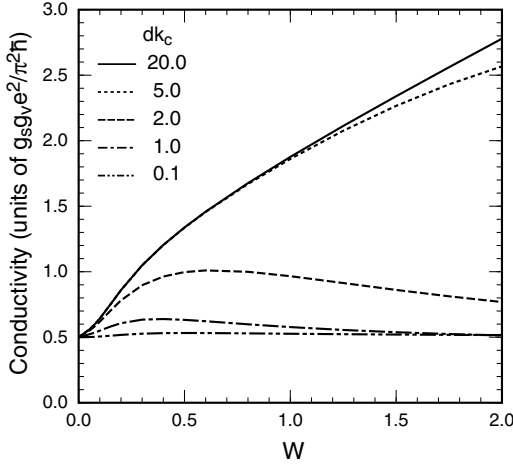
Figure 2.13 Calculated minimum conductivity at the Dirac point versus W for scatterers with Gaussian potential. After Ref. [68].

Calculations can be extended to the case of scatterers with long-range potential [68]. We consider, for example, scatterers with Gaussian potential $U(\mathbf{r}) = \sum_j (v_i/\pi d^2) \exp[-(\mathbf{r} - \mathbf{r}_j)^2/d^2]$ characterized by potential range d and strength v_i. The energy region affected strongly by the presence of scatterers is limited to $|\varepsilon| \lesssim \gamma/d$ because scattering becomes ineffective for $k > d^{-1}$. Therefore, for long-range scatterers, W is not restricted to small values like $W < 0.1$, but can be much larger.

Figure 2.13 shows the minimum conductivity at the Dirac point. For very short-range case $dk_c < 1$, the conductivity is nearly independent of W, where k_c is the cufoff momentum given by $\gamma k_c \sim \gamma_0$ corresponding to the region where the linear dispersion is approximately valid. For $dk_c > 1$, on the other hand, the conductivity increases with W, depending on dk_c. States at the Dirac point have higher k components because of strong forward scattering caused by long-range scatterers. These higher k states are weakly scattered in backward direction and therefore tend to have large contribution to the conductivity. For short-range scatterers, higher k components do not contribute much to the conductivity and the minimum conductivity remains small.
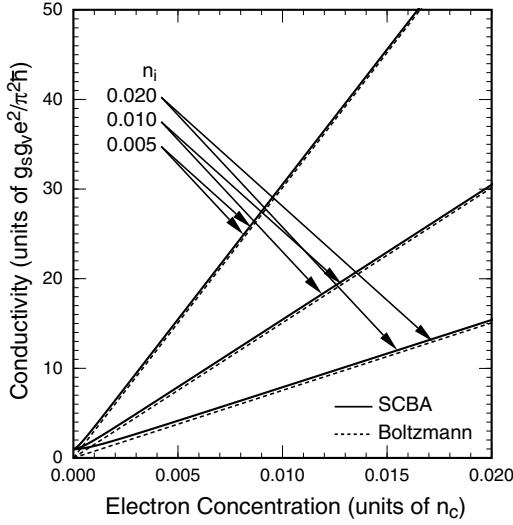
Figure 2.14 Calculated conductivity versus the electron concentration for charged scatterers. After Ref. [68].

Since the first experimental observation of the minimum conductivity [4], which is larger than the theoretical prediction [23, 69, 70], there have been various experimental [71–73] and theoretical works [74–81] to answer the question whether the minimum conductivity is really universal or not. The above clearly shows that the conductivity at the Dirac point is not universal but depends on the degree of the disorder for scatterers with long-range potential when the disorder is sufficiently large.

Calculations can be extended to the case of charged impurities when the screening effect is self-consistently included within a Thomas–Fermi approximation, i.e., the screening is given by the density of states at the Fermi level determined in a self-consistent manner [68]. Figure 2.14 shows the conductivity as a function of the electron density. Here, ε_c is the cutoff energy of the order of $3\gamma_0 \sim 9$ eV, where $-\gamma_0$ is the hopping integral in the simplest tight-binding model [83], and $n_c = \varepsilon_c^2/(4\pi\gamma^2)$ is the concentration roughly corresponding to an impurity per several unit cells. The conductivity is essentially the same as the Boltzmann conductivity and increases in proportion to n_s except that it approaches a nonzero
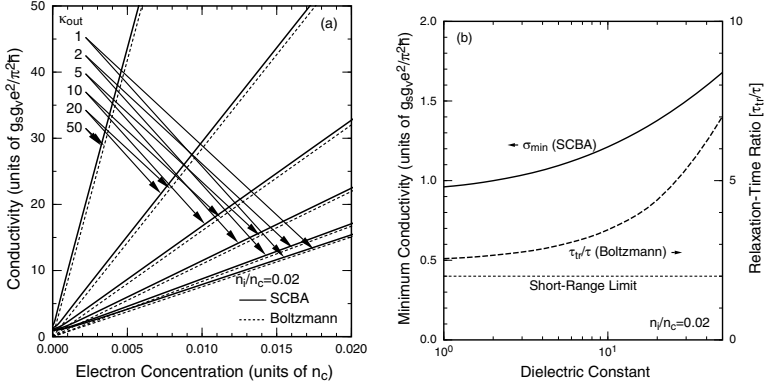
Figure 2.15 (a) Conductivity versus electron concentration for various values of the dielectric constant of dielectric material on top of graphene. (b) Minimum conductivity and the relaxation-time ratio as a function of dielectric constant κ_{out}. After Ref. [82].

value slightly larger than $2 \times \sigma_{min}$ at the Dirac point. This again shows that the minimum conductivity is not universal for realistic scatterers. More elaborate calculations are necessary for various scattering mechanisms and other quantities before reaching full understanding on the behavior of the minimum conductivity.

Calculations can also be extended to the case in the presence of dielectric environmental material [82]. Figure 2.15(a) shows some examples of calculated conductivity for $1 \leq \kappa_{out} \leq 50$. With the increase of κ_{out}, the conductivity does not increase so much, presumably due to the fact that the decrease of potential by dielectric screening is partly canceled by the reduction in the screening by electrons in graphene. Figure 2.15(b) shows the minimum conductivity at the Dirac point as a function of κ_{out}. It increases gradually with κ_{out}. The reason is that the effective potential tends to become of long range due to less screening by electrons in graphene.

Figure 2.15(b) also shows ratio of transport relaxation time τ determining the conductivity and self-energy relaxation time τ_0 corresponding to the inverse of the total scattering probability [82]. For short-range scatterers we have $\tau/\tau_0 = 2$ because of the absence of backscattering [23]. For $\kappa_{out} = 1$ without environmental dielectric

material, we have $2 < \tau/\tau_0 < 3$ not so much different from that for short-range scatterers. This shows that charged impurities should be regarded as short-range scatterers for $\kappa_{\text{out}} = 1$ in contrast to the claim otherwise [84]. For sufficiently large κ_{out}, for which τ/τ_0 is much larger than two, charged impurities tend to have the nature of long-range scatterers. Experiments under different dielectric environments were reported [85–87], but results vary among them and therefore seem to remain inconclusive yet.

2.5.4 *Resonant Scattering by Lattice Defects*

Direct and clear evidence for the presence of atomic defects in graphene layers, such as vacancies consisting of a single atom, two atoms adjacent to each other, etc., was experimentally demonstrated [88, 89]. Further, graphene is sensitive to adsorbed atoms partly because of their roles as strong scatterers as well as carrier doping [90–92]. The electron scattering by such localized defects with strong and short-range potential is quite interesting. In fact, the scattering of electrons by vacancies was studied in carbon nanotubes both in a tight-binding model and in an effective-mass approximation and was shown to depend critically on the difference in the number of vacancies at A and B sublattices when the strength of the potential is sufficiently large [93–98]. In nanotubes, resonance scattering by defects was experimentally observed [99–101] and various theoretical calculations based on first-principles [102–105] and tight-binding models [106, 107] were reported.

Effects of scattering by several closely located impurities with strong and short-range potential were theoretically studied recently [108]. It was shown that in a defect consisting of a single impurity, a quasi-bound state like a donor or acceptor state emerges near the Dirac point when the potential becomes extremely strong. In the case of AB pair impurities, the quasi-bound state splits into two and the resonance appears near the Dirac point for moderately strong scattering potential. In the case of defects consisting of many atoms, the number of resonances crossing $\varepsilon = 0$ when the potential strength is varied is that of AB pairs. Such resonance scattering can also be a candidate accounting for the experimental observation of the strong energy dependence of the conductivity in graphene.

Within a tight-binding model, a short-range impurity gives rise to change in local site energy u_0 measured from that of a carbon atom. This gives rise to a delta potential with strength $u = u_0\Omega_0$, where Ω_0 is the area of a unit cell. It is possible to calculate effective **k·p** Hamiltonian for such an impurity and formulate the calculation of scattering matrix T_S within the effective-mass scheme based on Green's function technique [108]. In the following, the scattering strength is represented by the effective scattering potential, V_S, giving the transport relaxation time τ, i.e.,

$$\frac{1}{\tau} = \frac{2\pi}{\hbar} \frac{1}{2} \sum_{v,v'} \int \frac{d\mathbf{k}'}{(2\pi)^2} n_i \left| \langle vs\mathbf{k}|T_S|v's\mathbf{k}'\rangle \right|^2_{\text{av}} (1 - \cos\theta_{\mathbf{k},\mathbf{k}'})\delta(\varepsilon_{s\mathbf{k}} - \varepsilon_{s\mathbf{k}'})$$

$$\equiv \frac{2\pi}{\hbar} n_i V_S^2 \frac{1}{2} \sum_{v,v'} \int \frac{d\mathbf{k}'}{(2\pi)^2} \delta(\varepsilon_{s\mathbf{k}} - \varepsilon_{s\mathbf{k}'}), \qquad (2.128)$$

where v and v' denote the K and K' points, n_i is the defect concentration, and $\theta_{\mathbf{k},\mathbf{k}'}$ is the angle between $\mathbf{k}$ and $\mathbf{k}'$.

Figure 2.16 shows some examples of effective potential V_S of a defect consisting of a single A site as a function of energy for $u > 0$. Results for $u < 0$ are obtained by mirror reflection with respect to $\varepsilon = 0$. A strong repulsive and attractive short-range impurity causes the appearance of a virtual bound state and its energy is denoted by a downward arrow. Actual peaks in the effective potential are slightly shifted to the zero-energy side because of the large density of states except at the Dirac point. In the limit $u \to \infty$, the bound states moves to $\varepsilon = 0$ and the effective potential diverges there. In this case, we have $V_S^{-1} \sim (|\varepsilon|/2\pi\gamma^2)\ln|\varepsilon|$, giving $\sigma \propto |n_s|$ apart from weak logarithmic dependence.

Figure 2.17 shows V_S of defect A_1B_1 consisting of a pair of neighboring A and B sites. Because of large splitting of bonding and antibonding combinations of bound states, the energy of antibonding state can lie close to the zero energy even for moderate values of u. Figure 2.17(a) shows that this state crosses the Dirac point at $u/\gamma_0\Omega_0 \approx 2.5$, where the scattering strength at the Dirac point diverges. With the further increase of u, the bound state goes into the conduction band and the scattering potential approaches a small value independent of u in the limit of infinitely large u.
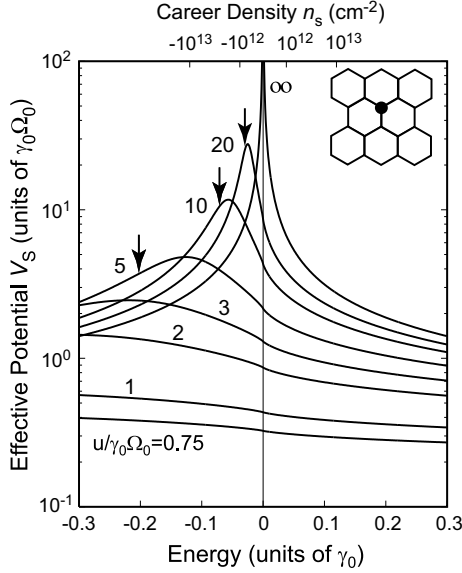
Figure 2.16 Some examples of effective potential V_S of defect A_1 as a function of energy for $u > 0$. The values of $u/\gamma_0\Omega_0$ are denoted in the figure. Results for $u < 0$ are obtained by mirror reflection with respect to $\varepsilon = 0$. The downward arrows indicate energy of a virtual bound state. A clear resonance enhancement becomes apparent for $u/\gamma_0\Omega_0 \gtrsim 10$. After Ref. [108].

Both analytic and numerical calculations for defect A_nB_m ($n \geq m \geq 0$) show the following: (i) The number of bound states that cross the Dirac point for moderate values of u is given by that of AB pairs, i.e., given by m. (ii) In the limit of sufficiently large u, energy of some bound states approaches the Dirac point unless $n = m$. For $n = m$, V_S approaches a small value independent of u and almost independent of energy. These conclusions can be confirmed in Fig. 2.18, which shows V_S of various defects as a function of the potential strength at the Dirac point.

2.5.5 *Crossover between Localization and Antilocalization*

In the presence of strong disorder, states are known to be localized and the conductivity vanishes at zero temperature. Because of the
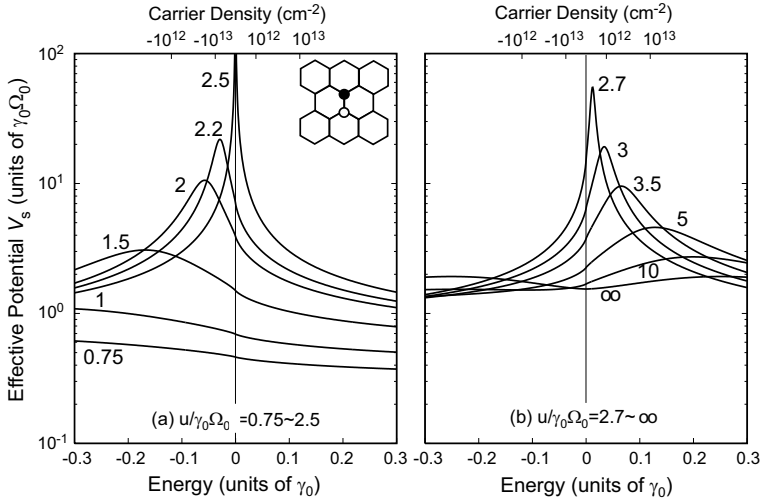
Figure 2.17 Some examples of V_S of defect A_1B_1 consisting of a pair of neighboring A and B sites. Divergent scattering occurs around $u/\gamma_0\Omega_0 \approx 2.5$ for which the antibonding resonance state crosses the Dirac point. After Ref. [108].
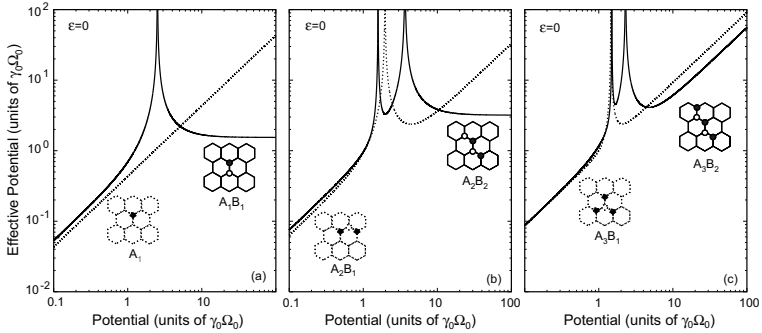

Figure 2.18 Some examples of V_S of various defects as a function of the potential strength at the Dirac point. After Ref. [108].

disorder, various spatial symmetries are all destroyed and only the symmetry related to time reversal may survive. The localization effect is known to vary strongly depending of this remaining

symmetry. The symmetry plays decisive roles in two dimensional systems, which are critical in localization according to scaling theory.

The Weyl equation (2.17) is invariant under a special time reversal operation S,

$$\mathbf{F}^S = K\mathbf{F}^*, \qquad (2.129)$$

where $\mathbf{F}^*$ represents the complex conjugate of the wave function $\mathbf{F}$ and K is an anti-unitary matrix $K = -i\sigma_y$ satisfying $K^2 = -1$. The corresponding operation for an operator P is given by $P^S = K\,^t P K^{-1}$, where $^t P$ stands for the transpose of P. This corresponds to the time reversal in systems with spin–orbit interaction and leads to

$$\mathbf{F}^{S^2} \equiv (\mathbf{F}^S)^S = -\mathbf{F}. \qquad (2.130)$$

The system belongs to the symplectic universality class when only S constitutes a relevant symmetry [109].

This symmetry prevails even in the presence of impurities unless their potential range is smaller than the lattice constant a. In fact, for such scatterers, the effective potential is the same for the A and B sites and does not cause any mixing between the K and K' points. In this case a quantum correction or a weak-localization correction to the Boltzmann conductivity becomes positive and diverges logarithmically [29]. This so-called antilocalization behavior is the same as that appears in systems with strong spin–orbit interaction.

The operation S is not the real time reversal in graphene. Actually, the Bloch functions at the K and K' points are mutually complex conjugate, and therefore the K point is converted into the K' point and the K' point into the K point under the real time reversal. In the present $\mathbf{k} \cdot \mathbf{p}$ scheme, this operation T is expressed as

$$\mathbf{F}^T_K = e^{-i\psi}\sigma_z\mathbf{F}^*_{K'}, \quad \mathbf{F}^T_{K'} = e^{-i\psi}\sigma_z\mathbf{F}^*_K, \qquad (2.131)$$

where ψ is an arbitrary phase factor and $\mathbf{F}_K$ and $\mathbf{F}_{K'}$ are the wave functions at the K and K' points, respectively. This immediately gives

$$\mathbf{F}^{T^2}_K \equiv (\mathbf{F}^T_K)^T = \mathbf{F}_K, \quad \mathbf{F}^{T^2}_{K'} \equiv (\mathbf{F}^T_{K'})^T = \mathbf{F}_{K'}, \qquad (2.132)$$

characteristic of the conventional orthogonal symmetry. When we can neglect mixing between the K and K' points and confine

ourselves to states in each valley, however, the T symmetry is irrelevant and the special S symmetry becomes relevant. In the presence of short-range scatterers causing mixing between K and K' points, the S symmetry is violated, but the T symmetry prevails. As a result, the system now belongs to the orthogonal class [29, 110].

The actual equi-energy line deviates from the circle and has trigonal warping when the energy becomes nonzero. This effect can be included by a higher order $\mathbf{k} \cdot \mathbf{p}$ term. For the K point it is given by

$$\mathcal{H}_1 = \gamma \begin{pmatrix} 0 & h_1(\hat{k}_x, \hat{k}_y) \\ h_1(\hat{k}_x, \hat{k}_y)^\dagger & 0 \end{pmatrix}, \quad h_1(\hat{k}_x, \hat{k}_y) = \beta \frac{a}{4\sqrt{3}} (\hat{k}_x + i\hat{k}_y)^2,$$
(2.133)

where β is a constant of the order of unity. This higher order term gives rise to a trigonal warping of the dispersion. This expression with $\beta = 1$ has been derived from a nearest-neighbor tight-binding model [111] but is much more general if we regard β as an adjustable parameter. In the presence of $\mathcal{H}_1$, the special time reversal symmetry is destroyed because $\mathcal{H}_1^S = -\mathcal{H}_1$ [112]. As a result, the system now belongs to the unitary class. For the K' point, the effective Hamiltonian is obtained by the replacement of h_1 by $-h_1^\dagger$. It should be noted also that the presence of lattice strain gives rise to an effective vector potential as will be shown in the next section and therefore destroys the S symmetry. A nonzero curvature also gives rise to an effective vector potential and destroys the S symmetry [16, 113].

The time reversal symmetry is known to manifest itself as a quantum correction to the conductivity. If the system has the S symmetry, quantum correction $\Delta\sigma$ given by so-called maximally crossed diagrams exhibits an antilocalization behavior, i.e., the conductivity increases logarithmically with the decrease of the temperature. If the system has only T symmetry, $\Delta\sigma$ exhibits a weak-localization behavior and the conductivity decreases logarithmically with the temperature decrease. The crossover between the weak- and antilocalization behavior caused by short-range scatterers was demonstrated [29] and the crossover between negative and positive magnetoresistance was predicted [30]. A peculiar behavior of the magnetoresistance was experimentally observed [114–118].

2.6 Phonons and Electron–Phonon Interaction

2.6.1 *Acoustic Phonon*

Acoustic phonons important in the electron scattering are described well by a continuum model [119]. The potential-energy functional for displacement $\mathbf{u} = (u_x, u_y)$ is written as

$$U[\mathbf{u}] = \int dx dy \frac{1}{2} \Big(B(u_{xx} + u_{yy})^2 + \mu \big[(u_{xx} - u_{yy})^2 + 4u_{xy}^2 \big] \Big),$$

(2.134)

$$u_{xx} = \frac{\partial u_x}{\partial x}, \quad u_{yy} = \frac{\partial u_y}{\partial y}, \quad 2u_{xy} = \frac{\partial u_x}{\partial y} + \frac{\partial u_y}{\partial x}, \qquad (2.135)$$

as in a homogeneous and isotropic two-dimensional system. The parameters B and μ denote the bulk modulus and the shear modulus, respectively ($B = \lambda + \mu$ with λ and μ being Lame's constants). The corresponding kinetic energy is written as

$$K[\mathbf{u}] = \int dx dy \frac{\rho}{2} (\dot{u}_x^2 + \dot{u}_y^2), \qquad (2.136)$$

where ρ is the mass density given by the carbon mass per unit area, $\rho = 3.80 \times 10^{-7}$ kg/m^2.

The corresponding equations of motion are given by

$$\rho \ddot{u}_x = (B + \mu) \frac{\partial^2 u_x}{\partial x^2} + \mu \frac{\partial^2 u_x}{\partial y^2} + B \frac{\partial^2 u_y}{\partial x \partial y},$$

$$\rho \ddot{u}_y = B \frac{\partial^2 u_x}{\partial x \partial y} + (B + \mu) \frac{\partial^2 u_y}{\partial x^2} + \mu \frac{\partial^2 u_y}{\partial y^2}.$$

(2.137)

These give a transverse mode with frequency $\omega_T(q)$ and a longitudinal mode with frequency $\omega_L(q)$, where

$$\omega_T(q) = v_T q, \quad v_T = \sqrt{\frac{\mu}{\rho}},$$

$$\omega_L(q) = v_L q, \quad v_L = \sqrt{\frac{B + \mu}{\rho}},$$

(2.138)

A long-wavelength acoustic phonon gives rise to an effective potential called the deformation potential

$$V_1 = g_1(u_{xx} + u_{yy}), \qquad (2.139)$$

proportional to a local dilation, where g_1 is of the order of the Fermi level measured from the bottom of the σ bands, i.e., $g_1 \sim 30$ eV. This term appears as a diagonal term in the matrix Hamiltonian in the effective-mass approximation and cannot give rise to backscattering in metallic nanotubes. A higher order term appears due to the modification of local bond length,

$$V_2 = g_2 e^{3i\eta}(u_{xx} - u_{yy} + 2iu_{xy}), \qquad (2.140)$$

where η is the chiral angle in nanotubes and vanishes in graphene, and $g_2 \sim \gamma_0/2$ or $g_2 \sim 1.5$ eV, which is much smaller than the deformation potential constant g_1. This term appears as an off-diagonal term. The total Hamiltonian is written as

$$\mathcal{H}'_K = \begin{pmatrix} V_1 & V_2 \\ V_2^* & V_1 \end{pmatrix}, \quad \mathcal{H}'_{K'} = \begin{pmatrix} V_1 & -V_2^* \\ -V_2 & V_1 \end{pmatrix}. \qquad (2.141)$$

2.6.2 *Optical Phonon*

Long-wavelength optical phonons are known to be measured directly by the Raman scattering [120–122]. Usually, they are described perfectly well in a continuum model. Such a model was developed and the Hamiltonian for electron–phonon interactions was derived [123], and effects of electron–phonon interaction on optical phonons were recently studied in graphene [124, 125].

Optical phonons are represented by the relative displacement of two sub-lattice atoms A and B,

$$\mathbf{u}(\mathbf{r}) = \sum_{\mathbf{q},\mu} \sqrt{\frac{\hbar}{2NM\omega_0}}(b_{\mathbf{q}\mu} + b^\dagger_{-\mathbf{q}\mu})\mathbf{e}_\mu(\mathbf{q})e^{i\mathbf{q}\cdot\mathbf{r}}, \qquad (2.142)$$

where N is the number of unit cells, M is the mass of a carbon atom, ω_0 is the phonon frequency at the Γ point, $\mathbf{q} = (q_x, q_y)$ is the wave vector, μ denotes the modes ('t' for transverse and 'l' for longitudinal), and $b^\dagger_{\mathbf{q}\mu}$ and $b_{\mathbf{q}\mu}$ are the creation and destruction operators, respectively. Define $q_x = q\cos\varphi_{\mathbf{q}}$ and $q_y = q\sin\varphi_{\mathbf{q}}$ with $q = |\mathbf{q}|$. Then, we have $\mathbf{e}_l(\mathbf{q}) = i(\cos\varphi_{\mathbf{q}}, \sin\varphi_{\mathbf{q}})$ and $\mathbf{e}_t(\mathbf{q}) = i(-\sin\varphi_{\mathbf{q}}, \cos\varphi_{\mathbf{q}})$.

The interaction between optical phonons and an electron in the vicinity of the K and K′ points is given by [123]

$$\mathcal{H}^K_{\text{int}} = -\sqrt{2}\frac{\beta_\Gamma\gamma}{b^2}\vec{\sigma} \times \mathbf{u}(\mathbf{r}), \quad \mathcal{H}^{K'}_{\text{int}} = +\sqrt{2}\frac{\beta_\Gamma\gamma}{b^2}\vec{\sigma} \times \mathbf{u}(\mathbf{r}), \quad (2.143)$$

where the product for vectors $\mathbf{a} = (a_x, a_y)$ and $\mathbf{b} = (b_x, b_y)$ in two dimension is defined by $\mathbf{a} \times \mathbf{b} = a_x b_y - a_y b_x$, b is the bond length ($b = a/\sqrt{3}$), and $\beta_\Gamma = -d \ln \gamma_0/d \ln b = -(b/\gamma_0)(d\gamma_0/db)$ within a nearest-neighbor tight-binding model. Usually, we expect $\beta_\Gamma \sim 2$. This means that the lattice distortion gives rise to a shift in the origin of the wave vector or an effective vector potential, i.e., u_x in the y direction and u_y in the x direction. The interaction strength is characterized by the dimensionless coupling parameter

$$\lambda_\Gamma = \frac{36\sqrt{3}}{\pi} \frac{\hbar^2}{2Ma^2} \frac{1}{\hbar\omega_0} \left(\frac{\beta_\Gamma}{2}\right)^2. \qquad (2.144)$$

For $M = 1.993 \times 10^{-23}$ g and $\hbar\omega_0 = 0.196$ eV [126], we have $\lambda_\Gamma \approx 3 \times 10^{-3}(\beta_\Gamma/2)^2$. This shows that the interaction is not strong and therefore the lowest order perturbation gives sufficiently accurate results.

The phonon Green's function is written as

$$D_\mu(\mathbf{q}, \omega) = \frac{2\hbar\omega_0}{(\hbar\omega)^2 - (\hbar\omega_0)^2 - 2\hbar\omega_0 \Pi_\mu(\mathbf{q}, \omega)}. \qquad (2.145)$$

The phonon frequency is determined by the pole of $D_\mu(\mathbf{q}, \omega)$. In the case of weak interaction, the shift of the phonon frequency, $\Delta\omega_\mu$, and the broadening, Γ_μ, are given by

$$\Delta\omega_\mu = \frac{1}{\hbar}\mathrm{Re}\,\Pi_\mu(\mathbf{q}, \omega_0), \quad \Gamma_\mu = -\frac{1}{\hbar}\mathrm{Im}\,\Pi_\mu(\mathbf{q}, \omega_0). \qquad (2.146)$$

When we calculate the self-energy of optical phonons starting with the known phonon modes in graphene, its direct evaluation causes a problem of double counting [127]. In fact, if we apply the above formula to the case of vanishing Fermi energy, we get the frequency shift due to virtual excitations of all electrons in the π bands. However, this contribution is already included in the definition of the frequency ω_0. In order to avoid such a problem, we have to subtract the contribution in the undoped graphene for $\omega = 0$ corresponding to the adiabatic approximation.

Figure 2.19 shows the frequency shift and broadening for various values of $1/\omega_0\tau$ and an example of the spectral function,
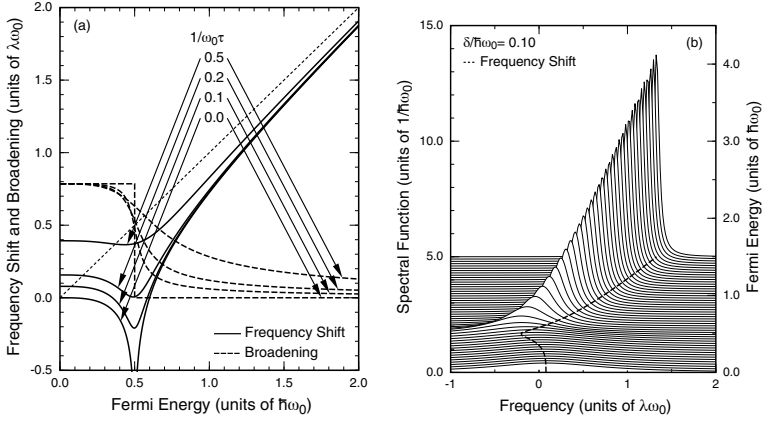
Figure 2.19 (a) The frequency shift and broadening of optical phonons in monolayer graphene as a function of the Fermi energy. τ is a phenomenological relaxation time characterizing the level broadening effect due to disorder. (b) Calculated spectral function of optical phonon for varying Fermi energy. After Ref. [124].

$(-1/\pi)\mathrm{Im}\,D(q, \omega_0)$ [124]. For nonzero δ or $1/\omega_0\tau$, the logarithmic singularity of the frequency shift and the sharp drop in the broadening disappear, but the corresponding features remain for $1/\omega_0\tau \ll 1$. Similar results were reported independently [128] and experiments giving qualitatively similar results were reported [129–131].

The calculation can easily be extended to the case in the presence of magnetic field B, where discrete Landau levels are formed and oscillations due to resonant interactions appear in the frequency shift and the broadening [125, 132]. Figure 2.20 shows calculated frequency shift and broadening when $\varepsilon_F^0/\hbar\omega_0 = 1/4$ and the corresponding phonon spectral function, where ε_F^0 is the Fermi energy in the absence of a magnetic field. All resonant transitions from $-n$ to $n+1$ and from $-n-1$ to n with $n > 0$ appear at the field where their energy difference becomes equal to $\hbar\omega_0$. At resonances, the phonon spectrum exhibits characteristic behavior. Recently this magneto-phonon resonance was observed in Raman experiments [133].
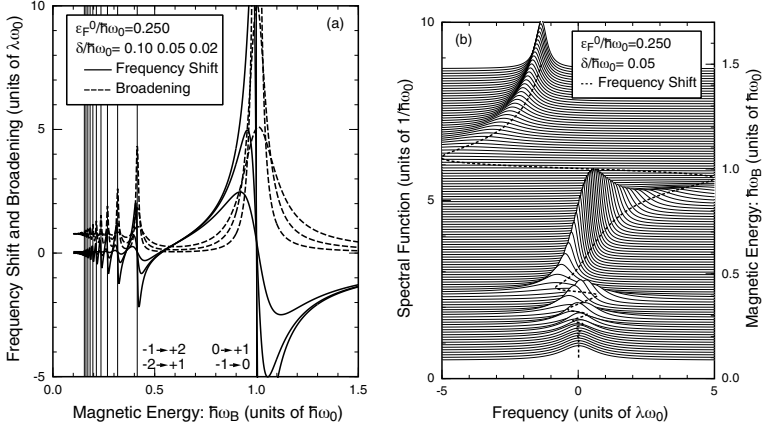
Figure 2.20 (a) The frequency shift and broadening of optical phonons in monolayer graphene as a function of effective magnetic energy $\hbar\omega_B$. Thin vertical lines show resonance magnetic fields. $\varepsilon_F^0/\hbar\omega_0 = 1/4$. The results for $\delta/\hbar\omega_0 = 0.1$, 0.05, and 0.02 are shown. (b) The phonon spectral function for $\varepsilon_F^0/\hbar\omega_0 = 1/4$ and $\delta/\hbar\omega_0 = 0.05$. The dotted line shows the peak position as a function of $\hbar\omega_B$. After Ref. [125].

2.6.3 *Zone-Boundary Phonon*

Phonons near the K and K' points, called zone-boundary phonons, can play important roles in intervalley scattering between the K and K' points. In general, there exist four independent eigen modes for each wave vector. However, after straightforward calculations, we can see that only one mode with the highest frequency contributes to the electron–phonon interaction [134]. This mode is known as a Kekulé type distortion generating only bond-length changes. The interaction Hamiltonian is given by

$$
\mathcal{H}_{\text{int}} = 2\frac{\beta_K \gamma}{b^2} \begin{pmatrix} 0 & \omega^{-1}\Delta(\mathbf{r})\sigma_y \\ \omega\Delta^\dagger(\mathbf{r})\sigma_y & 0 \end{pmatrix}, \tag{2.147}
$$

where $\omega = e^{2\pi i/3}$ and β_K is another appropriate parameter, which is equal to β_Γ for the tight-binding model. In the second quantized form,

$$
\Delta(\mathbf{r}) = \sum_{\mathbf{q}} \sqrt{\frac{\hbar}{2NM\omega_K}}(b_{K\mathbf{q}} + b_{K'-\mathbf{q}}^\dagger)e^{i\mathbf{q}\cdot\mathbf{r}}, \tag{2.148}
$$

where ω_K is the frequency of the Kekulé mode. It is worth noting that $\Delta(\mathbf{r})$ cannot be given by a simple summation over the K and K' modes. We should take a proper linear combination of the K and K' modes in order to make the lattice displacement a real variable. We can easily understand the operator form of $\Delta(\mathbf{r})$ and $\Delta(\mathbf{r})^{\dagger}$ in the interaction Hamiltonian by considering the momentum conservation with the fact that $2\mathbf{K} - \mathbf{K}'$ and $\mathbf{K} - 2\mathbf{K}'$ are reciprocal lattice vectors, where $\mathbf{K}$ and $\mathbf{K}'$ are the wave vectors at the K and K' point. The dimensionless coupling parameter, λ_K, is given by the same expression as Eq. (2.144) except that ω_0 is replaced with ω_K and β_Γ with β_K. For $\hbar\omega_K = 161.2$ meV, we have $\lambda_K = 3.5 \times 10^{-3}(\beta_K/2)^2$.

The lifetime of an electron with energy ε is given by the scattering probability from the initial state to possible final states via emission and absorption of one phonon. For the zone-center phonon, the summation of the contributions of longitudinal and transverse modes gives isotropic scattering probability in each of the K and K' points. For the zone-boundary phonon, any scattering processes are classified into two types: One is the transition between "one K-electron with one K-phonon" and "one K'-electron," and the other is between "one K-electron" and "one K'-electron with one K'-phonon." For example, an electron around the K point can be scattered to the K' point accompanied by absorption of one phonon around the K point, and this belongs to the former process. The electron scattering from the K to K' point can also be induced by the emission of one phonon around the K' point, while this is classified into the latter one.

In graphene, the calculated scattering probabilities for both phonons are given by the same formula,

$$\frac{\hbar}{\tau} = \pi\lambda_\alpha|\varepsilon - \hbar\omega_\alpha|. \tag{2.149}$$

where α represents Γ or K and we have neglected the phonon occupation due to large ω_α at room temperature. This simply shows that the electron lifetime is inversely proportional to the coupling parameter λ_α and to the density of states at the energy of the final state. What should be stressed here is that the phonon emission is possible only when the energy of the initial electron is larger than that of the phonon to be emitted. Otherwise, the

final states are fully occupied at zero temperature and the phonon emission never takes place. In this sense, the zone-boundary phonon has another advantage over the zone-center phonon. Therefore, the zone-boundary phonon gives dominant scattering for high-field transport in graphene and in nanotube owing to its smaller frequency and larger coupling constant. It also plays a dominant role in oscillatory magnetophonon resonance appearing in the conductivity in magnetic fields at high temperatures [135].

2.7 Bilayer Graphene

2.7.1 *Electronic States*

We consider a bilayer graphene that is arranged in the AB (Bernal) stacking as shown in Fig. 2.21. The upper layer is denoted as 1 and the lower layer denoted as 2. In each layer, the unit cell contains two carbon atoms denoted by A_1 and B_1 in layer 1 and A_2 and B_2 in layer 2. For the interlayer coupling, we include only the coupling between vertically neighboring atoms. Then, electronic states are described by the $\mathbf{k} \cdot \mathbf{p}$ Hamiltonian: [32, 33]

$$
\mathcal{H} =
\begin{array}{cccc}
\phantom{\begin{pmatrix}0\end{pmatrix}} A_1 & B_1 & A_2 & B_2
\end{array}
\begin{pmatrix}
0 & \gamma \hat{k}_- & 0 & 0 \\
\gamma \hat{k}_+ & 0 & \Delta & 0 \\
0 & \Delta & 0 & \gamma \hat{k}_- \\
0 & 0 & \gamma \hat{k}_+ & 0
\end{pmatrix},
\tag{2.150}
$$

where $\Delta \, (= \gamma_1 \approx 0.4$ eV) [136] represents the interlayer coupling between sites B_1 and A_2. We shall completely neglect coupling γ_3 between vertically neighboring atoms $A_1 \leftrightarrow B_2$ (see Fig. 2.21) and γ_4 giving coupling $A_1 \leftrightarrow A_2$ and $B_1 \leftrightarrow B_2$ as shown in Fig. 2.21(a). It is known that they do not play important roles [33, 125].

Let us define

$$
\varepsilon(k) = \sqrt{\left(\frac{\Delta}{2}\right)^2 + (\gamma k)^2}, \quad \gamma k = \varepsilon(k) \sin \psi, \quad \frac{\Delta}{2} = \varepsilon(k) \cos \psi,
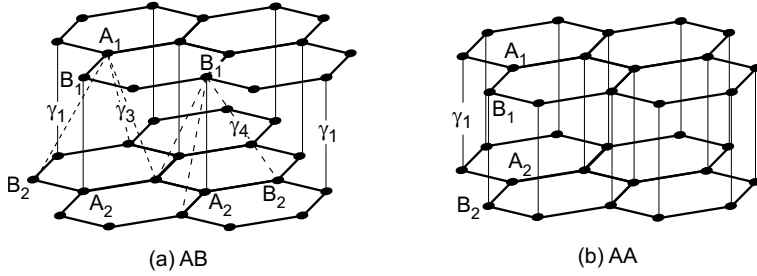\tag{2.151}
$$

Figure 2.21 The lattice structure of a bilayer graphene. Some representative hopping integrals are shown. (a) Conventional graphene with AB stacking. (b) AA stacking.

where ψ vanishes for $k = 0$ and approaches $\pi/2$ with increasing k. Then, the eigen energies are given by

$$\varepsilon_{\pm 1}(k) = \pm 2\varepsilon(k)\sin^2(\psi/2), \quad \varepsilon_{\pm 2}(k) = \pm 2\varepsilon(k)\cos^2(\psi/2).$$
(2.152)

The band $\varepsilon_{+1}(k)$ represents the lowest conduction band that touches the highest valence band $\varepsilon_{-1}(k)$ at $k = 0$. The bands $\varepsilon_{\pm 2}(k)$ are the excited conduction and valence bands and $\varepsilon_{+2}(k) - \varepsilon_{+1}(k) = \Delta$ independent of k. In the vicinity of $\varepsilon = 0$, the Hamiltonian is reduced to the (2,2) form for the basis set (A_1, B_2) [32, 33],

$$\mathcal{H} \approx \frac{\hbar^2}{2m^*} \begin{pmatrix} 0 & -\hat{k}_-^2 \\ -\hat{k}_+^2 & 0 \end{pmatrix},$$
(2.153)

with

$$m^* = \frac{\hbar^2 \Delta}{2\gamma^2}.$$
(2.154)

We have the energy dispersion $\varepsilon(k) = \pm\hbar^2 k^2/2m^*$, giving the density of states $D(\varepsilon) = g_s g_v \Delta/4\pi\gamma^2$. In the following, the energy bands are also denoted by integer $j = 1, \ldots, 4$ in the order of increasing energy as well as by ± 1 and ± 2.

One important feature is that the band structure can be strongly modified due to opening up of a bandgap by applied electric field [35, 137, 138]. Figure 2.22 shows a schematic illustration of the device structure, where eFd represents the potential difference between layers 1 and 2 (F is the effective electric field and $d = 0.334$ nm is
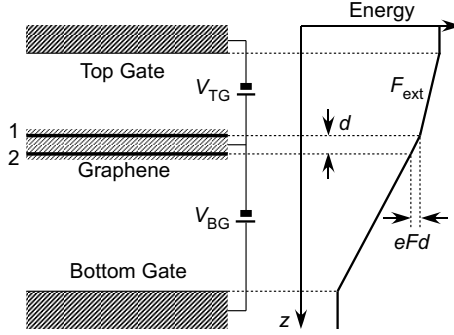
Figure 2.22   A schematic illustration of the bilayer graphene field-effect transistor with a top gate and a bottom gate and the potential energy diagram. The distance between the layers is given by d, the potential difference by eFd, and F_{ext} represents the field due to the top gate.

the interlayer distance). The effective Hamiltonian becomes

$$
\mathcal{H} = \begin{pmatrix} eFd/2 & \gamma \hat{k}_- & 0 & 0 \\ \gamma \hat{k}_+ & eFd/2 & \Delta & 0 \\ 0 & \Delta & -eFd/2 & \gamma \hat{k}_- \\ 0 & 0 & \gamma \hat{k}_+ & -eFd/2 \end{pmatrix}. \tag{2.155}
$$

In the vicinity of $\varepsilon = 0$, the Hamiltonian is reduced to the (2,2) form,

$$
\mathcal{H} \approx \begin{pmatrix} \frac{1}{2}eFd\left(1 - \frac{2}{\Delta}\frac{\hbar^2\hat{\mathbf{k}}^2}{2m^*}\right) & -\frac{\hbar^2\hat{k}_-^2}{2m^*} \\ -\frac{\hbar^2\hat{k}_+^2}{2m^*} & -\frac{1}{2}eFd\left(1 - \frac{2}{\Delta}\frac{\hbar^2\hat{\mathbf{k}}^2}{2m*}\right) \end{pmatrix}, \tag{2.156}
$$

The corresponding energy bands are

$$
\varepsilon_\pm(k) = \pm\sqrt{\frac{1}{4}(eFd)^2\left(1 - \frac{2}{\Delta}\frac{\hbar^2 k^2}{2m^*}\right)^2 + \left(\frac{\hbar^2 k^2}{2m^*}\right)^2}. \tag{2.157}
$$

In the region of small k satisfying $\hbar^2 k^2/2m^* \ll \Delta$, we have

$$
\varepsilon_\pm(k) \approx \pm\frac{1}{2}eFd\left(1 - \frac{2}{\Delta}\frac{\hbar^2 k^2}{2m^*}\right), \tag{2.158}
$$

showing that the lowest conduction band has its minima away from $k = 0$ [35]. Figure 2.23 shows the energy bands obtained by the diagonalization of this Hamiltonian. The bandgap appears and the minimum gap is located at a nonzero value of k depending on the field.
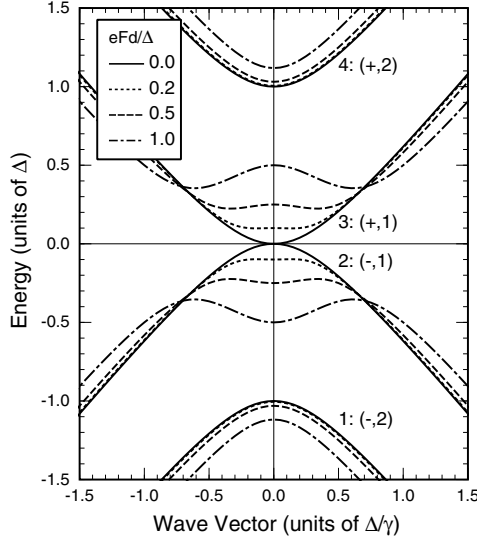
Figure 2.23 The energy dispersion for varying values of the potential difference eFd. The dot-dot-dashed lines show that of a monolayer graphene. After Ref. [138].

The effective field is determined in a self-consistent manner because the electron density distribution between two layers becomes different, giving rise to interlayer potential difference. Some examples of the results of such calculations are shown in Fig. 2.24 [138]. The unit $n_s^0 = g_v g_s \Delta^2 / 2\pi\gamma^2$ is the electron concentration at $\varepsilon_F = \Delta$ for $eFd = 0$. We have $n_s^0 \approx 2.5 \times 10^{13}$ cm^{-2} for $\Delta \approx 0.4$ eV. We can see eFd can become as large as $\sim \Delta/2$ although being dependent on $eF_{ext}d$, which represents the field due to an extra gate as shown in Fig. 2.22.

The structure of an AA stacked bilayer graphene is shown in Fig. 2.21(b). When we consider the strongest nearest-neighbor interlayer interaction, the Hamiltonian becomes

$$\hat{\mathcal{H}}_0 = \begin{array}{cccc} A_1 & B_1 & A_2 & B_2 \end{array} \\ \begin{pmatrix} +eFd/2 & \gamma\hat{k}_- & \Delta & 0 \\ \gamma\hat{k}_+ & +eFd/2 & 0 & \Delta \\ \Delta & 0 & -eFd/2 & \gamma\hat{k}_- \\ 0 & \Delta & \gamma\hat{k}_+ & -eFd/2 \end{pmatrix}. \quad (2.159)$$
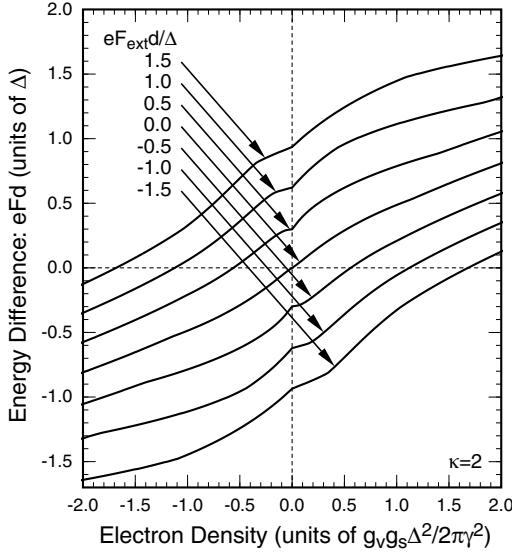
Figure 2.24 Calculated energy difference eFd as a function of the electron concentration for various values of $eF_{ext}d$. The static dielectric constant of the environment is chosen as $\kappa = 2$. After Ref. [138].

Let us define

$$\Delta = \tilde{\Delta}\sin\psi, \quad \frac{eFd}{2} = \tilde{\Delta}\cos\psi, \quad \tilde{\Delta} = \sqrt{\Delta^2 + \left(\frac{eFd}{2}\right)^2}, \quad (2.160)$$

and

$$V = \begin{pmatrix} \cos(\psi/2) & 0 & -\sin(\psi/2) & 0 \\ 0 & \cos(\psi/2) & 0 & -\sin(\psi/2) \\ \sin(\psi/2) & 0 & +\cos(\psi/2) & 0 \\ 0 & \sin(\psi/2) & 0 & +\cos(\psi/2) \end{pmatrix}. \quad (2.161)$$

Then, we have

$$V^{-1}\hat{\mathcal{H}}_0 V = \begin{pmatrix} \tilde{\Delta} & \gamma\hat{k}_- & 0 & 0 \\ \gamma\hat{k}_+ & \tilde{\Delta} & 0 & 0 \\ 0 & 0 & -\tilde{\Delta} & \gamma\hat{k}_- \\ 0 & 0 & \gamma\hat{k}_+ & -\tilde{\Delta} \end{pmatrix}. \quad (2.162)$$

This immediately shows that the band structure consists of two monolayer-like bands relatively shifted in energy by amount $\pm\tilde{\Delta}$. The presence of potential asymmetry between the top and bottom

layers does not cause significant change except for the increase in the relative shift of two monolayer bands.

2.7.2 Magnetic Properties

Let us consider first the symmetric bilayer graphene with AB stacking. The Landau level in the region $|\varepsilon| \ll \Delta$ in magnetic field B perpendicular to graphene can be calculated from the Hamiltonian (2.153) as [32]

$$\varepsilon_{sn} = s\hbar\omega_c\sqrt{n(n+1)}, \quad (n = 0, 1, \cdots, \ s = \pm 1) \qquad (2.163)$$

where $\omega_c = eB/m^*c$. We have doubly degenerate levels at zero energy ($n = 0$ and $s = \pm 1$), while the spacing gradually becomes constant as n goes higher. This degeneracy of the zero-energy Landau level also leads to logarithmic singularity of the magnetic susceptibility. In fact, in a manner similar to but more complicated than in the monolayer graphene, the susceptibility is calculated as

$$\chi = -\left(\frac{e\hbar}{2m^*}\right)^2 \frac{g_s g_v m^*}{2\pi\hbar^2} \int_{-\varepsilon_c}^{\varepsilon_c} \left(\ln\frac{\varepsilon_c}{|\varepsilon|} - 1\right)\left(-\frac{\partial f}{\partial\varepsilon}\right)d\varepsilon, \qquad (2.164)$$

where ε_c is a cutoff energy of the order of Δ.

In order to show this logarithmic dependence intuitively, we expand the Landau level energy for large n as

$$\varepsilon_{sn} = s\hbar\omega_c\left[\left(n + \frac{1}{2}\right) - \frac{1}{8}\left(n + \frac{1}{2}\right)^{-1} + \cdots\right], \qquad (2.165)$$

where the first term gives the constant interval, and the second gives a shift toward zero energy, which is rewritten as $-(\hbar\omega_c)^2/(8\varepsilon_{sn})$. For $\varepsilon_F < 0$, for example, the change in the total energy due to the energy shift is calculated as

$$\Delta E = -\frac{g_s g_v m^*}{2\pi\hbar^2}\int_{-\varepsilon_c}^{\varepsilon_F}\frac{(\hbar\omega_c)^2}{8\varepsilon}d\varepsilon = \frac{B^2}{2}\frac{g_v g_s}{4\pi}\frac{e^2\gamma^2}{\hbar^2\Delta}\ln\frac{\varepsilon_c}{|\varepsilon_F|}, \qquad (2.166)$$

giving the $\ln|\varepsilon_F|$ dependence of the susceptibility.

An analytic expression for the susceptibility for the full Hamiltonian (2.155) can be derived but will not be presented here because it is too complicated [22]. Figure 2.25 shows the density of states and the susceptibility for $eFd/\Delta = 0$, 0.2, and 0.5. In the absence of gap, the susceptibility exhibits logarithmic divergence at zero energy. In the presence of a nonzero gap, this singularity is removed, but
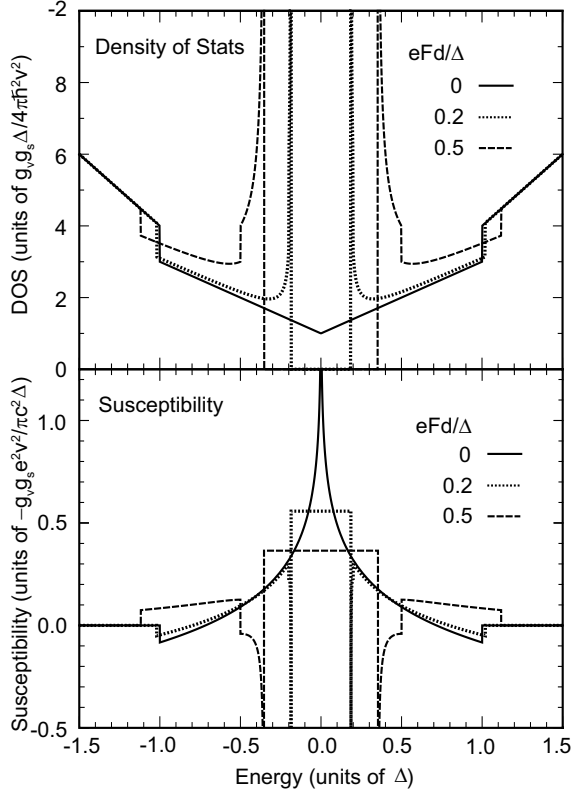
Figure 2.25 The density of states (upper panel) and susceptibility (lower panel) of bilayer graphenes with the asymmetry gap $eFd/\Delta = 0$, 0.2, and 0.5. The upward direction represents negative (i.e., diamagnetic) susceptibility. After Ref. [22].

the susceptibility is constant within the gap region together with singular paramagnetic susceptibility at the band edges.

2.7.3 *Optical Properties*

In bilayer graphene, optical absorption is possible in two different configurations, electric field of light parallel and perpendicular to the layer. It is straightforward to calculate the dynamical conductivity describing optical absorption for electric field parallel

to the layer [139, 140]. It is obtained by replacing σ_x with Σ_x in Eq. (2.86), where

$$\Sigma_x = \begin{pmatrix} 0 & 1 & 0 & 0 \\ 1 & 0 & 0 & 0 \\ 0 & 0 & 0 & 1 \\ 0 & 0 & 1 & 0 \end{pmatrix}. \tag{2.167}$$

The effective conductivity for perpendicular electric field is calculated as follows [140]: We apply external electric field $E_{ext}(\omega)e^{-i\omega t} + \text{c.c.}$ perpendicular to the layer, where 'c.c.' stands for complex conjugate. Let n_1 and n_2 be the electron density in layers 1 and 2, respectively, per unit area. The asymmetry in the density distribution $\Delta n(\omega)$ is defined as $\Delta n(\omega) = n_2(\omega) - n_1(\omega)$. This induces electric field

$$(-e)E_{ind}(\omega) = -\frac{4\pi e^2}{\kappa}\frac{\Delta n(\omega)}{2}, \tag{2.168}$$

in the region $-d/2 < z < +d/2$, where κ is the static dielectric constant of the environment.

We shall define the polarizability $\alpha(\omega)$ through

$$(-e)\frac{\Delta n(\omega)}{2} = \alpha(\omega)E_{tot}(\omega), \tag{2.169}$$

where $E_{tot}(\omega)e^{-i\omega t} + \text{c.c.}$ is the total electric field. Then, we have

$$(-e)E_{tot}(\omega) = (-e)E_{ext}(\omega) - \frac{4\pi e^2}{\kappa}\frac{\Delta n(\omega)}{2}, \tag{2.170}$$

giving

$$E_{tot}(\omega) = \frac{E_{ext}(\omega)}{\varepsilon(\omega)}, \tag{2.171}$$

$$\varepsilon(\omega) = 1 + \frac{4\pi}{\kappa}\alpha(\omega). \tag{2.172}$$

With the use of the equation of continuity, we have induced current

$$j(\omega) = -i\omega(-e)\frac{\Delta n(\omega)}{2} = \frac{1}{d}\sigma_{zz}(\omega)E_{tot}(\omega), \tag{2.173}$$

in the region $-d/2 < z < +d/2$, with two-dimensional conductivity

$$\sigma_{zz}(\omega) = -i\omega\alpha(\omega)d. \tag{2.174}$$

Then, we have

$$\varepsilon(\omega) = 1 + \frac{4\pi i}{\omega \kappa d} \sigma_{zz}(\omega), \qquad (2.175)$$

$$j(\omega) = \frac{1}{d} \tilde{\sigma}_{zz}(\omega) E_{\text{ext}}(\omega), \qquad (2.176)$$

with

$$\tilde{\sigma}_{zz}(\omega) = \frac{\sigma_{zz}(\omega)}{\varepsilon(\omega)}. \qquad (2.177)$$

The power absorption per unit area is given by

$$P = \frac{d}{2} \text{Re} \left[j(\omega) E_{\text{tot}}(\omega)^* \right] = \frac{1}{2} \text{Re} \, \tilde{\sigma}_{zz}(\omega) |E_{\text{ext}}(\omega)|^2. \qquad (2.178)$$

The dynamical conductivity can easily be calculated in a linear response theory. Define

$$\hat{\tau} = \begin{pmatrix} +1 & 0 & 0 & 0 \\ 0 & +1 & 0 & 0 \\ 0 & 0 & -1 & 0 \\ 0 & 0 & 0 & -1 \end{pmatrix}. \qquad (2.179)$$

Then, we have

$$\sigma_{zz}(\omega) = i\omega e^2 d^2 \frac{g_s g_v}{4} \frac{1}{L^2} \sum_{\alpha,\beta} \frac{(f_\alpha - f_\beta)|\hat{\tau}_{\alpha\beta}|^2}{\varepsilon_\alpha - \varepsilon_\beta + \hbar\omega + i\delta}, \qquad (2.180)$$

where α and β stand for a set of quantum numbers $(j, \mathbf{k})$ and $f_\alpha = f(\varepsilon_\alpha)$ is the Fermi distribution function. We have used the fact that both K and K' points give the same contribution. Explicitly, we have

$$\sigma_{zz}(\omega) = i\omega e^2 d^2 \frac{g_s g_v}{4} \frac{1}{2\pi\gamma^2} \sum_{j,j'} \int_0^\infty \gamma^2 k dk \, g(\gamma k)$$

$$\times \frac{[f(\varepsilon_{jk}) - f(\varepsilon_{j'k})]|\hat{\tau}_{jj'}(k)|^2}{\varepsilon_{jk} - \varepsilon_{j'k} + \hbar\omega + i\delta}. \qquad (2.181)$$

In the above, we have introduced cutoff function $g(\varepsilon)$ decaying rapidly for energy comparable to the half of the π-band width. The typical magnitude of the conductivity becomes

$$\sigma_1 = \frac{e^2}{\hbar} \frac{g_s g_v}{4} \frac{d^2}{2\pi\gamma^2} \Delta^2 \sim \frac{e^2}{\pi\hbar} \frac{g_s g_v}{4} \times 0.022, \qquad (2.182)$$

where we have used $a = 2.46$ Å, $d = 3.34$ Å, $\Delta \approx 0.4$ eV, and $\gamma_0 \approx 3$ eV in the last expression.
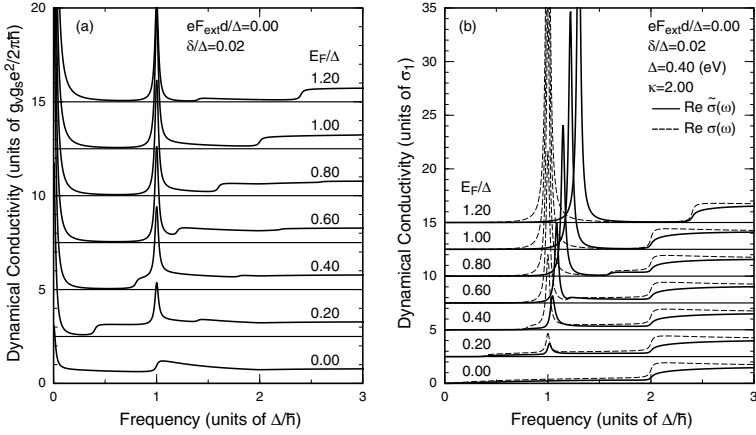
Figure 2.26 Calculated dynamical conductivity for (a) parallel and (b) perpendicular polarization in a symmetric bilayer graphene. The dashed lines in (a) represent $\sigma_{zz}(\omega)$ without depolarization effect and the solid lines $\tilde{\sigma}_{xx}(\omega)$ with depolarization effect. After Ref. [140].

Figure 2.26 shows some examples of calculated dynamical conductivity for (a) parallel and (b) perpendicular polarization in a symmetric case $eFd = 0$, with several values of the Fermi energy. The dashed lines in (b) represent $\sigma_{zz}(\omega)$ without depolarization effect and the solid lines $\tilde{\sigma}_{zz}(\omega)$ with depolarization effect. The dynamical conductivity for $\varepsilon_F = 0$ has essentially no prominent structure except a step-like increase corresponding to transitions from $(-, 1)$ to $(+, 2)$ [139]. In a symmetric bilayer, with increase in ε_F, a delta-function peak appears at $\hbar\omega = \Delta$ with intensity proportional to $|\varepsilon_F|$, corresponding to allowed transitions $(+, 1) \rightarrow (+, 2)$. For perpendicular polarization, this sharp peak is shifted to the higher energy side due to the depolarization effect. When the Fermi level reaches the bottom of band $(+, 2)$, this shift is as large as 30 %.

Figure 2.27 shows the dynamical conductivity for varying electron concentration n_s for $F_{ext} = 0$, i.e., when the bilayer is symmetric for $n_s = 0$ and the asymmetry potential eFd increases with the change of n_s. The energies where interband transitions start to appear are shown by thin dotted lines. For transitions from $(+, 1)$ to $(+, 2)$, i.e., $3 \rightarrow 4$, the upper edge
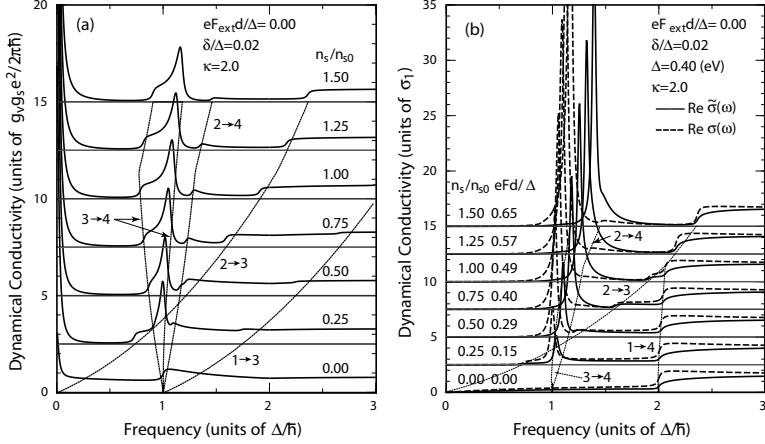
Figure 2.27 Calculated dynamical conductivity for parallel (a) and perpendicular (b) polarization for $eF_{ext}d = 0$. The potential difference between two layers, eFd/Δ, self-consistently determined is listed in the figure. Thin dotted lines denote edges of interband transitions ($j \rightarrow j'$ means those from band j to band j'). After Ref. [140].

where the transition disappears is also included. For the parallel polarization, the absorption corresponding to transitions $(+, 1) \rightarrow (+, 2)$ becomes broadened with increase of n_s due to the gap opening. For the perpendicular polarization, this broadening is not significant, because the resonance occurs at an energy higher than the interband continuum due to the depolarization effect. A weak structure appears near the line denoted as $2 \rightarrow 4$ with the increase of n_s. This corresponds to the transition from $(-, 1)$ to $(+, 2)$, which becomes allowed by the bandgap opening.

The strength of the absorption for the perpendicular polarization is determined by conductivity $\tilde{\sigma}_{zz}(\omega)$ of the order of σ_1, while that for the parallel polarization by $\sigma_{xx}(\omega)$ of the order of $(g_v g_s e^2)/(4\pi\hbar)$. Because $\sigma_1 \sim 0.022 \times (g_v g_s e^2)/(4\pi\hbar)$, the absorption intensity for perpendicular polarization is much smaller. This smallness of $\tilde{\sigma}_{zz}(\omega)$ mainly comes from the fact that interlayer coupling γ_1 (~ 0.4 eV) is much smaller than intra-layer coupling γ_0 (~ 3 eV) in spite of the fact that interlayer separation d (= 3.34 Å) is not so much different from the intralayer lattice constant a (= 2.46 Å). The weak
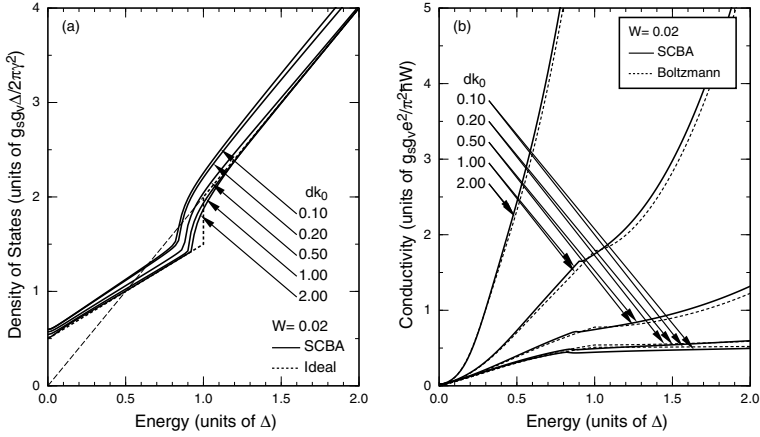
Figure 2.28 (a) Calculated density of states and (b) conductivity as a function of energy for scatterers with Gaussian potential with range d in units of $k_0 = \Delta/\gamma$ and dimensionless scattering strength $W = 0.02$. The dotted line in (a) represents the density of states of ideal bilayer graphene and the thin dashed line represents that of two independent monolayer graphenes. The dotted line in (b) shows the Boltzmann conductivity. After Ref. [141].

absorption intensity requires the use of bilayer graphene with large area.

2.7.4 *Transport Properties*

It is easy to theoretically formulate transport theory in bilayer graphene within the Boltzmann scheme. In the following, however, we shall exclusively discuss results obtained in the self-consistent Born approximation [141]. Figure 2.28 shows calculated (a) density of states and (b) conductivity as a function of energy for scatterers with a Gaussian potential with range d and for scattering strength $W = 0.1$. In Fig. 2.28(a) the dotted line represents the ideal density of states and the dashed line represents twice of that in monolayer graphene and in 2.28(b) the dotted lines represent the Boltzmann conductivity.

The density of states clearly shows that the energy region affected strongly by the presence of scatterers is limited to $|\varepsilon| \lesssim \gamma/d$

for small d such that $dk_0 \leq 0.2$, where $k_0 = \Delta/\gamma$. When the range becomes larger such that $dk_0 \geq 2$, the region affected by scatterers is separated into two, those close to zero energy and close to the bottom of the excited conduction band Δ. In fact, the excited conduction band has significant band tail due to disorder.

At zero energy, the Boltzmann conductivity vanishes due to the vanishing velocity. In the self-consistent Born approximation, the conductivity becomes close to the universal value obtained previously for short-range scatterers [33, 39]

$$\sigma_2 = \frac{g_s g_v e^2}{\pi^2 \hbar}, \tag{2.183}$$

which is twice as large as that in monolayer graphene [23], the universality of which remains as a hot topic [74–81]. It increases rapidly with energy, becoming larger than the Boltzmann conductivity at sufficiently high energy for long-range scatterers $dk_0 > 0.5$.

The conductivity exhibits a kink-like structure when the energy crosses the bottom of the excited conduction band. This behavior also seen in the Boltzmann conductivity arises due to sudden appearance of interband scattering, which is more dominant than the appearance of extra conductivity due to additional carriers in the excited conduction band. Apart from the difference in the kink position, the overall behavior of the conductivity is very close to that of the Boltzmann result. Interband matrix elements between the state $\mathbf{k} = 0$ at the bottom of the excited conduction band and those of the lowest conduction band vanish, and therefore the conductivity does not exhibit stronger step-like decrease at the band-crossing point.

Figure 2.29 shows the minimum conductivity at zero energy. For very short-range case $dk_0 < 1$, the conductivity is nearly independent of W and close to σ_2. With the increase in the range, the conductivity increases with W, takes a maximum at a certain value of W and then starts to decrease. The value of W where the minimum conductivity becomes maximum increases with the range. This figure clearly shows that the conductivity at zero energy is not universal but depends on the degree of the disorder for scatterers with long-range potential. This situation is the same as in monolayer graphene [68].
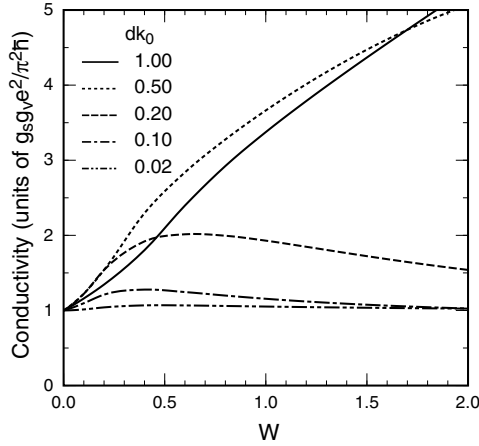
Figure 2.29 Calculated minimum conductivity at zero energy versus W for scatterers with Gaussian potential. After Ref. [141].

Calculations can also be performed for charged impurities within the Thomas–Fermi approximation for screening [141]. Figure 2.30 shows some examples of calculated (a) density of states and (b) conductivity. The density of states in the low-energy region becomes larger with the concentration of scatterers. Further, the excited conduction band has a long tail in the density of states, its amount being roughly proportional to the concentration.

The minimum conductivity at zero energy becomes slightly larger than the universal value given by Eq. (2.183) and increases with the impurity concentration. However, it approximately remains universal because the dependence on n_i is weak as shown in the inset of Fig. 2.30(b). When the energy exceeds the bottom of the excited conduction band, the Boltzmann conductivity exhibits a discrete jump. This jump is also present in the conductivity in the self-consistent Born approximation, although it is considerably smoothed out. This increase when the excited band is occupied comes from the sudden increase in the screening effect.

Figure 2.31 shows some examples for an asymmetric bilayer with nonzero gap. The density of states does not easily vanish and has low energy tail. This is partly due to the self-consistency between the screening constant and the density of states. In fact, smaller density
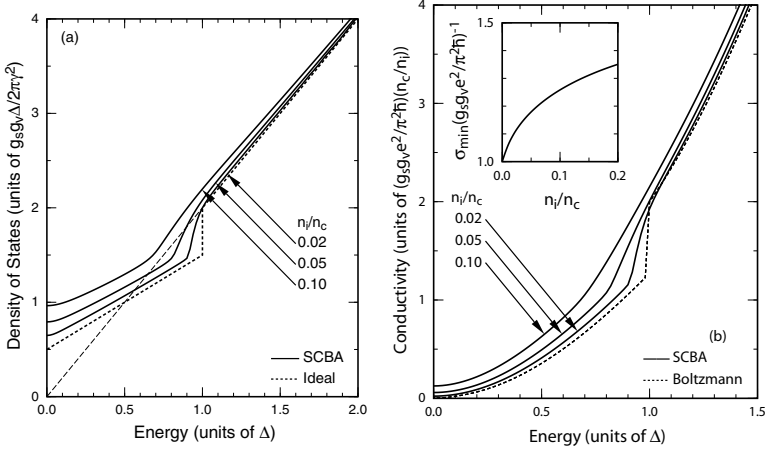
Figure 2.30 Density of states (a) and conductivity (b) versus the Fermi energy for charged scatterers screened in the Thomas–Fermi approximation, calculated in a self-consistent Born approximation. The inset in (b) shows the minimum conductivity versus the impurity concentration. After Ref. [141].

of states causes less screening and causes effectively large scattering strength giving rise to long tail in the density of states. In spite of the considerable density of states, the conductivity within the gap region is much smaller than that outside, in particular for large gap $eFd/\Delta = 1$.

Calculations can also be performed for bilayer graphene with AA stacking. Figure 2.32 shows some examples of calculated (a) density of states and (b) conductivity as a function of energy for symmetric bilayer $eFd = 0$ with AA stacking. Results for asymmetric bilayer can be obtained by replacing Δ with $\tilde{\Delta}$ given in Eq. (2.160). The density of states in the clean limit is independent of energy in the region given by $-\Delta < \varepsilon < +\Delta$ and starts to increase linearly outside this region, as shown by a dotted line in Fig. 2.32(a). In the presence of charged impurities, the density of states is enhanced symmetrically around $\pm\Delta$ corresponding to the Dirac points of the two bands given by Eq. (2.162). As a result, the total density of states is most strongly enhanced near zero energy.
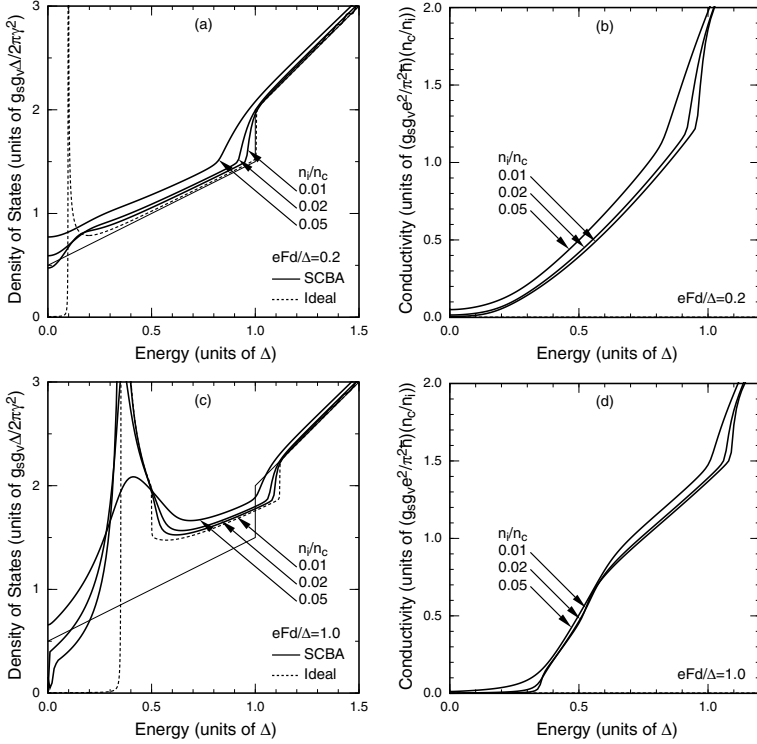
Figure 2.31 Calculated density of states (a) and (c), and conductivity (b) and (d) of asymmetric bilayer graphene. (a) and (b) $eFd/\Delta = 0.2$. (c) and (d) $eFd/\Delta = 1$. After Ref. [82].

For small impurity concentration $n_i/n_c = 0.05$, the conductivity exhibits a singularly sharp drop at $\pm\Delta$. This is a manifestation of the zero-mode anomaly appearing in the conductivity for short-range scatterers with strength independent of energy or electron concentration predicted previously [23], shown in Fig. 2.10. In fact, the screening effect is essentially independent of the energy in the vicinity of $\pm\Delta$ as shown in Fig. 2.32(a), making charged impurities effectively "short-range scatterers" with energy independent strength. Therefore, the zero-mode anomalies characteristic of massless Dirac electrons can be experimentally observed in an AA stacked bilayer graphene even if scattering is dominated by charged
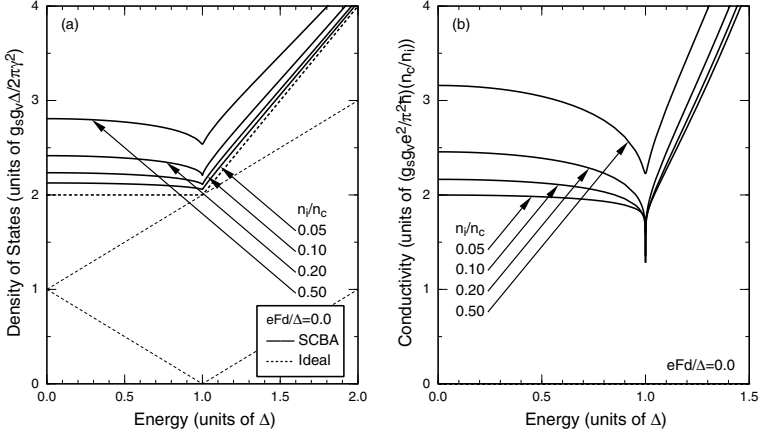
Figure 2.32 Calculated density of states (a) and conductivity (b) of AA-stacked bilayer graphene for charged impurities with screening effect being included within the Thomas–Fermi approximation. After Ref. [82].

impurities. In monolayer graphenes, this singularity is obscured by diverging scattering strength at the Dirac point.

2.7.5 *Phonons and Electron–Phonon Interaction*

When we neglect small interlayer coupling and interaction with electrons in the vicinity of the Fermi level, acoustic phonons in each layer are regarded as independent and the same as those in monolayer graphene. As a result, the interaction Hamiltonian in each layer is the same as in monolayer. The same is applicable to optical phonons and zone boundary phonons. Within such an approximation scheme, it is straightforward to make theoretical formulation on electron–phonon interactions. In the following, we shall consider interaction effects on optical phonons as an example.

In symmetric bilayer graphene, optical phonons are classified into symmetric and antisymmetric modes in which the displacement of the top and bottom layers are in-phase and out-of-phase, respectively. They are affected by electron–phonon interactions in a different manner [142]. The symmetric mode causes interband transitions between $\varepsilon_{\pm 1}(k)$ and therefore exhibits logarithmic singularity in a manner same as in monolayer graphene when $\varepsilon_F =$
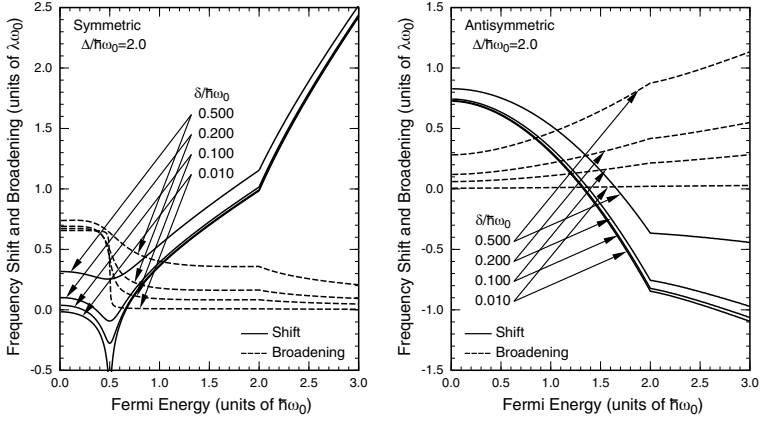
Figure 2.33 Some examples of calculated frequency shift and broadening of the symmetric (a) and antisymmetric mode (b) at the Γ point in a bilayer graphene. $\Delta/\hbar\omega_0 = 2$. The amount of the broadening due to disorder is denoted by δ. After Ref. [142].

$\hbar\omega_0/2$. On the other hand, this transition is not allowed for the antisymmetric mode, but interband transitions between $\varepsilon_{+1}(k)$ and $\varepsilon_{+2}(k)$ contribute to the phonon renormalization when band $\varepsilon_{+1}(k)$ is occupied by electrons.

Figure 2.33 shows calculated frequency shift and broadening for two phonon modes. For the symmetric mode, the shift increases almost linearly in the range $1/2 < \varepsilon_F/\hbar\omega_0 < 2$. Above $\varepsilon_F = \Delta$, corresponding to $\varepsilon_F/\hbar\omega_0 = 2$ for $\Delta/\hbar\omega_0 = 2$, the second conduction band is populated by electrons and the dependence on ε_F becomes steeper. For the antisymmetric mode, the frequency is enhanced from ω_0 of the mono-layer graphene at $\varepsilon_F = 0$ and the broadening is absent, because the contribution of interband transitions between the bands $\varepsilon_{\pm1}(k)$ is suppressed. With the increase of ε_F interband transitions between $\varepsilon_{+1}(k)$ and $\varepsilon_{+2}(k)$ contribute to the self-energy and the frequency gradually decreases.

When the electron concentration is changed by a gate voltage, potential asymmetry is introduced, and as a result, the symmetric and antisymmetric modes are mixed with each other through electron–phonon interactions [138]. Figure 2.34 shows the frequency shift (top panel), broadening (middle panel), and the spectral intensity
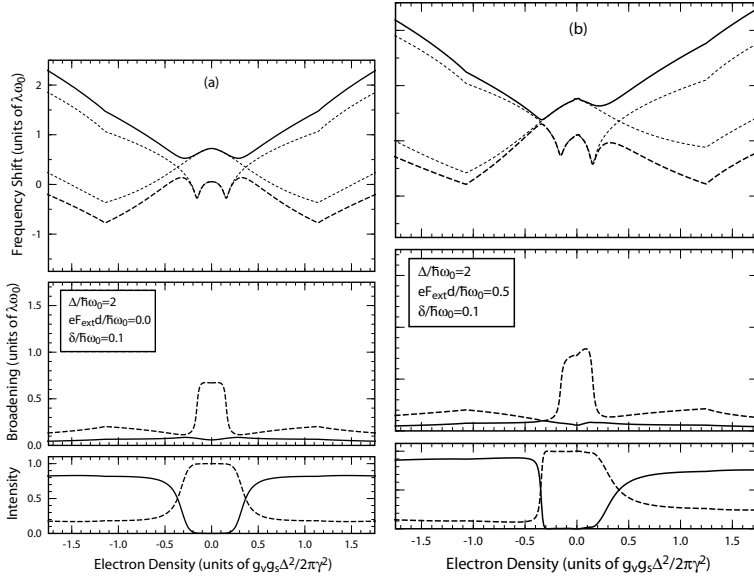
Figure 2.34 Calculated frequency shift, broadening, and strength of the symmetric component. The solid and dashed lines denote the high- and low-frequency modes, respectively. The thin dotted lines in the top panel show the frequencies for symmetric and antisymmetric modes calculated without inclusion of their mixing. $\Delta/\hbar\omega_0 = 2$. $\delta/\hbar\omega_0 = 0.1$. (a) $eF_{\text{ext}}d/\Delta = 0$ and (b) 0.5. After Ref. [138].

(bottom panel) of the symmetric component as a function of the electron concentration for $eF_{\text{ext}}d = 0$. We have assumed $\Delta/\hbar\omega_0 = 2$ corresponding to $\Delta \approx 0.4$ eV and $\hbar\omega_0 \approx 0.2$ eV and $\delta/\hbar\omega_0 = 0.1$. The symmetric component shown in the figure describes the relative intensity of the Raman scattering. At $n_s = 0$ with $eFd = 0$, the optical phonons are exactly classified into symmetric and antisymmetric modes. With the increase of n_s, they become mixed with each other, which becomes particularly important when they cross each other.

In the presence of nonzero external field as $eF_{\text{ext}}d/\hbar\omega_0 = 0.5$ as shown in Fig. 2.34(b), the results are asymmetric between positive and negative n_s. In fact, the intensity of the low-frequency mode is much stronger for $n_s > 0$ than for $n_s < 0$. The appearance of two peaks at sufficiently high electron concentration is in agreement

with that of recent experiments showing double peaks in a highly doped bilayer graphene [143–148]. In order to make detailed comparison with experiments, we may have to consider a small frequency splitting of symmetric and antisymmetric modes that is independent of the change in the electron concentration.

2.8 Multilayer Graphene

We consider a multilayer graphene composed of N graphene layers arranged in the AB (Bernal) stacking. For simplicity we include the nearest-neighbor intra-layer coupling parameter γ_0 and the interlayer coupling $\Delta = \gamma_1$ between A and B atoms located vertically with respect to the layer plane. We can show that the Hamiltonian of a multilayer graphene can be decomposed into those equivalent to monolayer or bilayer, which allows us to systematically study the dependence of various quantities on layer numbers [40–42]. This exact decomposition rule is not destroyed by the presence of next-nearest-neighbor interlayer coupling γ_3 causing trigonal warping of the bands.

Let $|A_j\rangle$ and $|B_j\rangle$ be the Bloch functions at the K point, corresponding to the A and B sublattices, respectively, of layer j. For convenience we divide carbon atoms into two groups as

$$
\begin{aligned}
&\text{Group I}: \ B_1, \ A_2, \ B_3, \ \cdots \\
&\text{Group II}: \ A_1, \ B_2, \ A_3, \ \cdots
\end{aligned}
\tag{2.184}
$$

The atoms of group I are arranged along vertical columns normal to the layer plane, while those in group II are above or below the center of hexagons in the neighboring layers. If the basis is taken as $|A_1\rangle, |B_1\rangle; |A_2\rangle, |B_2\rangle; \cdots; |A_N\rangle, |B_N\rangle$, the Hamiltonian for the multilayer graphene around the K point becomes

$$
\mathcal{H} = \begin{pmatrix} H_0 & V & & \\ V^\dagger & H_0 & V^\dagger & \\ & V & H_0 & V \\ & & \ddots & \ddots & \ddots \end{pmatrix},
\tag{2.185}
$$

with

$$
H_0 = \begin{pmatrix} 0 & \gamma \hat{k}_- \\ \gamma \hat{k}_+ & 0 \end{pmatrix}, \quad V = \begin{pmatrix} 0 & 0 \\ \Delta & 0 \end{pmatrix}.
\tag{2.186}
$$

The effective Hamiltonian for K' is obtained by exchanging $\hat{k}_+$ and $\hat{k}_-$.

The Hamiltonian (2.185) can be decomposed into smaller subsystems for the basis appropriately chosen [40, 41]. First, we define the orthonormal sets

$$
\begin{aligned}
\phi_l^{(\mathrm{I})} &= \psi_l^{(1)}|B_1\rangle + \psi_l^{(2)}|A_2\rangle + \psi_l^{(3)}|B_3\rangle + \cdots, \\
\phi_l^{(\mathrm{II})} &= \psi_l^{(1)}|A_1\rangle + \psi_l^{(2)}|B_2\rangle + \psi_l^{(3)}|A_3\rangle + \cdots,
\end{aligned}
\tag{2.187}
$$

where

$$
\begin{aligned}
\psi_l^{(j)} &= \sqrt{\frac{2}{N+1}}\sin j\kappa_l, \quad \kappa_l = \frac{\pi}{2} - \frac{l\pi}{2(N+1)}, \\
l &= -(N-1), -(N-3), \ldots, N-1.
\end{aligned}
\tag{2.188}
$$

Here, l is an odd integer when N is even, while l is even when N is odd, and therefore $l = 0$ is allowed only for odd N.

Next, for $m > 0$, we take the basis

$$
\begin{aligned}
\Big\{ (\phi_m^{(\mathrm{II})} + \phi_{-m}^{(\mathrm{II})})/\sqrt{2}, \quad (\phi_m^{(\mathrm{I})} + \phi_{-m}^{(\mathrm{I})})/\sqrt{2}, \\
(\phi_m^{(\mathrm{I})} - \phi_{-m}^{(\mathrm{I})})/\sqrt{2}, \quad (\phi_m^{(\mathrm{II})} - \phi_{-m}^{(\mathrm{II})})/\sqrt{2} \Big\}.
\end{aligned}
\tag{2.189}
$$

For $m = 0$, we take the basis $\{\phi_0^{(\mathrm{II})}, \phi_0^{(\mathrm{I})}\}$. Then, the Hamiltonian has no off-diagonal elements between different m's. For $m > 0$, the sub-Hamiltonian becomes

$$
\mathcal{H}_m = \begin{pmatrix}
0 & \gamma\hat{k}_- & 0 & 0 \\
\gamma\hat{k}_+ & 0 & \lambda_m\Delta & 0 \\
0 & \lambda_m\Delta & 0 & \gamma\hat{k}_- \\
0 & 0 & \gamma\hat{k}_+ & 0
\end{pmatrix},
\tag{2.190}
$$

with

$$
\lambda_m = 2\cos\kappa_m,
\tag{2.191}
$$

which is equivalent to the Hamiltonian of bilayer graphene, while the interlayer coupling Δ is multiplied by λ_m. For $m = 0$, we have the Hamiltonian identical to that of the monolayer graphene. These subsystems are labeled as $m = 0, 2, 4, \cdots, N-1$ for odd N and $m = 1, 3, 5, \cdots, N-1$ for even N.

The eigenstate of a finite-layer graphene can be regarded as a part of a standing wave in bulk graphite, which is a superposition
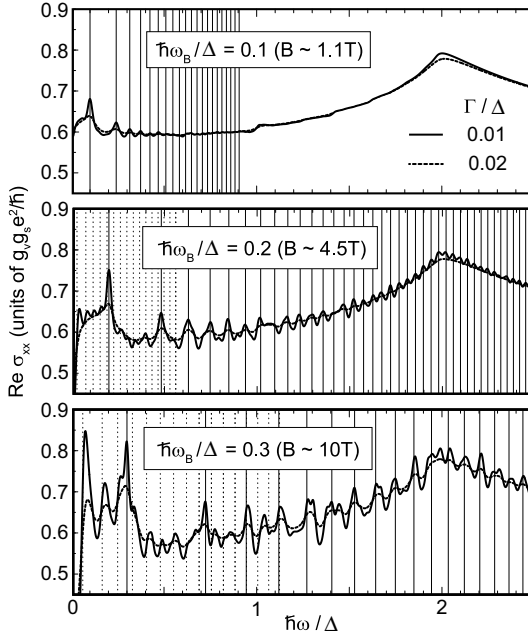
Figure 2.35 Examples of the real part of the dynamical conductivity averaged over the layer numbers from $N = 1$ to 20, for magnetic fields with $\hbar\omega_B/\Delta = 0.1$, 0.2 and 0.3. Vertical solid and dashed lines represent transition energies for monolayer-type ($\kappa = \pi/2$) and bilayer-type ($\kappa = 0$) subbands, respectively. After Ref. [41].

of opposite traveling waves with $\pm k_z$. The quantity κ ($= \kappa_m$) in our representation corresponds to a wave number via $\kappa = |k_z|d$, where d is the interlayer distance. Thus the monolayer-type subband $\kappa = \pi/2$ is related to an H point in the Brillouin zone of graphite, while no states correspond to $k_z = 0$ since κ never becomes zero.

Thus, the Hamiltonian has been decomposed into those equivalent to the monolayer or bilayer bands. The monolayer-like band exists only in odd-layered graphenes, while the bilayer-like bands always exist. This decomposition can be used for the analysis of diamagnetic response of multilayer graphenes [40]. In fact, in odd-layered graphenes, the monolayer-like band gives a strong diamagnetic peak at $\varepsilon_F = 0$, while the bilayer-like bands
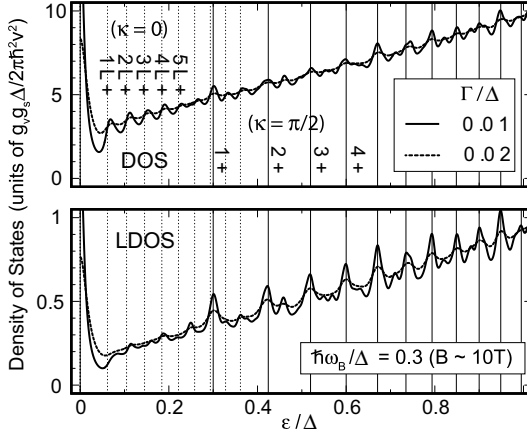
Figure 2.36 (Top) Density of states averaged over the layer numbers $N = 1$ to 20, at $\hbar\omega_B/\Delta = 0.3$. (Bottom) Corresponding plot for the local density of states on the top layer. Vertical solid and dashed lines indicate the ideal Landau level energies for the monolayer-type ($\kappa = \pi/2$) and the bilayer-type ($\kappa = 0$) subbands, respectively. After Ref. [41].

present a broad peak. With the increase of the layer number, the susceptibility is dominated by that of bilayer-like bands. Thus, the large diamagnetic susceptibility of bulk graphite can be understood in terms of the logarithmic singularity of bilayer graphene.

This decomposition rule can also be used for the dynamical conductivity describing optical absorption and the local density of states observed by scanning tunneling spectroscopy [41]. Figure 2.35 shows the dynamical conductivity averaged over the samples $N = 1, 2, \cdots, 20$. Surprisingly, we still see the series of peaks in the monolayer graphene $\hbar\omega \propto \sqrt{B}$. This comes from the monolayer-type subbands that appears in every odd layered graphene.

In Fig. 2.36, the top panel shows the total density of states and the bottom panel shows the corresponding plot for the local density of states on the top layer. In the total density of states, we observe the several peaks coming from the monolayer-type subband similarly to the optical absorption spectra. In the local density of states, interestingly, the peaks of the monolayer-type subband are much more pronounced.

References

1. K. S. Novoselov, A. K. Geim, S. V. Morozov, D. Jiang, Y. Zhang, S. V. Dubonos, I. V. Grigorieva, and A. A. Firsov, Electric field effect in atomically thin carbon films, *Science* **306**, 666 (2004).

2. C. Berger, Z. Song, T. Li, X. Li, A. Y. Ogbazghi, R. Feng, Z. Dai, A. N. Marchenkov, E. H. Conrad, P. N. First, and W. A. de Heer, Ultrathin epitaxial graphite: 2D electron gas properties and a route toward graphene-based nanoelectronics., *J. Phys. Chem. B* **108**, 19912 (2004).

3. K. S. Kim, Y. Zhao, H. Jang, S. Y. Lee, J. M. Kim, K. S. Kim, J. -H. Ahn, P. Kim, J.-Y. Choi, and B. H. Hong, Large-scale pattern growth of graphene films for stretchable transparent electrodes, *Nature* **457**, 706 (2009).

4. K. S. Novoselov, A. K. Geim, S. V. Morozov, D. Jiang, M. I. Katsnelson, I. V. Grigorieva, S. V. Dubonos, and A. A. Firsov, Two-dimensional gas of massless Dirac fermions in graphene, *Nature* **438**, 197 (2005).

5. Y. Zhang, Y.-W. Tan, H. L. Stormer, and P. Kim, Experimental observation of the quantum Hall effect and Berry's phase in graphene, *Nature* **438**, 201 (2005).

6. T. Ando, Exotic electronic and transport properties of graphene, *Physica E* **40**, 213 (2007).

7. T. Ando, The electronic properties of graphene and carbon nanotubes, *NPG Asia Mater.* **1**, 17 (2009).

8. A. H. Castro Neto, F. Guinea, N. M. Peres, K. S. Novoselov, and A. K. Geim, The electronic properties of graphene, *Rev. Mod. Phys.* **81**, 109 (2009).

9. D. S. L. Abergel, V. Apalkov, J. Berashevich, K. Ziegler, and T. Chakraborty, Properties of graphene: A theoretical perspective, *Adv. Phys.* **59**, 261 (2010).

10. T. Ando, Theory of electronic states and transport in carbon nanotubes, *J. Phys. Soc. Jpn.* **74**, 777 (2005).

11. J. W. McClure, Diamagnetism of graphite, *Phys. Rev.* **104**, 666 (1956).

12. J. C. Slonczewski and P. R. Weiss, Band structure of graphite, *Phys. Rev.* **109**, 272 (1958).

13. D. P. DiVincenzo and E. J. Mele, Self-consistent effective-mass theory for intralayer screening in graphite intercalation compounds, *Phys. Rev. B* **29**, 1685 (1984).

14. G. W. Semenoff, Condensed-matter simulation of a three-dimensional anomaly, *Phys. Rev. Lett.* **53**, 2449 (1984).

15. H. Ajiki and T. Ando, Electronic states of carbon nanotubes, *J. Phys. Soc. Jpn.* **62**, 1255 (1993).

16. C. L. Kane and E. J. Mele, Size, shape, and low energy electronic structure of carbon nanotubes, *Phys. Rev. Lett.* **78**, 1932 (1997).

17. T. Ando and T. Nakanishi, Impurity scattering in carbon nanotubes — absence of back scattering, *J. Phys. Soc. Jpn.* **67**, 1704 (1998).

18. T. Ando, T. Nakanishi, and R. Saito, Berry's phase and absence of back scattering in carbon nanotubes, *J. Phys. Soc. Jpn.* **67**, 2857 (1998).

19. M. Koshino and T. Ando, Diamagnetism in disordered graphene, *Phys. Rev. B* **75**, 235333 (2007).

20. H. Fukuyama, Anomalous orbital magnetism and Hall effect of massless fermions in two dimension, *J. Phys. Soc. Jpn.* **76**, 043711 (2007).

21. M. Koshino, Y. Arimura, and T. Ando, Magnetic field screening and mirroring in graphene, *Phys. Rev. Lett.* **102**, 177203 (2009).

22. M. Koshino and T. Ando, Anomalous orbital magnetism in Dirac-electron systems: Role of pseudo-spin paramagnetism, *Phys. Rev. B* **81**, 195431 (2010).

23. N. H. Shon and T. Ando, Quantum transport in two-dimensional graphite system, *J. Phys. Soc. Jpn.* **67**, 2421 (1998).

24. Y. Zheng and T. Ando, Hall conductivity of two-dimensional graphite system, *Phys. Rev. B* **65**, 245420 (2002).

25. T. Ando, Y. Zheng, and H. Suzuura, Dynamical conductivity and zero-mode anomaly in honeycomb lattices, *J. Phys. Soc. Jpn.* **71**, 1318 (2002).

26. T. Ando and H. Suzuura, Presence of perfectly conducting channel in metallic carbon nanotubes, *J. Phys. Soc. Jpn.* **71**, 2753 (2002).

27. T. Ando, Aharonov–Bohm effect and symmetry crossover in carbon nanotubes, *J. Phys. Soc. Jpn.* **75**, 054701 (2006).

28. T. Ando, Effects of symmetry crossover in quantum transport in graphene and nanotube, *Phil. Trans. Roy. Soc. A* **366**, 221 (2008).

29. H. Suzuura and T. Ando, Crossover from symplectic to orthogonal class in a two-dimensional honeycomb lattice, *Phys. Rev. Lett.* **89**, 266603 (2002).

30. E. McCann, K. Kechedzhi, V. I. Falko, H. Suzuura, T. Ando, and B. L. Altshuler, Weak localisation magnetoresistance in graphene, *Phys. Rev. Lett.* **97**, 146805 (2006).

31. See, for example, A. Kobayashi, S. Katayama, Y. Suzumura, and H. Fukuyama, Massless fermions in organic conductor, *J. Phys. Soc. Jpn.* **76**, 034711 (2007).

32. E. McCann and V. I. Falko, Landau-level degeneracy and quantum Hall effect in a graphite bilayer, *Phys. Rev. Lett.* **96**, 086805 (2006).

33. M. Koshino and T. Ando, Transport in bilayer graphene: Calculation within a self-consistent Born approximation, *Phys. Rev. B* **73**, 245403 (2006).

34. M. I. Katsnelson, Minimal conductivity in bilayer graphene, *Euro. Phys. J. B* **52**, 151 (2006).

35. E. McCann, Asymmetry gap in the electronic band structure of bilayer graphene, *Phys. Rev. B* **74**, 161403 (2006).

36. J. Nilsson, A. H. Castro Neto, N. M. R. Peres, and F. Guinea, Electron–electron interactions and the phase diagram of a graphene bilayer, *Phys. Rev. B* **73**, 214418 (2006).

37. F. Guinea, A. H. Castro Neto, and N. M. R. Peres, Electronic states and Landau levels in graphene stacks, *Phys. Rev. B* **73**, 245426 (2006).

38. E. V. Castro, K. S. Novoselov, S. V. Morozov, N. M. R. Peres, J. M. B. Lopes dos Santos, J. Nilsson, F. Guinea, A. K. Geim, and A. H. Castro Neto, Biased bilayer graphene: Semiconductor with a gap tunable by the electric field effect, *Phys. Rev. Lett.* **99**, 216802 (2007).

39. M. Koshino, Electronic transport in bilayer graphene, *New J. Phys.* **11**, 095010 (2009).

40. M. Koshino and T. Ando, Orbital diamagnetism in multilayer graphenes: Systematic study with the effective mass approximation, *Phys. Rev. B* **76**, 085425 (2007).

41. M. Koshino and T. Ando, Magneto-optical properties of multilayer graphenes, *Phys. Rev. B* **77**, 115313 (2008).

42. M. Koshino and T. Ando, Electronic structures and optical absorption of multilayer graphenes, *Solid State Commun.* **149**, 1123 (2009).

43. M. V. Berry, Quantum phase factors accompanying adiabatic changes, *Proc. Roy. Soc. London* **A392**, 45 (1984).

44. B. Simon, Holonomy, the quantum adiabatic theorem, and Berry's phase, *Phys. Rev. Lett.* **51**, 2167 (1983).

45. T. Ando, Screening effect and impurity scattering in monolayer graphene, *J. Phys. Soc. Jpn.* **75**, 074716 (2006).

46. S. Y. Zhou, G.-H. Gweon, A. V. Fedorov, P. N. First, W. A. de Heer, D.-H. Lee, F. Guinea, A. H. Castro Neto, and A. Lanzara, Substrate-induced bandgap opening in epitaxial graphene, *Nat. Mat.* **6**, 770 (2007).

47. S. Y. Zhou, D. A. Siegel, A. V. Fedorov, F. E. Gabaly, A. K. Schmid, A. H. Castro Neto, D.-H. Lee, and A. Lanzara, Origin of the energy bandgap in epitaxial graphene, *Nat. Mat.* **7**, 259 (2008).

48. A. W. W. Ludwig, M. P. A. Fisher, R. Shankar, and G. Grinstein, Integer quantum Hall transition: An alternative approach and exact results, *Phys. Rev. B* **50**, 7526 (1994).

49. J. W. McClure, Theory of diamagnetism of graphite, *Phys. Rev.* **119**, 606 (1960).

50. M. P. Sharma, L. G. Johnson, and J. W. McClure, Diamagnetism of graphite, *Phys. Rev. B* **9**, 2467 (1974).

51. S. A. Safran and F. J. DiSalvo, Theory of magnetic susceptibility of graphite intercalation compounds, *Phys. Rev. B* **20**, 4889 (1979).

52. J. Blinowski and C. Rigaux, Theory of magnetic susceptibility in acceptor and donor graphite intercalation compounds, *J. Phys. (Paris)* **45**, 545 (1984).

53. R. Saito and H. Kamimura, Orbital susceptibility of higher-stage graphite intercalation compounds, *Phys. Rev. B* **33**, 7218 (1986).

54. M.-C. Chang and Q. Niu, Berry phase, hyperorbits, and the Hofstadter spectrum: Semiclassical dynamics in magnetic Bloch bands, *Phys. Rev. B* **53**, 7010 (1996).

55. D. Xiao, W. Yao, and Q. Niu, Valley-contrasting physics in graphene: Magnetic moment and topological transport, *Phys. Rev. Lett.* **99**, 236809 (2007).

56. H. Ajiki and T. Ando, Magnetic properties of carbon nanotubes, *J. Phys. Soc. Jpn.* **62**, 2470 (1993).

57. M. Yamamoto, M. Koshino, and T. Ando, Electric and magnetic response of multi-wall carbon nanotubes, *J. Phys. Soc. Jpn.* **77**, 084705 (2008).

58. T. Ando, Theory of cyclotron resonance line shape in a two-dimensional electron system., *J. Phys. Soc. Jpn.* **38**, 989 (1975).

59. R. R. Nair, P. Blake, A. N. Grigorenko, K. S. Novoselov, T. J. Booth, T. Stauber, N. M. R. Peres, and A. K. Geim, Fine structure constant defines visual transparency of graphene, *Science* **320**, 1308 (2008).

60. Z. Q. Li, E. A. Henriksen, Z. Jiang, Z. Hao, M. C. Martin, P. Kim, H. L. Stormer, and D. N. Basov, Dirac charge dynamics in graphene by infrared spectroscopy, *Nat. Phys.* **4**, 532 (2008).

61. T. Ando, Effects of valley mixing and exchange on excitons in carbon nanotubes with Aharonov–Bohm flux, *J. Phys. Soc. Jpn.* **75**, 024707 (2006).

62. T. Ando, A. B. Fowler, and F. Stern, Electronic properties of two-dimensional systems, *Rev. Mod. Phys.* **54**, 437 (1982).

63. E. A. Taft and H. R. Philipp, Optical properties of graphite, *Phys. Rev.* **138**, A197 (1965).

64. K. Nomura and A. H. MacDonald, Quantum Hall ferromagnetism in graphene, *Phys. Rev. Lett.* **96**, 256602 (2006).

65. T. Fukuzawa, M. Koshino, and T. Ando, Weak-field Hall effect in graphene calculated within self-consistent Born approximation, *J. Phys. Soc. Jpn.* **78**, 094714 (2009).

66. T. Ando and Y. Uemura, Theory of quantum transport in a two-dimensional electron system under magnetic fields. I. Characteristics of level broadening and transport under strong fields, *J. Phys. Soc. Jpn.* **36**, 959 (1974).

67. J. Martin, N. Akerman, G. Ulbricht, T. Lohmann, J. H. Smet, K. von Klitzing, and A. Yacoby, Observation of electron-hole puddles in graphene using a scanning single-electron transistor, *Nat. Phys.* **4**, 144 (2008).

68. M. Noro, M. Koshino, and T. Ando, Theory of transport in graphene with long-range scatterers, *J. Phys. Soc. Jpn.* **79**, 094713 (2010).

69. E. Fradkin, Critical behavior of disordered degenerate semiconductors. II. Spectrum and transport properties in mean-field theory, *Phys. Rev. B* **33**, 3263 (1986).

70. P. A. Lee, Localized states in a d-wave superconductor, *Phys. Rev. Lett.* **71**, 1887 (1993).

71. A. K. Geim and K. S. Novoselov, The rise of graphene, *Nat. Mater.* **6**, 183 (2007).

72. Y.-W. Tan, Y. Zhang, K. Bolotin, Y. Zhao, S. Adam, E. H. Hwang, S. Das Sarma, H. L. Stormer, and P. Kim, Measurement of scattering rate and minimum conductivity in graphene, *Phys. Rev. Lett.* **99**, 246803 (2007).

73. K. I. Bolotin, K. J. Sikes, Z. Jiang, G. Fundenberg, J. Hone, P. Kim, and H. L. Stormer, Ultrahigh electron mobility in suspended graphene, *Solid State Commun.* **146**, 351 (2008).

74. H. Kumazaki and D. S. Hirashima, Effects of impurities in two-dimensional graphite, *J. Phys. Soc. Jpn.* **75**, 053707 (2006).

75. I. L. Aleiner and K. B. Efetov, Effect of disorder on transport in graphene, *Phys. Rev. Lett.* **97**, 236801 (2006).

76. K. Ziegler, Robust transport properties in graphene, *Phys. Rev. Lett.* **97**, 266802 (2006).

77. K. Nomura and A. H. MacDonald, Quantum transport of massless Dirac fermions, *Phys. Rev. Lett.* **98**, 076602 (2007).

78. J. H. Bardarson, J. Tworzydo, P. W. Brouwer, and C. W. J. Beenakker, One-parameter scaling at the Dirac point in graphene, *Phys. Rev. Lett.* **99**, 106801 (2007).

79. S. Adam, E. H. Hwang, V. M. Galitski, and S. Das Sarma, A self-consistent theory for graphene transport, *Proc. Nat. Acad. Sci.* **104**, 18392 (2007).

80. K. Ziegler, Long-range correlations in disordered graphene, *Phys. Rev. B* **78**, 125401 (2008).

81. S. Adam, P. W. Brouwer, and S. Das Sarma, Crossover from quantum to Boltzmann transport in graphene, *Phys. Rev. B* **79**, 201404 (2009).

82. T. Ando, Charged impurity scattering in graphenes: Effects of environmental screening, band gap, and AA stacking, *J. Phys.: Conf. Ser.* **302**, 012015 (2011).

83. W. W. Toy, M. S. Dresselhaus, and G. Dresselhaus, Minority carriers in graphite and the H-point magnetoreflection spectra, *Phys. Rev. B* **15**, 4077 (1977).

84. M. Monteverde, C. Ojeda-Aristizabal, R. Weil, K. Bennaceur, M. Ferrier, S. Gueron, C. Glattli, H. Bouchiat, J. N. Fuchs, and D. L. Maslov, Transport and elastic scattering times as probes of the nature of impurity scattering in single-layer and bilayer graphene, *Phys. Rev. Lett.* **104**, 126801 (2010).

85. C. Jang, S. Adam, J.-H. Chen, E. D. Williams, S. Das Sarma, and M. S. Fuhrer, Tuning the effective fine structure constant in graphene: Opposing effects of dielectric screening on short- and long-range potential scattering, *Phys. Rev. Lett.* **101**, 146805 (2008).

86. L. A. Ponomarenko, R. Yang, T. M. Mohiuddin, M. I. Katsnelson, K. S. Novoselov, S. V. Morozov, A. A. Zhukov, F. Schedin, E. W. Hill, and A. K. Geim, Effect of a high-κ environment on charge carrier mobility in graphene, *Phys. Rev. Lett.* **102**, 206603 (2009).

87. F. Chen, J. Xia, D. K. Ferry, and N. Tao, Dielectric screening enhanced performance in graphene FET, *Nano Lett.* **9**, 2574 (2009).

88. A. Hashimoto, K. Suenaga, A. Gloter, K. Urita, and S. Iijima, Direct evidence for atomic defects in graphene layers, *Nature* **430**, 870 (2004).

89. J. H. Warner, M. H. Rummeli, L. Ge, T. Gemming, B. Montanari, N. M. Harrison, B. Buchner, and G. A. D. Briggs, Structural transformations in graphene studied with high spatial and temporal resolution, *Nat. Nano.* **4**, 500 (2009).

90. S. Y. Zhou, D. A. Siegel, A. V. Fedorov, and A. Lanzara1, Metal to insulator transition in epitaxial graphene induced by molecular doping, *Phys. Rev. Lett.* **101**, 086402 (2008).

91. F. Schedin, A. K. Geim, S. V. Morozov, E. W. Hill, P. Blake, M. I. Katsnelson, K. S. Novoselov, Detection of individual gas molecules adsorbed on graphene, *Nat. Mat.* **6**, 652 (2007).

92. See, for example, C. Coletti, C. Riedl, D. S. Lee, B. Krauss, L. Patthey, K. von Klitzing, J. H. Smet, and U. Starke, Charge neutrality and band-gap tuning of epitaxial graphene on SiC by molecular doping, *Phys. Rev. B* **81**, 235401 (2010).

93. T. Ando, T. Nakanishi, and M. Igami, Effective-mass theory of carbon nanotubes with a vacancy, *J. Phys. Soc. Jpn.* **68**, 3994 (1999).

94. M. Igami, T. Nakanishi, and T. Ando, Conductance of carbon nanotube with a vacancy, *J. Phys. Soc. Jpn.* **68**, 716 (1999).

95. M. Igami, T. Nakanishi, and T. Ando, Numerical study of transport in carbon nanotubes with lattice vacancy, *J. Phys. Soc. Jpn.* **68**, 3146 (1999).

96. M. Igami, T. Nakanishi, and T. Ando, Effect of lattice vacancy on conductance of carbon nanotubes, *Physica B* **284–288**, 1746 (2000).

97. M. Igami, T. Nakanishi, and T. Ando, Effect of lattice vacancy on carbon nanotubes: Conductance quantization, *Mol. Cryst. Liq. Cryst.* **340**, 719 (2000).

98. M. Igami, T. Nakanishi, and T. Ando, Effective-mass theory of carbon nanotubes with vacancies in magnetic fields., *J. Phys. Soc. Jpn.* **70**, 481 (2001).

99. O. Zhou, R. M. Fleming, D. W. Murphy, R. C. Haddon, A. P. Ramirez, and S. H. Glarum, Carbon nanotube with defects, *Science* **263**, 1744 (1994).

100. M. Bockrath, W. J. Liang, D. Bozovic, J. H. Hafner, C. M. Lieber, M. Tinkham, and H. K. Park, Resonant electron scattering by defects in single-walled carbon nanotubes, *Science* **291**, 283 (2001).

101. J. W. Park, J. Kim, J.-O. Lee, K. C. Kang, J.-J. Kim, and K.-H. Yoo, Effects of artificial defects on the electrical transport of single-walled carbon nanotubes, *Appl. Phys. Lett.* **80**, 133 (2002).

102. J.-C. Charlier, T. W. Ebbesen, and Ph. Lambin, Structural and electronic properties of pentagon–heptagon pair defects in carbon nanotubes, *Phys. Rev. B* **53**, 11108 (1996).

103. L. Chico, L. X. Benedict, S. G. Louie, and M. L. Cohen, Quantum conductance of carbon nanotubes with defects, *Phys. Rev. B* **54**, 2600 (1996).

104. H. J. Choi, J.-S. Ihm, S. G. Louie, and M. L. Cohen, Defects, quasibound states, and quantum conductance in metallic carbon nanotubes, *Phys. Rev. Lett.* **84**, 2917 (2000).

105. B. C. Pan, W. S. Yang, and Jinlong Yang, Formation energies of topological defects in carbon nanotubes, *Phys. Rev. B* **62**, 12652 (2000).

106. T. Kostyrko, M. Bartkowiak, and G. D. Mahan, Reflection by defects in a tight-binding model of nanotubes, *Phys. Rev. B* **59**, 3241 (1999).

107. H. Matsumura and T. Ando, Conductance of carbon nanotube with a Stone–Wales defect, *J. Phys. Soc. Jpn.* **70**, 2657 (2001).

108. A. Toyoda and T. Ando, Theory of electron scattering by lattice defects in monolayer graphene, *J. Phys. Soc. Jpn.* **79**, 094708 (2010).

109. F. J. Dyson, Statistical theory of the energy levels of complex systems. I, *J. Math. Phys.* **3**, 140 (1962).

110. T. Ando and K. Akimoto, Effects of short-range scatterers on perfect channel in metallic carbon nanotubes, *J. Phys. Soc. Jpn.* **73**, 1895 (2004).

111. H. Ajiki and T. Ando, Energy bands of carbon nanotubes in magnetic fields, *J. Phys. Soc. Jpn.* **65**, 505 (1996).

112. K. Akimoto and T. Ando, Effects of trigonal warping on perfect channel in metallic carbon nanotubes, *J. Phys. Soc. Jpn.* **73**, 2194 (2004).

113. T. Ando, Spin–orbit interaction in carbon nanotubes, *J. Phys. Soc. Jpn.* **69**, 1757 (2000).

114. S. V. Morozov, K. S. Novoselov, M. I. Katsnelson, F. Schedin, L. A. Ponomarenko, D. Jiang, and A. K. Geim, Strong suppression of weak localization in graphene, *Phys. Rev. Lett.* **97**, 016801 (2006).

115. X.-S. Wu, X.-B. Li, Z.-M. Song, C. Berger, and W. A. de Heer, Weak antilocalization in epitaxial graphene: Evidence for chiral electrons, *Phys. Rev. Lett.* **98**, 136801 (2007).

116. F. V. Tikhonenko, D. W. Horsell, R. V. Gorbachev, and A. K. Savchenko, Weak localization in graphene flakes, *Phys. Rev. Lett.* **100**, 056802 (2008).

117. D.-K. Ki, D.-C. Jeong, J.-H. Choi, H.-J. Lee, and K.-S. Park, Inelastic scattering in a monolayer graphene sheet: A weak-localization study, *Phys. Rev. B* **78**, 125409 (2008).

118. F. V. Tikhonenko, A. A. Kozikov, A. K. Savchenko, and R. V. Gorbachev, Transition between electron localization and antilocalization in graphene, *Phys. Rev. Lett.* **103**, 226801 (2009).

119. H. Suzuura and T. Ando, Phonons and electron–phonon scattering in carbon nanotubes, *Phys. Rev. B* **65**, 235412 (2002).

120. A. C. Ferrari, J. C. Meyer, V. Scardaci, C. Casiraghi, M. Lazzeri, F. Mauri, S. Piscanec, D. Jiang, K. S. Novoselov, S. Roth, and A. K. Geim, Raman spectrum of graphene and graphene layers, *Phys. Rev. Lett.* **97**, 187401 (2006).

121. A. Gupta, G. Chen, P. Joshi, S. Tadigadapa, and P.C. Eklund, Raman scattering from high-frequency phonons in supported n-graphene layer films, *Nano Lett.* **6**, 2667 (2006).

122. C. N. R. Rao, A. K. Sood, K. S. Subrahmanyam, and A. Govindaraj, Graphene: The new two-dimensional nanomaterial, *Angew. Chem.* **48**, 7752 (2009).

123. K. Ishikawa and T. Ando, Optical phonon interacting with electrons in carbon nanotubes, *J. Phys. Soc. Jpn.* **75**, 084713 (2006).

124. T. Ando, Anomaly of optical phonon in monolayer graphene, *J. Phys. Soc. Jpn.* **75**, 124701 (2006).

125. T. Ando, Magnetic oscillation of optical phonon in graphene, *J. Phys. Soc. Jpn.* **76**, 024712 (2007).

126. J. Maultzsch, S. Reich, C. Thomsen, H. Requardt, and P. Ordejon, Phonon dispersion in graphite, *Phys. Rev. Lett.* **92**, 075501 (2004).

127. N. A. Viet, H. Ajiki, and T. Ando, Lattice instability in metallic carbon nanotubes, *J. Phys. Soc. Jpn.* **63**, 3036 (1994).

128. M. Lazzeri and F. Mauri, Nonadiabatic Kohn anomaly in a doped graphene monolayer, *Phys. Rev. Lett.* **97**, 266407 (2006).

129. S. Pisana, M. Lazzeri, C. Casiraghi, K. S. Novoselov, A. K. Geim, A. C. Ferrari, and F. Mauri, Breakdown of the adiabatic Born–Oppenheimer approximation in graphene, *Nat. Mat.* **6**, 198 (2007).

130. J. Yan, Y. Zhang, P. Kim, and A. Pinczuk, Electric field effect tuning of electron–phonon coupling in graphene, *Phys. Rev. Lett.* **98**, 166802 (2007).

131. A. Das, S. Pisana, B. Chakraborty, S. Piscanec, S. K. Saha, U. V. Waghmare, K. S. Novoselov, H. R. Krishnamurthy, A. K. Geim, A. C. Ferrari, and A. K. Sood, Monitoring dopants by Raman scattering in an electrochemically top-gated graphene transistor, *Nat. Nanotech.* **3**, 210 (2008).

132. M. O. Goerbig, J.-N. Fuchs, K. Kechedzhi, and V. I. Falko, Filling-factor-dependent magnetophonon resonance in graphene, *Phys. Rev. Lett.* **99**, 087402 (2007).

133. C. Faugeras, M. Amado, P. Kossacki, M. Orlita, M. Sprinkle, C. Berger, W. A. de Heer, and M. Potemski, Tuning the electron–phonon coupling in multilayer graphene with magnetic fields, *Phys. Rev. Lett.* **103**, 186803 (2009).

134. H. Suzuura and T. Ando, Zone-boundary phonon in graphene and nanotube, *J. Phys. Soc. Jpn.* **77**, 044703 (2008).

135. N. Mori and T. Ando, Magnetophonon resonance in monolayer graphene, *J. Phys. Soc. Jpn.* **80**, 044706 (2011).

136. A. Misu, E. Mendez, and M. S. Dresselhaus, Near infrared reflectivity of graphite under hydrostatic pressure. I. experiment, *J. Phys. Soc. Jpn.* **47**, 199 (1979).

137. H. Min, B. Sahu, S. K. Banerjee, and A. H. MacDonald, *Ab initio* theory of gate induced gaps in graphene bilayers, *Phys. Rev. B* **75**, 155115 (2007).

138. T. Ando and M. Koshino, Field effects on optical phonons in bilayer graphene, *J. Phys. Soc. Jpn.* **78**, 034709 (2009).

139. D. S. L. Abergel and V. I. Falko, Optical and magneto-optical far-infrared properties of bilayer graphene, *Phys. Rev. B* **75**, 155430 (2007).

140. T. Ando and M. Koshino, Optical absorption by interlayer density excitations in bilayer graphene, *J. Phys. Soc. Jpn.* **78**, 104716 (2009).

141. T. Ando, Bilayer graphene with long-range scatterers studied in a self-consistent Born approximation, *J. Phys. Soc. Jpn.* **80**, 014707 (2011).

142. T. Ando, Anomaly of optical phonons in bilayer graphene, *J. Phys. Soc. Jpn.* **76**, 104711 (2007).

143. L. M. Malard, D. C. Elias, E. S. Alves, and M. A. Pimenta, Observation of distinct electron–phonon couplings in gated bilayer graphene, *Phys. Rev. Lett.* **101**, 257401 (2008).

144. J. Yan, T. Villarson, E. A. Henriksen, P. Kim, and A. Pinczuk, Optical phonon mixing in bilayer graphene with a broken inversion symmetry, *Phys. Rev. B* **80**, 241417 (2009).

145. M. Bruna and S. Borini, Observation of Raman G-band splitting in top-doped few-layer graphene, *Phys. Rev. B* **81**, 125421 (2010).

146. J. M. Garcia, R. He, M. P. Jiang, J. Yan, A. Pinczuk, Y. M. Zuev, K. S. Kim, P. Kim, K. Baldwin, K. W. West, and L. N. Pfeiffer, Multilayer graphene films grown by molecular beam deposition, *Solid State Commun.* **150**, 809 (2010).

147. A. B. Kuzmenko, L. Benfatto, E. Cappelluti, I. Crassee, D. van der Marel, P. Blake, K. S. Novoselov, and A. K. Geim, Gate tunable infrared phonon anomalies in bilayer graphene, *Phys. Rev. Lett.* **103**, 116804 (2009).

148. T.-T. Tang, Y. Zhang, C.-H. Park, B. Geng, C. Girit, Z. Hao, M. C. Martin, A. Zettl, M. F. Crommie, S. G. Louie, Y. R. Shen, and F. Wang, A tunable phonon–exciton Fano system in bilayer graphene, *Nat. Nano.* **5**, 32 (2010).